SLAC – 289
UC-34D
(E)

A STUDY OF HADRONIZATION USING ENERGY FLOW FROM e^+e^- ANNIHILATION INTO QUARKS AND GLUONS AT $\sqrt{s}$ OF 29 GeV*

Leslie J Rosenberg

Stanford Linear Accelerator Center
Stanford University
Stanford, California 94305

November 1985

Prepared for the Department of Energy
under contract number DE-AC03-76SF00515

Printed in the United States of America. Available from the National Technical Information Service, U.S. Department of Commerce, 5285 Port Royal Road, Springfield, Virginia 22161. Price: Printed Copy A08, Microfiche A01.

* Ph.D. Dissertation.

Abstract

We have made a high statistics study of QCD jets produced in e^+e^- annihilations at $\sqrt{s}$ of 29 GeV and observed in the MAC detector located at the PEP storage ring at SLAC. The MAC detector uses calorimetry and provides a homogeneous response over much of its $98\% \cdot 4\pi$ sr instrumented solid angle. A data sample of well reconstructed hadronic events was selected by requiring that E_{vis} in the calorimeters be near $\sqrt{s}$, and almost all the energy be deposited in the central calorimeters. Fits of the jet transverse energy flow are made to the data using String (STR) model and several types of Independent Jet (IJM) model hypotheses, where α_s, the strong coupling constant, and σ_q, the width of the secondary quark $P_\perp$ distribution, are free parameters. The fits to $O(\alpha_s^2)$ using $\overline{MS}$ renormalization yield $\alpha_s \sim 0.17$ with the STR hypothesis, and $\alpha_s \sim 0.12$ with the various IJM hypotheses. The correlations between α_s and σ_q are examined. Detailed comparisons were made with other experimental results. The energy flow projected onto the event plane of *3-jet* events selected from the above data sample was studied. The data shows an asymmetric energy flow around the thin jet. Such an asymmetry was predicted by the STR model, and a cluster model (Webber) incorporating soft gluon interference. The various IJM models show no such asymmetry. We associate this asymmetry with coherence effects during hadronization.

Acknowledgements

I thank Professor David Ritson, my thesis advisor, for guidance and support during my graduate studies at Stanford. He is a gentle soul and a skilled physicist; I have gained much from our association.

I also thank my mother and father. My work was made much easier knowing I have parents who are very proud of me.

My wife Cecilia deserves special thanks. Her constant support and love made this thesis possible.

I thank Joseph Ballam, Martin Perl and Michael Peskin for helpful suggestions, and for not working me over at my thesis defense. Harvey Lynch and Thomas Gottschalk provided helpful discussions over the course of my research. My thanks to Henry Band, Robert Messner and Patricia Rankin for editing this manuscript, and to Art Ogawa for computer typesetting software. I thank the SLAC library for cheerful, prompt and accurate assistance. I thank the MAC Collaboration for having designed and built the software and hardware for our elegant detector.

My thanks to Drew Baden, Halsie Reno and Harry Nelson for helpful discussions, friendship and understanding.

Table of Contents

List of Tables

List of Figures

1. Introduction

The currently accepted view holds that the strong interactions are described by Quantum Chromodynamics (QCD), a gauge theory of quarks interacting through gluons. Perturbative QCD is predictive for large Q^2 processes. However, the fragmentation of quarks and gluons into hadrons is a low Q^2 phenomenon not yet amenable to QCD calculations. At low Q^2, in place of a predictive theory, we rely on phenomenological models describing fragmentation. The purpose of this study is to measure α_s, the coupling constant of large Q^2 QCD, and to determine which of the phenomenological models best describe low Q^2 fragmentation.

1.1 Developments Leading to QCD

Quarks were the name given in the early 1960's to the hypothesized constituents of hadrons.[1] It was proposed that the observed hadron spin was a result of coupling the constituent quark spins, and that the additive hadron quantum numbers of charge, flavor and baryon number reflected those of the quark constituents.

By the mid 1960's, indirect evidence for an underlying quark structure of nucleons surfaced through studies of hadron classification, static moments, decays and collisions.[2] In the 1968 Vienna conference, W.K.H. Panofsky presented evidence in a rapporteur talk that "... these data might give evidence on the behavior of point-like, charged structures within the nucleon."[3] He was referring to results from the SLAC deep-inelastic scattering experiments. It appeared that nucleons contained physical quarks, and that these quarks were asymptotically free (that is, they appeared non-interacting to large Q^2 photon probes). There were mysteries remaining after the Vienna conference; hadrons did not appear to exist containing more than three quarks; free quarks were not observed; and asymptotic freedom. A model with non-interacting quarks was too simplistic.

The success of QED in describing electrodynamics encouraged theorists to develop analogous gauge theories describing quark dynamics. It was noted that $SU(3)$ triplet quarks interacting with $SU(3)$ octet gauge bosons, together with

the hypothesis that hadrons are $SU(3)$ singlets, explained much of the hadron classification problem.[4,5]The discovery of ψ resonances in 1974 gave credence to the model of quarks as physical hadron constituents. By the mid-1970's, QCD, the gauge theory of quark interactions emerged. QCD features a new quantum number, color (C), quarks as $SU(3)_C$ triplets, gluons as $SU(3)_C$ octets, a coupling constant $\alpha_s(Q^2)$ that decreases with increasing Q^2, and the hypothesis of confinement where observed particles are color singlets.

1.2 The Process $e^+e^- \rightarrow hadrons$

The fact that R, the ratio of hadron production to muon pair production, is relatively constant[6] over a wide range of $\sqrt{s}$, the center of mass energy, in e^+e^- annihilation implies that the virtual photon γ^* has a point-like coupling to the final state hadrons.[7] This requirement is satisfied in a quark-parton model,[8] with $e^+e^- \rightarrow \gamma^* \rightarrow partons \rightarrow hadron\ jets$.

The partons produced in the hard production process $\gamma^* \rightarrow q\bar{q}$ are, in general, far off the mass shell, with $M_q \sim \sqrt{s}/2$. Subsequent fragmentation of the partons into hadrons results in jets of on shell final state particles, with characteristic masses of $O(1\,\mathrm{GeV})$.

These rather different energy scales for parton production and fragmentation imply that the hard perturbative process $e^+e^- \rightarrow partons$, and the soft fragmentation process $partons \rightarrow hadrons$, occur over quite different times in the event evolution. Consider the uncertainty relation $\Delta E \Delta t \sim 1$ with ΔE the difference between the on and off shell masses. For $\sqrt{s}$ of 30 GeV, the hard parton production time Δt_p is related to the soft parton fragmentation time Δt_f by

$$\Delta t_f / \Delta t_p \sim \sqrt{s}/M_0 \sim 30\,\mathrm{GeV}/1\,\mathrm{GeV} \quad ,$$

where M_0 is the characteristic hadron mass. So, with the center of mass energy for this experiment, characteristic times of soft fragmentation are about 30 times longer than the time scale of the initial hard production. To a good approximation, the production of hard partons and their subsequent soft fragmentation can be treated as independent processes; the former followed by the latter, if we ignore soft fragmentation during the period of hard production. This justifies the two step procedure we will use in order to model hadronization; one Monte Carlo generates partons which are then input to another Monte Carlo that performs the fragmentation.

The rest of this section gives a short description of the role that coupling constants play in gauge theories, with particular emphasis on the role of α_s in the Standard model. It is interesting to measure α_s, not only because it is a fundamental parameter, but also because predictions for the physics occurring at very high energies are dependent on the weak scale value of α_s. An example of the influence of α_s on predictions of the proton lifetime in a simple model will be given later.

1.2.1 The Standard Model of Electro-Weak Interactions

The interactions among fermions are described by gauge theories where the Lagrangian is invariant under a gauge group rotation at each point in space-time. This requirement of local gauge invariance requires the existence of bosons that mediate fermion interactions. The same requirement of local gauge invariance also prohibits the initial fermions and the intermediate bosons from having corresponding mass terms in the Lagrangian. The process of spontaneous symmetry breaking with the Higgs mechanism generates mass for the weak vector bosons by introducing an additional scalar Higgs field into the theory. The resulting minimal theory that accounts for observed phenomena couples local gauge invariance with the Higgs scheme of spontaneous symmetry breaking. The model for the electromagnetic and weak sector is called the Glashow-Weinberg-Salam Model (GSW) in honor of its proponents. The model describing strong interactions is called Quantum Chromodynamics (QCD). The combination of GSW and QCD is called the standard model. The standard model incorporates all the known particles and interactions, excepting gravity.

1.2.1.1 The Fundamental Fermions

The fundamental fermions may be divided into three families of increasing mass. The observation of maximal parity violation of charged weak decays into left-handed neutrinos requires that the right-handed fermions be weak isosinglets, and that the left-handed fermions form weak isodoublets. Before local gauge invariance is invoked, there exist the massless fermions depicted in Table 1.1, grouped into weak eigenstates. The first family, containing the electron, electron neutrino and the u and d quark combined, makes up the bulk of the matter in the universe.

1.2.1.2 Local Gauge Invariance

We start with a Lagrangian that contains only fermion kinetic energy terms

Table 1.1. The fundamental fermions.

first family	second family	third family	
$\begin{pmatrix}\nu_e \\ e^-\end{pmatrix}_L$	$\begin{pmatrix}\nu_\mu \\ \mu^-\end{pmatrix}_L$	$\begin{pmatrix}\nu_\tau \\ \tau^-\end{pmatrix}_L$	Leptons
$(e^-)_R$	$(\mu^-)_R$	$(\tau^-)_R$	
$\begin{pmatrix}u \\ d\end{pmatrix}_L$	$\begin{pmatrix}c \\ s\end{pmatrix}_L$	$\begin{pmatrix}t \\ b\end{pmatrix}_L$	
$(u)_R$ $(d)_R$	$(c)_R$ $(s)_R$	$(t)_R$ $(b)_R$	Quarks

given by

$$\mathcal{L}_f = \overline{L}\gamma^\mu \partial_\mu L + \overline{R}\gamma^\mu \partial_\mu R \quad ,$$

where the right (R) and left (L) fermion wave functions are represented by

$$\overline{L} = \left(\bar{e}_L, \bar{\mu}_L, \bar{\tau}_L, \bar{\nu}_{eL}, \cdots, \bar{t}_L, \bar{b}_L\right) \quad ,$$
$$\overline{R} = \left(\bar{e}_R, \bar{\mu}_R, \bar{\tau}_R, \cdots, \bar{t}_R, \bar{b}_R\right) \quad .$$

By demanding that the Lagrangian be locally gauge invariant, interactions between the fermions are generated in a natural way. The fermionic fields are presumed to exhibit local gauge invariance under $U(1)_Y$, $SU(2)_L$ and $SU(3)_C$ transformations. The label Y denotes hypercharge, related to the electromagnetic charge and the weak isospin through the relation

$$Q = I_3 + \tfrac{1}{2}Y \quad .$$

The label L indicates that only left-handed currents couple in the weak interactions. The label C denotes color, the name for SU(3) charge. This is the minimal group

structure consistent with the observed character of the particle interactions. The invariance under $U(1)_Y$ generates a neutral vector boson denoted C^0. Invariance under $SU(2)_L$ results in 3 vector bosons: a neutral boson B^0, and two charged bosons B^- and B^+. The invariance of the Lagrangian under $SU(3)_C$ rotations results in eight vector bosons G^a, $a = 1$ to 8, called gluons. Colored objects have yet to be observed in a free state. This observation is accommodated by the hypothesis that the only allowed unbound objects must be color singlets. Therefore, quarks and gluons are presumed to always fragment into colorless hadrons. Mass terms in the Lagrangian for these additional bosons must also be absent in order to satisfy the demands of local gauge invariance. Invoking local gauge invariance adds the boson interaction and kinetic energy terms to the Lagrangian. The interactions are generated by replacing the derivative with the covariant derivative, so the term coupling the bosons to the fermions reads:

$$\begin{aligned}\mathcal{L}_f =& \overline{L}\gamma^\mu \left(\partial_\mu - i\frac{g'}{2}B_\mu Y - i\frac{g}{2}\hat{\tau}\cdot\vec{C}_\mu - i\frac{g_s}{2}\lambda^a G^a_\mu\right) L \\ &+ \overline{R}\gamma^\mu \left(\partial_\mu - i\frac{g'}{2}B_\mu Y - i\frac{g_s}{2}\lambda^a G^a_\mu\right) R\end{aligned}$$

where λ^a, $a = 1,8$ are the eight independent traceless matrices in a 3×3 representation of $SU(3)_C$, and g', g and g_s are the coupling strengths for the $U(1)_Y$, $SU(2)_L$ and $SU(3)_C$ gauge bosons.

1.2.1.3 Spontaneous Symmetry Breaking and the Higgs Mechanism

So far, gauge invariance forbids quadratic mass terms to appear. However, the observation that the weak interactions are short range call for massive bosons. The electromagnetic interaction is long range and is mediated by a massless photon. Since the gluons are never observed as free particles, the masses of the gluons are somewhat ill-defined. The effects of a gluon mass of less than of $O(1\,\text{GeV})$ would be masked by its fragmentation, and a hypothesis of zero mass for the gluons seems consistent with observation.

As a result of requiring local gauge invariance, there appear the massless vector fields C^0, B^0, B^+, B^- and G^a in the covariant derivative. After spontaneous symmetry breaking the weak bosons Z^0, W^- and W^+ acquire mass, while the remaining bosons must remain massless. One way to do this is to introduce a complex $SU(2)_L$ isospin doublet, ϕ, called the Higgs field, into the Lagrangian,

incorporating the gauge fields in the usual way to insure $SU(2)_L \times U(1)_Y$ local gauge invariance. The extra Higgs terms in the Lagrangian includes a gauge invariant kinetic energy, the most general potential consistent with renormalizability, and a Yukawa term coupling the Higgs to the fermions:[9]

$$\mathcal{L}_{Higgs} = (D^\mu \phi)^\dagger (D_\mu \phi) - V(\phi^\dagger \phi) + \mathcal{L}_{interaction} \quad ,$$

where

$$D^\mu = \partial^\mu + \frac{ig}{2}\vec{\tau}\cdot\vec{C}^\mu + \frac{ig'}{2}YB^\mu \quad ,$$

$$V(\phi^\dagger\phi) = \frac{\mu^2}{2}\phi^\dagger\phi + \frac{|\lambda|}{4}(\phi^\dagger\phi)^2 \quad ,$$

and

$$\mathcal{L}_{interaction} = -G_e[\bar{e}_R\phi^\dagger e_L + \bar{e}_L\phi e_R] - G_\mu[\bar{\mu}_R\phi^\dagger\mu_L + \bar{\mu}_L\phi\mu_R] - \ldots - G_b[\bar{b}_R\phi^\dagger b_L + \bar{b}_L\phi b_R] \quad .$$

The Higgs field is assumed to have a non-zero real vacuum expectation value for the neutral component:

$$\langle\phi\rangle = \begin{pmatrix} 0 \\ v \end{pmatrix} \quad .$$

When the Lagrangian is expanded around the vacuum expectation value of the Higgs field, some of the degrees of freedom in the Higgs field appear in the vector bosons. In particular, the fields C^0 and B^0 combine into a massive field Z^0, and a massless field A^0 according to:

$$Z^0 = \left(g'B^0 - gC^0\right)/\sqrt{g^2+g'^2} \qquad \text{and} \qquad A^0_\mu = \left(g'B^0 + gC^0\right)/\sqrt{g^2+g'^2} \quad .$$

The fields B^+ and B^- combine into the massive fields W^+ and W^- according to:

$$W^+ = \left(C^+ - iC^-\right)/\sqrt{2} \qquad \text{and} \qquad W^- = \left(C^+ + iC^-\right)/\sqrt{2} \quad .$$

The electric charge is related to the $U(1)_Y$ and $SU(2)_L$ coupling strengths by:

$$e = gg'/\sqrt{g^2+g'^2} = g\sin\theta_W = g'\cos\theta_W \quad ,$$

where the Weinberg angle θ_W parameterizes the mixing. The connection between low energy weak phenomenology and the Higgs mechanism is through the relation of the Fermi constant to the vacuum expectation value of the Higgs field, given by

$$G_F/\sqrt{2} = \frac{1}{4}v^2 \quad .$$

The mass of W^+ and W^- are read off the quadratic terms in the Lagrangian as

$$M_W^2 = e^2/\left(4\sqrt{2}G_F \sin^2\theta_W\right) \approx (78\,\mathrm{GeV})^2 \quad ,$$

while the mass of the Z^0 is read off similarly as

$$M_Z^2 = M_W^2/\cos^2\theta_W \approx (90\,\mathrm{GeV})^2 \quad .$$

In all, by giving mass to Z^0, W^- and W^+, three degrees of freedom were taken from the complex doublet Higgs field. A vestige of the original Higgs field remains as a neutral real scalar, h. The mass of the Higgs scalar h remains unpredicted by the GWS theory.

The masses for the fermions are generated in a similar manner. The neutral Higgs retains couplings to, say, right and left-handed electrons via terms of the form:

$$\mathcal{L} = \frac{-G_e}{\sqrt{2}}v\,(e_L e_R + e_R e_L) + \frac{-G_e}{\sqrt{2}}\,(e_L e_R + e_R e_L)\,h \quad ,$$

with G_e arbitrary. If G_e is chosen so that $G_e = \sqrt{2}M_e/v$, then the observed electron mass results from the first term. The masses of the other leptons and quarks result from similar couplings. Since G_e (and $G_\mu, \cdots, G_b$) is arbitrary, fermion masses are not predicted, but are simply allowed by the model. The gluons don't acquire mass since the Higgs field was presumed to leave $SU(3)_C$ unbroken.

The properties of the fundamental quanta are given in Table 1.2. Of these quanta, only the Higgs scalar remains unobserved.

1.2.1.4 The GIM Mechanism

The mass eigenstates of the quarks are not the same as the weak eigenstates. This is the Glashow, Iliopoulos and Maiani (GIM) generalization of the Cabbibo

Table 1.2. Properties of the fundamental quanta.

	mass GeV		mass GeV		mass GeV	Q ($\|e\|$)	T	T_3	Y	S
$\binom{\nu_e}{e^-}_L$	~ 0 5×10^{-4}	$\binom{\nu_\mu}{\mu^-}_L$	~ 0 1×10^{-1}	$\binom{\nu_\tau}{\tau^-}_L$	~ 0 1.78	0 -1	$\frac{1}{2}$ $\frac{1}{2}$	$\frac{1}{2}$ $-\frac{1}{2}$	-1 -1	$\frac{1}{2}$ $\frac{1}{2}$
$(e^-)_R$	5×10^{-4}	$(\mu^-)_R$	1×10^{-1}	$(\tau^-)_R$	1.78	-1	0	0	-2	$\frac{1}{2}$
$\binom{u}{d}_L$	3×10^{-1} 3×10^{-1}	$\binom{c}{s}_L$	1.5 0.5	$\binom{t}{b}_L$	~ 45 5	$\frac{2}{3}$ $-\frac{1}{3}$	$\frac{1}{2}$ $\frac{1}{2}$	$\frac{1}{2}$ $-\frac{1}{2}$	$\frac{1}{3}$ $\frac{1}{3}$	$\frac{1}{2}$ $\frac{1}{2}$
$(u)_R$	3×10^{-1}	$(c)_R$	1.5	$(t)_R$	45	$\frac{2}{3}$	0	0	$\frac{4}{3}$	$\frac{1}{2}$
$(d)_R$	3×10^{-1}	$(s)_R$	0.5	$(b)_R$	5	$-\frac{1}{3}$	0	0	$-\frac{2}{3}$	$\frac{1}{2}$
γ					0	0	0	0	0	1
Z^0					93	0	1	0	0	1
W^+					81	1	1	1	0	1
h					?	0	$\frac{1}{2}$	$-\frac{1}{2}$	1	0
G^a					~ 0	0	0	0	0	1

theory of quark mixing. The charged current decays of the quarks are given by:

$$J^\mu = (\bar{u} \quad \bar{c} \quad \bar{t}) \frac{\gamma^\mu(1-\gamma^5)}{2} U \begin{pmatrix} d \\ s \\ b \end{pmatrix}$$

where U is the quark mixing matrix. The diagonal terms in U are very near 1. The off-diagonal terms are small, with the exception of the matrix element corresponding to a current of $s \rightarrow u$, with $|U_{su}| \approx 0.23$. In the Standard model, the GIM mixing doesn't extend to the lepton doublets. Since the neutrinos are massless, any rotation among the neutrinos still leaves them in a mass eigenstate. This rotated neutrino state is then defined to be the partner of the associated charged lepton.

The grouping of quarks and leptons into weak doublets results in conserved family quantum numbers in weak decays. The unmixed lepton doublets have

absolutely conserved quantum numbers. The quark doublets have a small component of family non-conservation through quark mixing.

1.2.2 Coupling Constants

The process where fermions exchange a gauge boson may be used to define the strength of the electromagnetic, weak and strong interactions. The vertex factors are given in Fig. 1.1. These amplitudes for the exchange may be written in the form of a factor, times a function of the fermion quantum numbers

$$A = \alpha \times f \begin{pmatrix} \text{fermion} \\ \text{quantum} \\ \text{numbers} \end{pmatrix} \quad .$$

The factor α is called a coupling constant, and is related to the probability for a fermion to emit a gauge boson.

1.2.2.1 Q^2 Dependence of the Coupling Constants

Higher order loops make the exchanged boson a very complicated object. Recall in QED that the complete photon propagator may be represented as a sum of diagrams with increasing complexity of internal loops, as shown in Fig. 1.2. The diagrams in the second row involve an integration of only one momenta loop. All these one-loop diagrams may be summed explicitly to yield an effective propagator at the "one loop" level. The loop integrals diverge, but the resulting divergences may be absorbed into a redefinition of the coupling constants at the vertex. The process of absorbing loop divergences into a redefined, finite coupling, is called renormalization. A similar procedure that also includes vertex and self energy contributions results in a renormalized QCD coupling constant. The value of the renormalized coupling constant depends on the square of the four-momentum (Q^2) entering the loop. The change in the coupling constant with Q^2 is termed its running behavior.

The observed coupling constants for the electromagnetic, strong, and charged and neutral current weak interactions are denoted α_{em}, α_s, α_W, α_Z. These observed coupling constants may be written in terms of the coupling constants of the $SU(3)_C \times SU(2)_L \times U(1)_Y$ gauge group. Recall that the gauge coupling strengths are g' for $U(1)_Y$, g for $SU(2)_L$, and g_s for $SU(3)_C$. The gauge coupling constants are defined by the relations:

$$\alpha_{g'} = g'^2/4\pi \qquad \alpha_g = g^2/4\pi \qquad \alpha_s = g_s^2/4\pi \quad .$$

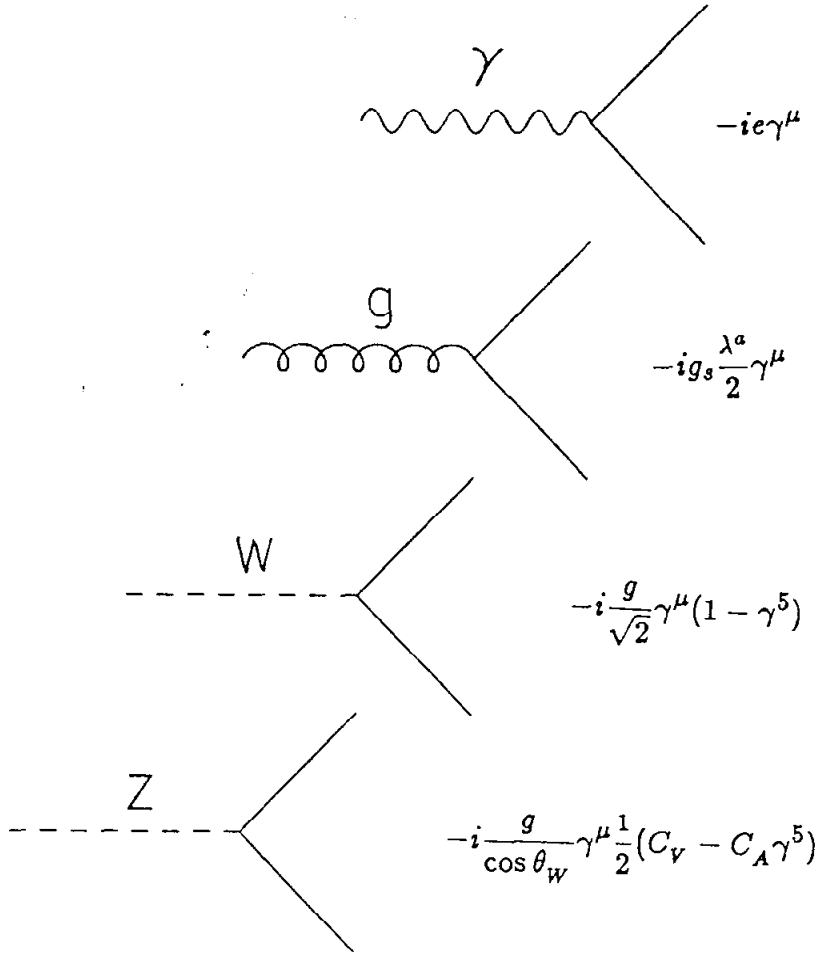

Figure 1.1. Vertex factors for the electromagnetic, strong, and charged and neutral current interactions.

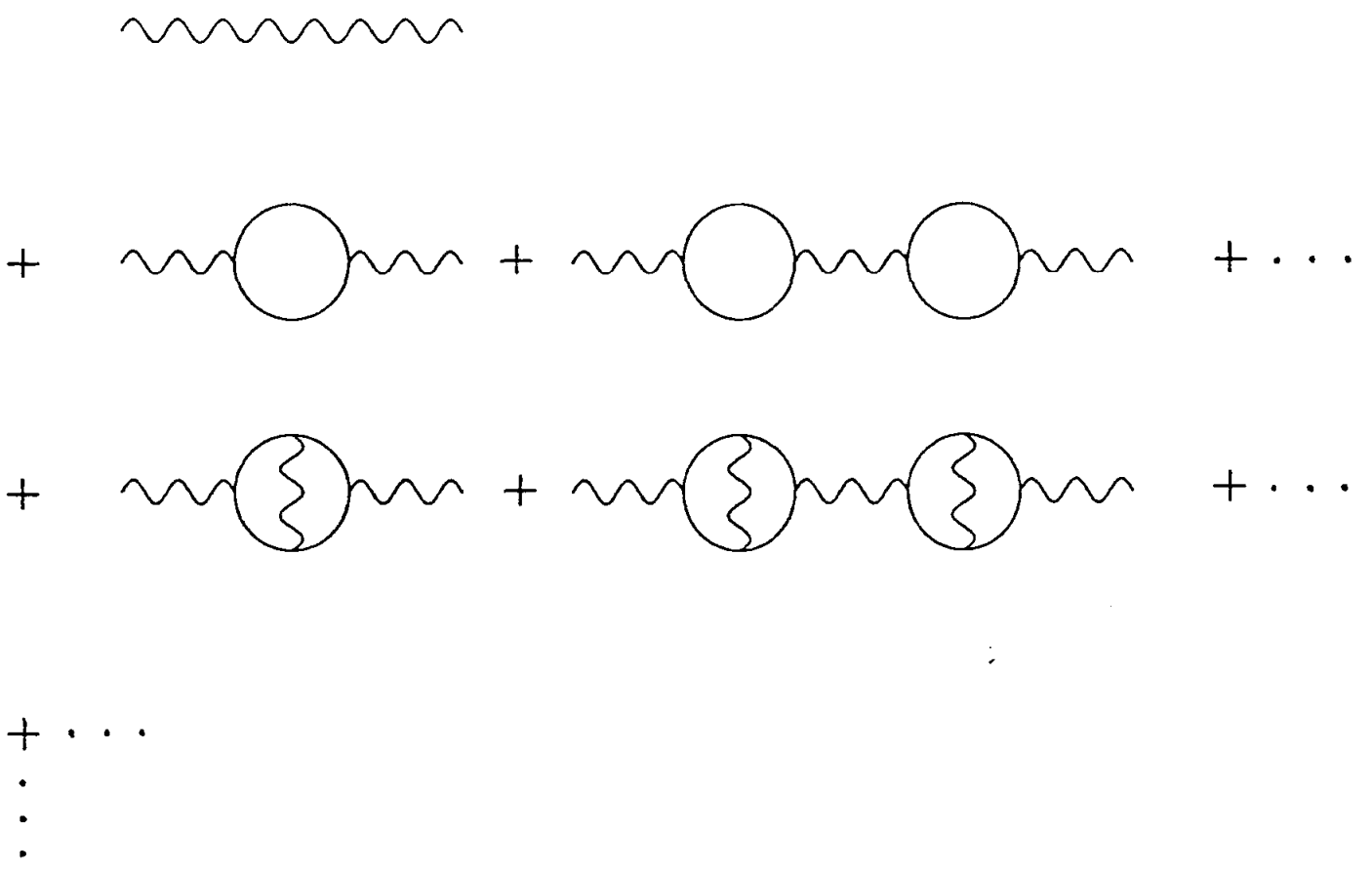

Figure 1.2. The expansion of the photon propagator into diagrams involving internal loops. These diagrams result in a coupling constant whose magnitude depends on the Q^2 entering the loops.

When all the loop corrections are included in the propagator, and the masses of particles participating in the loops are ignored, the running behavior of any coupling constant for the gauge group G may be expressed as[10,11]

$$\frac{d\alpha_G}{d\ln Q^2} = \frac{b_G}{4\pi} g_G^4 + O(g_G^6) \quad ,$$

with

$$b_G = -\left[\frac{11}{3}C_2(G) - \frac{4}{3}T_f(G)\right]/(4\pi)^2 \quad .$$

When $b_G > 0$, then α_G grows with increasing Q^2. The constants C_2 and T_f depend on the particular gauge group G. For $SU(3)_C \times SU(2)L \times U(1)_Y$, we have

$$C_2\left[SU(n)\right] = n \qquad C_2\left[U(1)\right] = 0$$
$$T_f\left[SU(3)\right] = n_q/2 \qquad T_f\left[SU(2)\right] = n/4 \qquad T_f\left[U(1)\right] = 5F/3 \quad ,$$

with n_q the number of quark flavors, n the number of left handed doublets (each quark doublet counts three times due to color), and F the number of families. The standard model assumes $n_q = 6$, $n = 12$, and $F = 3$. When $b_G < 0$, then α_G becomes smaller as Q^2 increases, and we say that the coupling becomes asymptotically free. The solutions to order one loop, well above the masses of any particles participating in the loops, and ignoring the Higgs scalar are given by

$$\alpha_G(Q^2) = \frac{\alpha_G(\mu^2)}{1 - \alpha_G(\mu^2) 4\pi b_G \ln\frac{Q^2}{\mu^2}} \quad ,$$

where $\alpha_G(\mu^2)$ is the value of α_G at some scale μ^2.

The physical coupling constants are, in general, mixtures of the gauge coupling constants. Examination of the vertex factors of Fig. 1.1 reveals that the charged weak coupling constant, unmixed with the $U(1)_Y$ coupling, is given by:

$$\alpha_W(Q^2) = \alpha_g \quad .$$

The observed neutral weak coupling is complicated by the running of $\sin^2\theta_W$, through the running of α_g and $\alpha_{g'}$. However, for the simplified coupling to neutrinos,

we have:

$$\alpha_Z(Q^2) = \left(\frac{g}{\cos\theta_W}\right)^2/4\pi$$
$$= \alpha_g + \alpha_{g'} \quad .$$

The electromagnetic coupling constant is given by:

$$\frac{1}{\alpha_{em}} = \frac{1}{\alpha_{g'}} + \frac{1}{\alpha_g}$$

or

$$\alpha_{em} = \frac{\alpha_{em}(\mu^2)}{1 - \alpha_{em}(\mu^2)\frac{1}{4\pi}\left[\frac{n}{3} + \frac{20}{9}F - \frac{22}{3}\right]\ln\frac{Q^2}{\mu^2}} \quad .$$

The strong coupling is given by:

$$\alpha_s(Q^2) = \alpha_{g_s} = \frac{\alpha_s(\mu^2)}{1 - \alpha_s(\mu^2)\frac{1}{4\pi}\left[\frac{2n_q}{3} - 11\right]\ln\frac{Q^2}{\mu^2}} \quad .$$

Here, the one-loop running behavior of α_s becomes singular when the denominator vanishes, and defines a scale where the QCD coupling becomes large. The value of Q^2 where this occurs is termed Λ^2 and is given by

$$\Lambda^2 = \mu^2 \exp\left(\frac{4\pi}{\alpha_s(\mu^2)}\ \frac{1}{\frac{2}{3}n_q - 11}\right) \quad .$$

In terms of this QCD scale Λ^2, the one-loop running behavior of α_s is given by[a]

$$\alpha_s(Q^2) = \frac{4\pi}{(11 - 2n_q/3)\ln(\frac{Q^2}{\Lambda^2})} \quad .$$

In the Standard model with $n_q = 6$, QCD is asymptotically free. Also note α_{em} can increase or decrease with increasing Q^2, depending on the number of families, the crossover occurring at $F \approx 2$. This somewhat surprising result arises from weak loops in the photon propagator. The coupling constant attached to the $U(1)_Y$ group does, however, run in the expected way for a pure $U(1)$ symmetry. The one loop

---

[a] The one-loop expression for α_s is independent of the regularization scheme.[12]

Q^2 evolution of $\alpha_{g'}$, α_g and α_s is shown in Fig. 1.3, where the effects of any scalars have been ignored, along with the masses of the particles participating in the loops. Note how rapidly α_s runs with Q^2, relative to α_g and $\alpha_{g'}$.

The value of α_s at PEP energies has a large effect on very high energy phenomenology. As an example, a minimal Grand Unified Theory (GUT) predicts that at energies below some unification scale M_x, $SU(5)$ is broken into $SU(3)_C \times SU(2)_L \times U(1)_Y$. Above M_x, there is an unbroken $SU(5)$ symmetry with a single coupling constant α_G.[13] The factor of 5/3 seen in Fig. 1.3 multiplying $\alpha_{g'}$ is a normalization imposed by the $SU(5)$ group structure. The unification scale M_x depends on α_s. The one loop dependence of M_x on α_s in this minimal model is shown in Table 1.3 for a reasonable range of α_s. Also shown in Table 1.3 is the α_s dependence of the proton lifetime, given by the relation[14]

$$\tau_p \sim \frac{1}{\alpha_G^2} \frac{M_x^4}{m_p^5} \quad .$$

Note the strong effect the value of α_s has on the predicted proton lifetime. Though null results from the current generation of proton decay experiments have placed minimal this $SU(5)$ GUT in disfavor, this exercise illustrates the importance of α_s measurements at PEP energies in order to extrapolate beyond a possible desert of continuum physics expected to lie above the weak scale.

1.2.3 Perturbative QCD

The early time evolution of $e^+e^- \rightarrow$ *hadrons* can be understood in terms of perturbative QCD. The cross section for the process $e^+e^- \rightarrow$ *quarks* + *gluons*, may be calculated either exactly to some finite order in α_s, or approximately by summing the leading logarithms explicitly to all orders.

At this point the model already has some predictive power. Perturbative QCD predicts, in agreement with observation,[17] that with increasing $\sqrt{s}$, the hadrons will form back-to-back jets, whereas simple phase space models predict increasingly isotropic event shapes. Jets are a phenomenon where hadrons are emitted with limited $P_\perp$ relative to some particular axis in the event. With large enough center of mass energy, hadronic events tend to take on a planar configuration.[18] Figure 1.4a displays the distribution of $\langle P_\perp^{IN^2} \rangle$, the per-event average square of the event momentum in the event plane, for MAC data at $\sqrt{s}$ of 29 GeV. Also shown in Fig. 1.4b and Fig. 1.4c are Monte Carlo predictions for $\sqrt{s}$ of 29 GeV, including

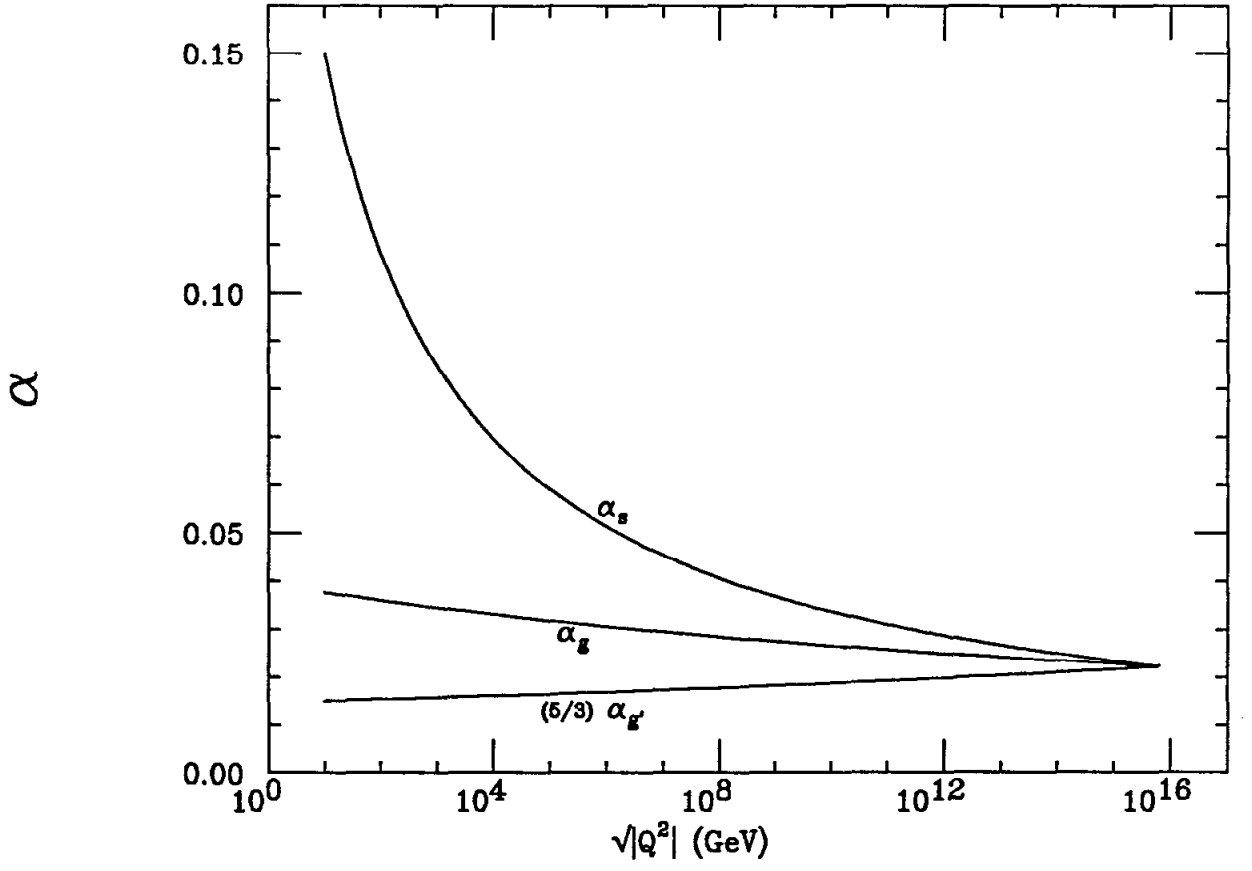

Figure 1.3. The one loop Q^2 evolution of $\frac{5}{3}\alpha_{g'}$, α_g and α_s. The curves were generated assuming α_s of .15 at Q^2 of $(10\,\mathrm{GeV})^2$. The effects of any scalars along with the masses of particles participating in the loops have been ignored. The unification point is highly dependent on α_s at the weak scale. The factor of 5/3 on the $U(1)_Y$ coupling constant is a normalization imposed by the specific model discussed in the text.

Table 1.3. The unification scale and proton lifetime as a function of α_s (at a Q^2 of 30^2 GeV^2) for the minimal Georgi and Glashow $SU(5)$ model. The unification scale M_x is given by $M_x \approx 1.3 \times 10^{-15} \Lambda_{\overline{MS}}$.[15] For the proton lifetime, the expression[16] $\tau_p \approx 2C \times 10^{-29} (M_x/\mathrm{GeV})^4$years is used. The factor of C accounts for theoretical uncertainty for in the proton decay matrix elements. Marciano gives C in the range 1-30. As a representative value, C is chosen to be 10 for the numbers shown in this table. We emphasize that this table represents not the definitive proton lifetime, but rather a reminder that small uncertainties in α_s at the weak scale are magnified enormously at the GUT scale.

α_s	$\Lambda_{\overline{MS}}$(MeV)	M_x(GeV)	τ_p(years)
.10	020	2.6×10^{14}	9.1×10^{25}
.15	270	3.5×10^{14}	3.0×10^{30}
.20	940	$12. \times 10^{14}$	4.4×10^{32}

detector simulation, for the full $O(\alpha_s^2)$ and the $O(\alpha_s^0)$ $e^+e^- \rightarrow quarks(+gluons)$ matrix elements. Note that the full $O(\alpha_s^2)$ Monte Carlo reproduces the $\langle P_\perp^{IN^2} \rangle$ distribution quite well. When hard perturbative bremsstrahlung is turned off, the population in the tail of the $\langle P_\perp^{IN^2} \rangle$ decreases considerably. Enhancements in the tail of $\langle P_\perp^{IN^2} \rangle$ and similar distributions provided some of the first signals for perturbative gluon emission.

Also shown as Fig. 1.4d is a result from TASSO[19] at $\sqrt{s}$ of 34 GeV. The $\langle P_\perp^{IN^2} \rangle$ distribution for the TASSO data is similar to the MAC distribution. However, direct comparison of the MAC and TASSO results is difficult; the center of mass energy for the TASSO data is 5 GeV higher than that for the MAC data; the MAC data used the thrust axis as the jet axis, while the TASSO data used sphericity; and the MAC thrust axis was computed from energy vectors, while the TASSO sphericity was computed from momentum vectors. Even without correcting for these differences, the MAC and TASSO results display similar behavior for the $\langle P_\perp^{IN^2} \rangle$ distribution.

The discovery of unambiguous *3-jet* topologies at PETRA[18] is further evidence for the existence of gluons, and firmly establishes QCD as the dominant theory of the strong interactions. Figure 1.5 shows a very *3-jet*-like event from the MAC hadronic data sample. The components of the MAC detector shown outlined in Fig. 1.5 are described in Chapter 2. This is an exceptional event. In fact, most hadronic events containing a hard radiative gluon are difficult to distinguish from

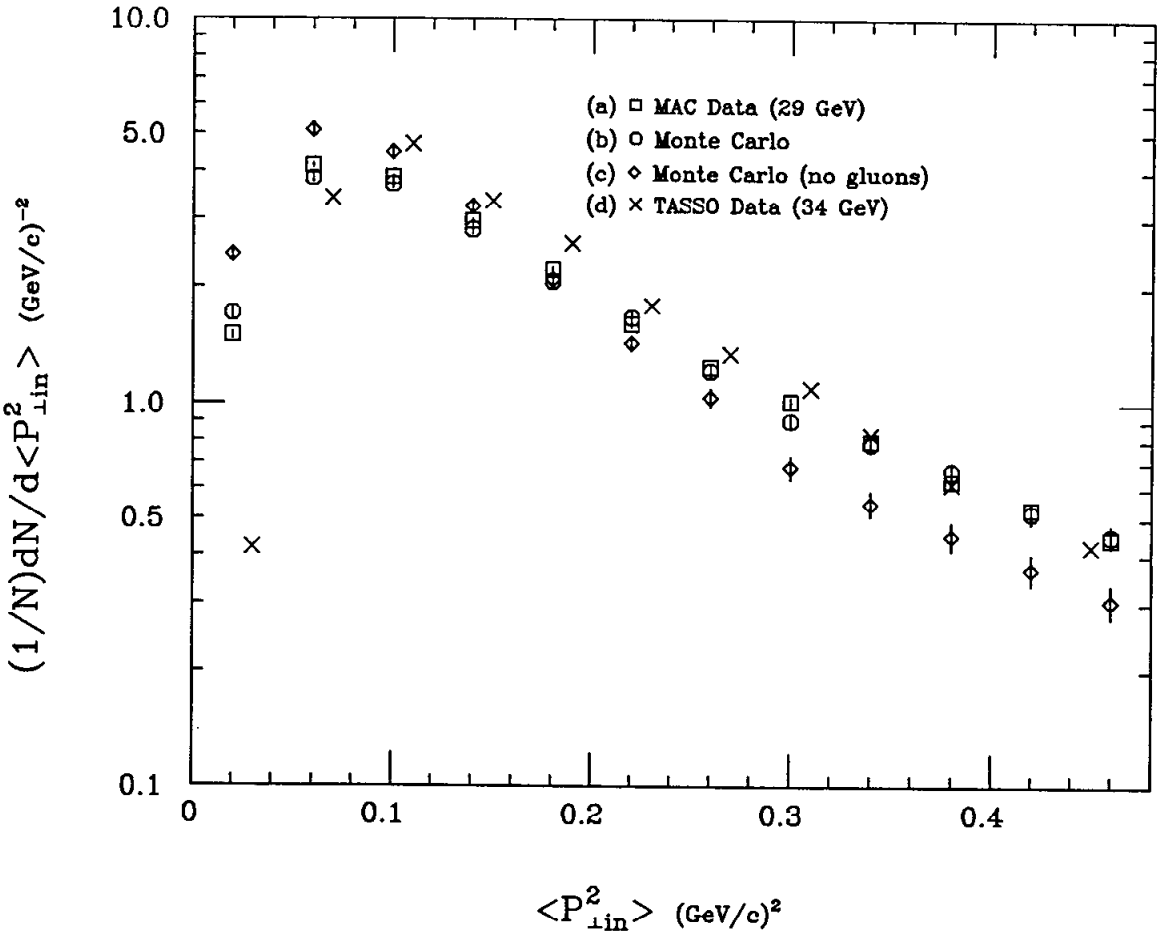

Figure 1.4. The distribution of $\langle P_{\perp}^{IN^2} \rangle$ for (a) MAC data at $\sqrt{s}$ of 29 GeV; (b) a Monte Carlo prediction incorporating the full $O(\alpha_s^2)$ $e^+e^- \rightarrow quarks + gluons$ matrix element for $\sqrt{s}$ of 29 GeV; (c) a Monte Carlo prediction incorporating the $O(\alpha_s^0)$ $e^+e^- \rightarrow quarks$ matrix element for $\sqrt{s}$ of 29 GeV; and (d) TASSO data from PETRA for $\sqrt{s}$ of 34 GeV. The enhancement of the population of this distribution at the high end of the distribution provided early evidence at PETRA for the gluon emission predicted by QCD.

2-jet events.

1.2.4 Non-Perturbative QCD Phenomenology

The observation of *3-jet* events is certainly a successful qualitative prediction of QCD. However, quantitative QCD measurements are difficult because the product of hard perturbative QCD production, the primary quarks and gluons, are not directly observable. They are presumed to fragment into hadrons through a non-perturbative (and so far uncalculable) mechanism. Hence, untangling the underlying parton dynamics from the hadronic final state requires introducing phenomenological models to account for the non-perturbative aspects of parton fragmentation. The required phenomenology is incorporated into Monte Carlo hadronization simulations that provide the necessary quantitative predictions. These simulations typically require many adjustable input parameters. The parameters are adjusted ("tuned") to give good agreement between data and the Monte Carlo predictions. Appendix A contains a more complete description of the methodology of generating predictions via Monte Carlo modeling.

There are two general types of analyses based on using these Monte Carlo simulations. One approach is to assume that the Monte Carlo provides an accurate description of hadron production. Then model parameters, such as α_s, may be fitted to agree with the data, albeit with an unavoidable model dependence of the result. Another approach is to compare the data and models with regard to the soft, non-perturbative aspects, and actually test the assumptions implicit in the Monte Carlos themselves. The motivation here is to establish whether the soft regime is described well by a particular phenomenological prescription. Then, perhaps, the phenomenology used in the surviving model provides clues to the nature of the physics in the soft fragmentation phase of hadronization.

The former approach yields quantitative results that have a strong dependence on the details of the modeling. The second approach is rather qualitative, yet results in conclusions about the predictive power of the hadronization models. Part of this analysis is in the style of the first approach and involves a Monte Carlo fitting of α_s to the data. The rest of the analysis takes the second approach and compares details of the energy flow in hadronic events with Monte Carlo predictions.

1.2.5 Techniques of Measuring α_s

α_s measurements have been performed at almost every high-energy accelerator

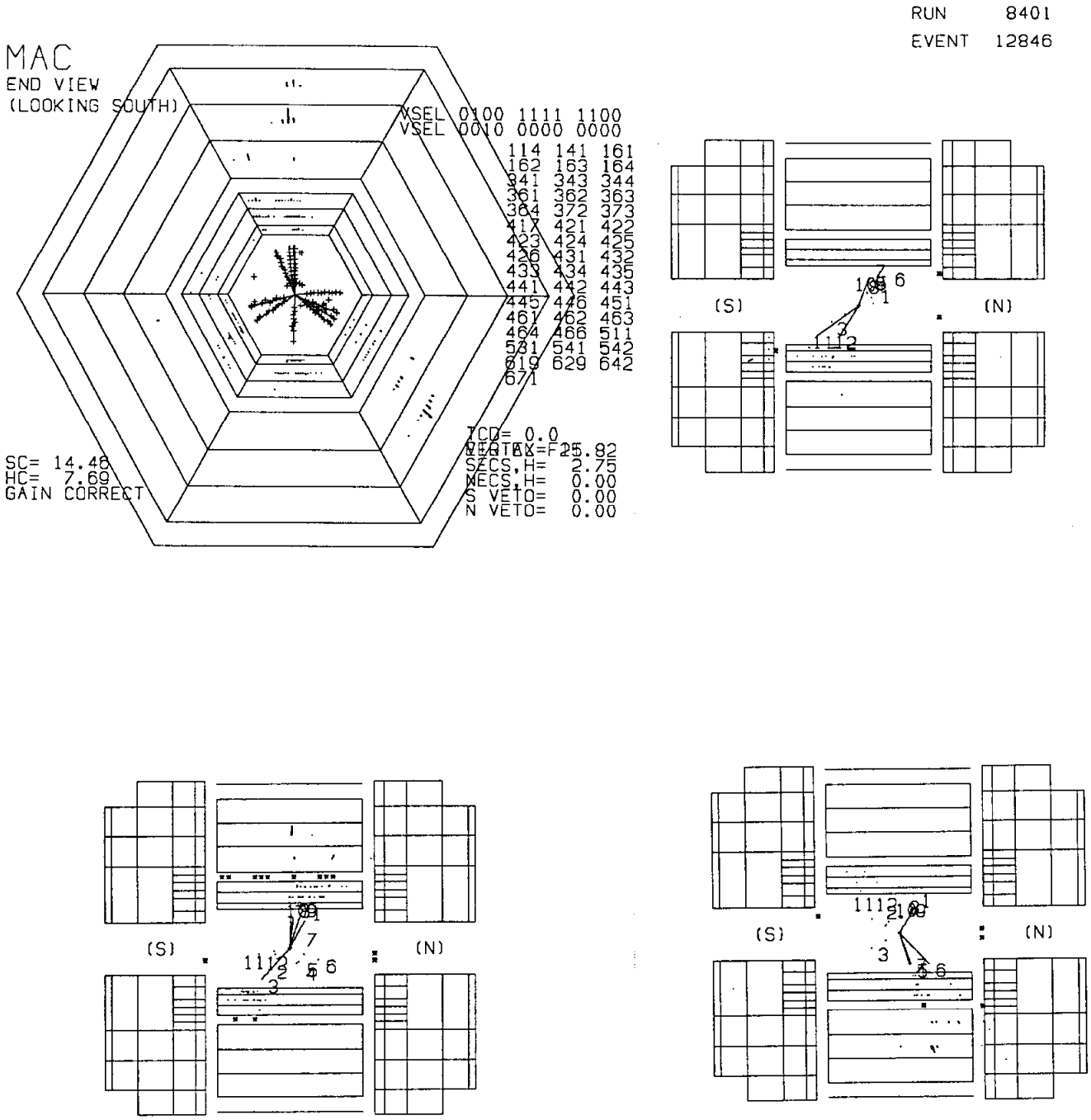

Figure 1.5. A very *3-jet*-like event from the MAC data sample. There are few such unambiguous *3-jet* events in the data sample.

around the world. In Fig. 1.6 are shown the various techniques for measuring α_s. Proceeding roughly from low to high energy, α_s can be measured:

- With onia resonances, usually the $\Upsilon(1S)$, by measuring the ratio of the hadron to μ pair production;
- With the shape of the photon structure function F_2^γ in 2γ interactions;
- With gluon bremsstrahlung corrections to $e^+e^- \rightarrow hadrons$;
- With scaling violations in deep-inelastic scattering;
- And recently, by the *3-jet/2-jet* ratio measured at the $SP\overline{P}S$.

These methods are given more detailed consideration in chapter 4. The PEP and PETRA α_s measurements essentially look for gluon radiative corrections in the process $e^+e^- \rightarrow hadrons$. The methods employed have been to: (1) Measure R, the ratio of hadron production to $\mu^+\mu^-$ production. (2) Count the number of *3-jet* events in the data sample; a cluster analysis. (3) Study hadronic event shapes. (4) Investigate energy-energy correlations in hadronic events.

This analysis uses an energy flow shape analysis to measure α_s, and further to examine subtle differences in energy flow predicted by fragmentation models.

1.3 Energy Flow as an Observable

From a theoretical perspective, energy flow was chosen as the observable in order to satisfy two requirements. The first requirement is that an observable should be immune to the $z \rightarrow 1$ and $t \rightarrow 0$ divergences of QCD (these variables are described in Appendix A); the cross sections for emitting arbitrarily soft gluons and for collinear bremsstrahlung of gluons are infinite.[20] The constraint imposed by the former divergence is satisfied by employing energy weighting in the observables. The constraint of the later divergence is satisfied by requiring that the weighting be first order in energy. Energy flow as the observable satisfies both constraints.

The second requirement of an observable is that it be relatively insensitive to "fine tuning" of the hadronization Monte Carlos. Observables containing dependence on particle type or absolute number density are suspect; these may vary greatly when the Monte Carlo parameters are adjusted. For example, one parameter common in hadronization Monte Carlos is the ratio of diquark to quark production. The baryon fraction in jets is strongly dependent on the value of this parameter. Its clear that an observable based on the absolute baryon production rate is very sensitive to this particular parameter, and not to the structure of the model. Energy flow as the observable, on the other hand, is rather insensitive as to

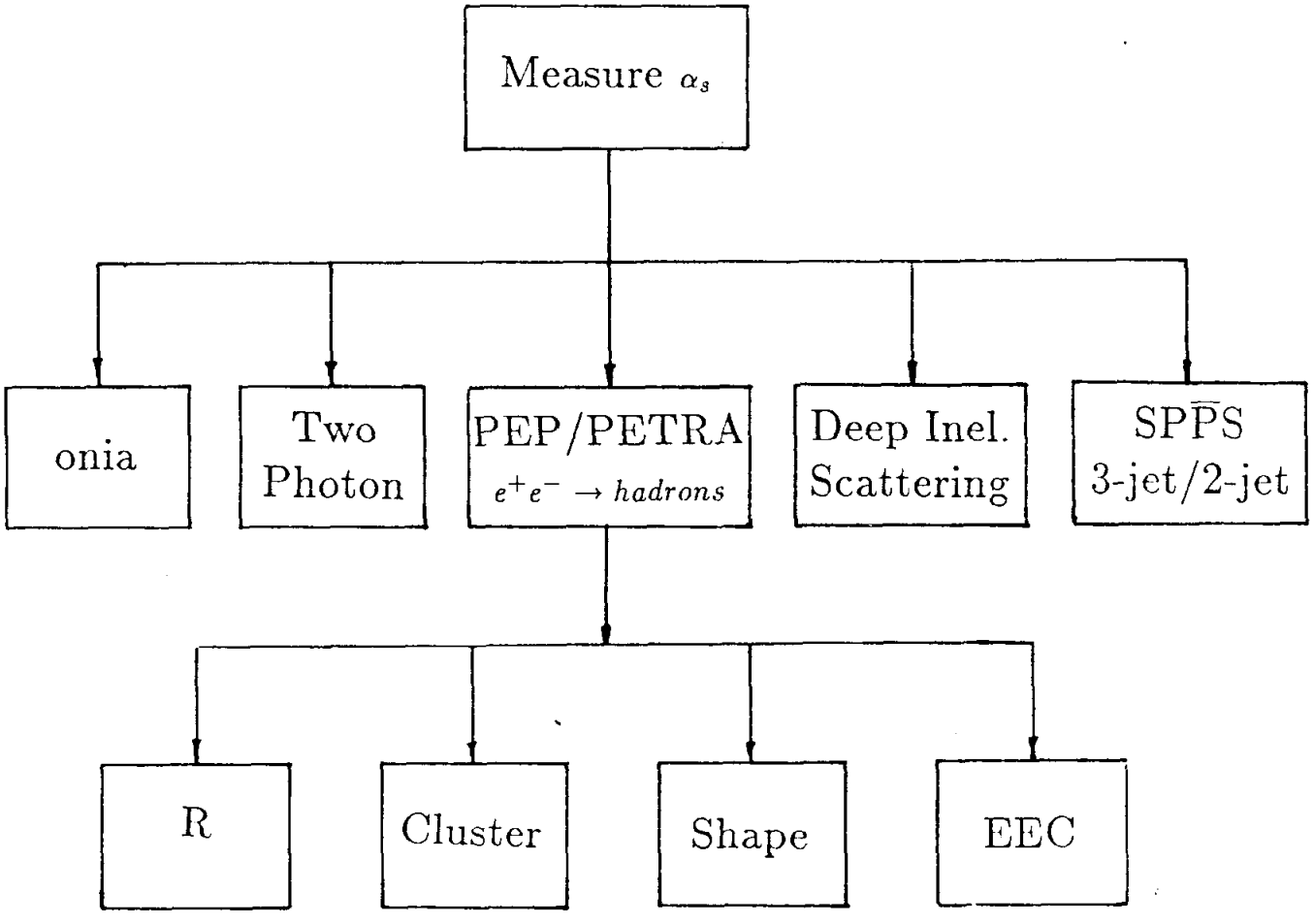

Figure 1.6. Methods of measuring α_s at different accelerators. The onia experiments measure the relative rate of the $\Upsilon(1s)$ into hadrons and muon pairs. The 2γ method, properly a PEP and PETRA experiment, finds the shape of the photon structure function. Deep inelastic experiments, using μ or ν beams, look for scaling violations in the shape of the structure functions. Recently, the UA(1) and UA(2) experiments have begun to measure α_s from the ratio of *3-jet* to *2-jet* events in high $P_\perp$ $P\overline{P}$ collisions. The cluster, shape and energy-energy correlation methods are dependent on fragmentation models. The R measurements have other systematics that limit their statistical significance as α_s measurements.

the type and number of particles resulting from the fragmentation of the primary partons. Another advantage of using energy flow is that the MAC detector is well suited for measuring the event energy configuration. The MAC calorimetry covers $\sim 98\% \cdot 4\pi$ sr of solid angle with a comparatively uniform response. The MAC detector is discussed in the following chapter.

1.3.1 Using Energy Flow to Study Fragmentation Models

Fragmentation models give good agreement with data in the *2-jet* regime: Indeed, the models are constructed to give equivalent predictions for *2-jet* events. However, subtle distinctions between models appear for *3-jet* events. As an example of these distinctions, we look at the energy flow predicted for the very *3-jet*-like configurations; these events have a quark, anti-quark, and gluon, with momenta far apart, and sharing roughly equal energy. This idealized parton configuration is illustrated in Fig. 1.7.

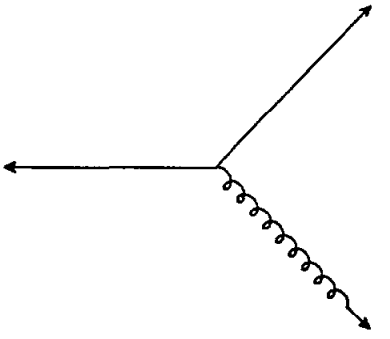

Figure 1.7. Ideal "Mercedes" parton skeleton used to demonstrate differences among fragmentation models. This skeleton is fragmented differently by IJM and STR models.

The model dependence of the fragmentation process can be illustrated by repeatedly fragmenting the configuration of Fig. 1.7 using a particular model. A log-polar histogram of energy flow around the event plane (log radius) vs. the angle around the event plane is presented in Fig. 1.8 for Incoherent Jet (IJM) and String (STR) fragmentation. In the region between the partons, the difference between the models is striking. The Incoherent Jet model tends to give the same energy between the two quark jets as it does between the quark and gluon jets. In contrast, the

String model introduces substantially less energy between the quark jets, for this particular parton configuration. The greater energy deposited between the quark and gluon jets is a general feature of String fragmentation. These features motivate the energy flow part of the analysis.

A method of evaluating fragmentation models then becomes clear: select an event sample enriched in *3-jet* events, determine the gluon quadrant of the event plane, and compare the character of the resultant energy flow with Monte Carlo predictions.

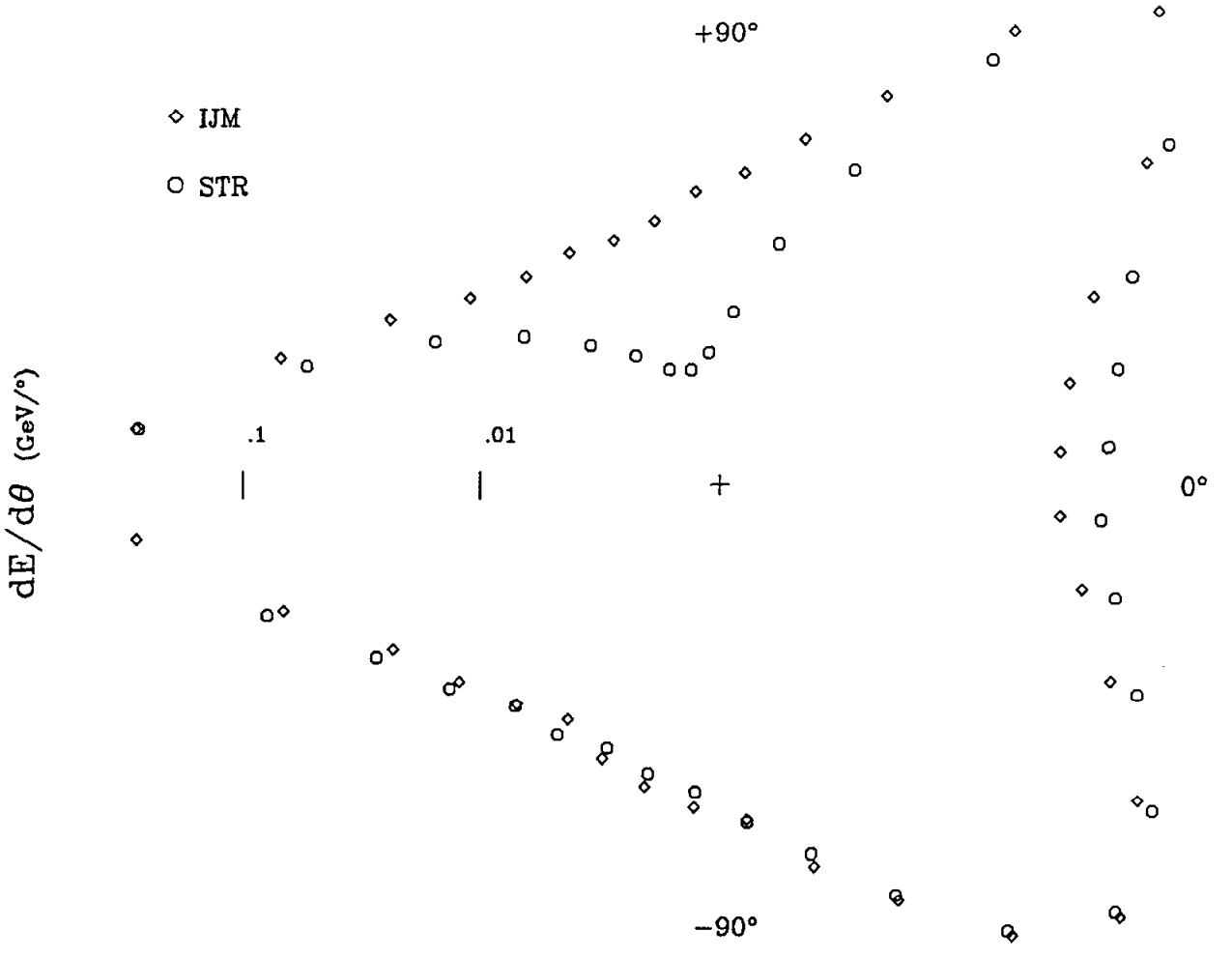

Figure 1.8. Histogram of energy flow around the event plane (log-polar) vs. angle around the plane for Incoherent Jet and String Models. The "Mercedes" skeleton is fragmented repeatedly by IJM or STR models. The energy in the region between the q and $\bar{q}$ jets (around $+90°$) is depleted for STR fragmentation.

2. Experimental Apparatus

2.1 The PEP Storage Ring

PEP (Positron Electron Project)[21] is a 2200 m circumference e^+e^- storage ring at the Stanford Linear Accelerator Center (SLAC). The original SLAC linac is used to inject electrons and positrons into the PEP ring as counter-rotating beams at energies of 14.5 GeV. Each e^+ and e^- beam is made up of three equally spaced bunches, colliding at six interaction regions symmetrically placed around the PEP ring. Looking down on the ring from above, the electrons circulate clockwise, and the positrons circulate counterclockwise. At the fourth interaction region, where the MAC detector takes data, the electrons move south, and the positrons move north. Except for 25 pb^{-1} of data taken at $\sqrt{s}$ of 28 GeV, all the data was taken at $\sqrt{s}$ of 29 GeV. The orbital frequency is 136.269 kHz, which means an e^+ bunch collides with an e^- bunch every 2.4461 μs. Typical e^+ or e^- beam currents are about 15 mA for the sum of the three bunches in a beam. Typical peak luminosities are $20 \times 10^{30}\,cm^{-2}s^{-1}$. The luminosity degrades to $5 \times 10^{30}\,cm^{-2}s^{-1}$ in about 2 hours.

2.2 The MAC Detector

The MAC (Magnetic Calorimeter) detector has been taking data at Interaction Region 4 at the PEP storage ring at SLAC since the turn-on of PEP in the Fall cycle of 1980. Detailed discussions of the MAC hardware may be found in Refs. 22-27. An end view of the central section of the MAC detector is shown in Fig. 2.1 and a side view is shown in Fig. 2.2. These figures will greatly clarify the coming discussion.

A charged particle emerging from the interaction point passes through the beam pipe and is bent by the solenoid field; this curvature is measured by the central drift chamber (CD) and converted into a momentum measurement. After

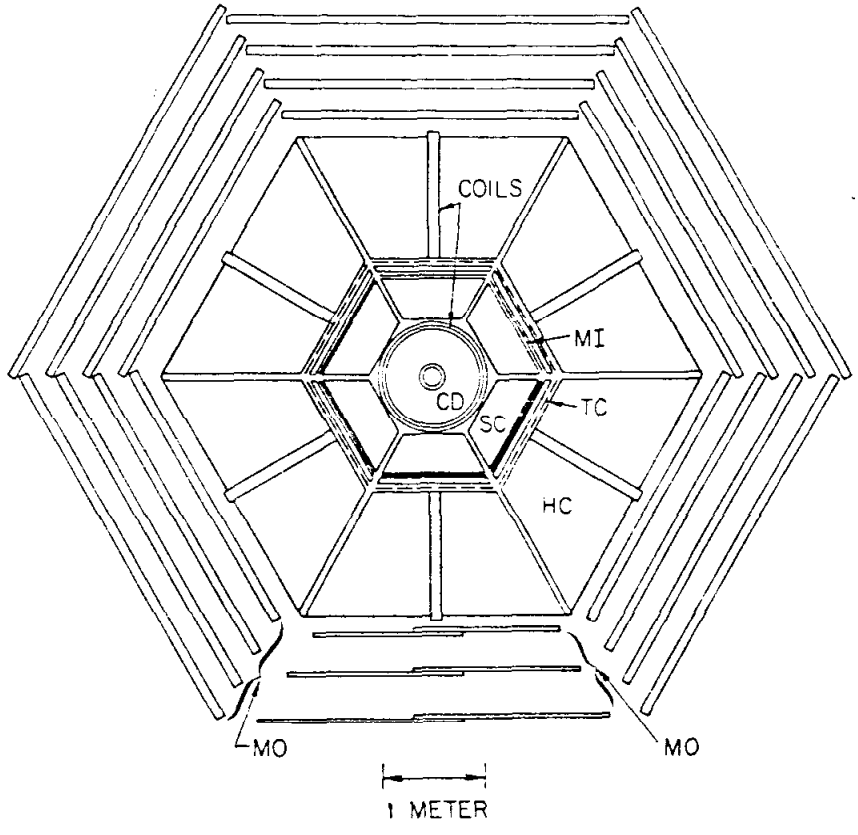

Figure 2.1. End view of the MAC detector illustrating the central section. Key: CD central drift chamber; SC electromagnetic shower chamber; TC trigger counter system; HC hadron calorimeter; MI inner muon drift chambers; MO outer muon drift chambers; EC endcap calorimeter; COILS: shown is the solenoid coil for the central drift chamber and the toroid coil for the muon system.

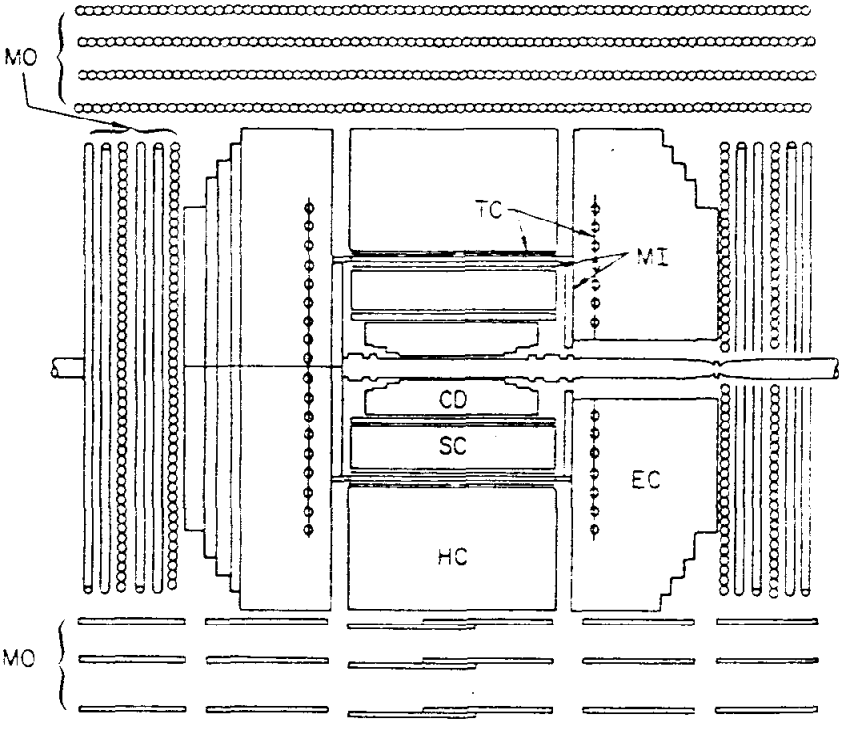

Figure 2.2. Side view of the MAC detector. Key: CD central drift chamber; SC electromagnetic shower chamber; TC trigger counter system; HC hadron calorimeter; MI inner muon drift chambers; MO outer muon drift chambers; EC endcap calorimeter.

passing through the solenoid magnet, energy is deposited in an electromagnetic shower chamber (SC). This is a stack of lead sheets and proportional wire chambers (PWCs) sandwiched together. This system is optimized for reconstructing photon and electron showers. A single layer of drift chambers is used to track the entry point of a particle into the hadron calorimeter steel. Surrounding the shower chambers are rows of scintillator paddles making up the trigger counter (TC) system. Outside of the trigger counters is the hadron calorimeter (HC). This is similar in structure to the SC and is a stack of steel plates and PWCs sandwiched together. The HC, together with the SC, reconstructs the energy of hadron jets. Particles that penetrate the hadron calorimeter steel enter the outer muon drift chambers (MO). This pattern of electromagnetic shower chambers, followed by hadron calorimetry and backed up with a muon drift system is repeated in the endcaps, except that the endcaps (ECs) use steel in both the electromagnetic and hadron calorimeters.

2.2.1 The MAC Detector Subsystems

The detector subsystems are discussed in more detail in the sections following. The MAC coordinate system uses this convention: $\hat{z}$ is north along the positron beam direction; $\hat{x}$ points west towards the center of the PEP ring; and $\hat{y}$ is vertical. The origin of this coordinate system is the nominal interaction point.

2.2.1.1 Central Drift Chamber

The beam pipe containing the PEP vacuum is aluminum tubing approximately 1.8 mm thick, and 18 cm in diameter.[a] The central drift chamber (CD) is composed of 833 double sense wire cells, running the full length of the CD, sharing a common gas volume of 90% argon with 10% methane. The sense wire pairs, kept separated with small epoxy beads, are fed into differential electronics. After the differential amplifier, the signal is split; one signal is fed into Time to Digital Converter (TDC) electronics, another signal is feed into Analog to Digital Converters (ADCs) of dE/dx electronics. The 50 μm sense wires are grouped into 10 layers; four of the layers have cells running parallel to the beam direction, while six of the layers are skewed 3°. The layers skew in the pattern $0°-3°+3°\ \ 0°-3°+3°\ \ 0°-3°+3°\ \ 0°$. These stereo wires allow the track θ angle to be reconstructed. The innermost wire

---

[a] We damaged our aluminum pipe and substituted a small diameter stainless steel beam pipe for a fraction of our data taking.

is at a radius of 12 cm, the outermost at a radius of 45 cm. The length of the outer wire layers is about 190 cm. The inner four layers are shorter than the outer six; layers 1 and 2 are 60% as long; layer 3 is 75% as long, and layer 4 is 75% as long. The 1.9 cm thick stainless steel end plates therefore have a stepped structure. The solenoid field is supplied by an aluminum coil of conventional water cooled design. The solenoid requires 6000 A at 138 V in order to generate a 5.7 kG field parallel to the z-axis.

A charged track traverses all 10 CD layers for polar angles $23° < \theta < 157°$; while 5 layers are crossed for $\theta < 17°$ and $\theta > 163°$. The point cell resolution is 200 μm. The angle errors in θ and ϕ are of the order of 0.1°. For a track traversing all 10 layers, the momentum resolution is given by $\Delta P/P = .065 P \sin\theta$, with P in GeV/c.

2.2.1.2 Electromagnetic Shower Chambers

The hexagonally symmetric shower chamber (SC) system provides full azimuthal coverage. Each sextant is composed of 32 2.5 mm thick lead[b] plates interleaved with PWCs. The 40 μm stainless steel anode wires carry the high voltage. The wires run the length of an open top, grounded aluminum extrusion, each extrusion containing 8 adjacent cells with cell dimensions 1.8 cm wide by 8.6 cm high. The wires are supported at the 1/3 and 2/3 points along each extrusion by a plastic standoff, and at each end by a plastic feedthrough. The segmentation of the SC is illustrated in Fig. 2.3b. The wires in each sextant are grouped into 32 azimuthal wedges. Each wedge is further divided into 3 radial layers, called wire groups, where the first layer is composed of 7 wire planes, the second of 13 wire planes, and the third of 12 wire planes. All ends in a particular wire group are joined in parallel and fed into the input of a low impedance preamp, located on the detector. The preamp outputs are connected to analog sample-and-hold modules (SHAMs)[28] which are in turn read out by an analog-to-digital scanner module (BADC)[29]. The preamp card also outputs an analog sum for use in the hardware and software triggers. The dynamic range of the electronics is such that minimum ionizing tracks and heavily ionizing showers are both within the digitization window. Each end of a wire group is brought out separately. The z-coordinate information of a shower comes from current division. This results in an energy vector $\hat{E}$ for each wire group, derived from the corrected pulse height at each end. The sides,

[b] The lead alloy used has composition 83% Pb, 12% Sb and 5% Sn.

bottom and top of the shower chambers are a thin skin of aluminum that seals the PWCs in a common gas volume. The ends are thick aluminum cover plates that remove with some difficulty to provide access to the feedthroughs. The gas used is 85% argon with 15% methane as the quencher. The solenoid together with the SC comprise approximately 14 X_0 for electrons at normal incidence.

The gain monitoring is automatic. A separate small proportional chamber monitors the gain of the recirculated gas at the exhaust port with the ^{55}Fe 6 KeV X-ray line, and compares this to the gain from a special fiducial gas mixture. Periodically, the computer records temperatures, pressures, voltages and gains. Major deviations from normal are cause for operator action, minor deviations are corrected off-line. The gas gain is monitored to about the 3% level, a factor of 3 better than actual gas gain deviations.

The resolution for electron showers in Bhabha events is $\Delta E/E \sim 20\%/\sqrt{E}$, with E in GeV/c. Bhabha showers were also used to measure the position resolution of the SC system by comparing the position of the shower centroid with tracks in the CD. We find that $\Delta\phi \sim 1°$, and $\Delta z \sim 1\%$ of the wire length.

2.2.1.3 Trigger Counter System

There are 144 single ended photomultiplier tube (PMT) readout scintillator paddles in a single layer surrounding the central section SC and endcap shower system, forming the Trigger Counter (TC) system. Both TDC and ADC information is digitized by standard LeCroy 22nn series CAMAC modules. The scintillator information is used in the trigger and for cosmic ray rejection.

In the central section, the scintillator paddles are arranged like barrel staves around the SC. There are 36 paddles covering the north end of the barrel, and 36 paddles covering the south half. Light signals are fed by Lucite light pipes into Amperex 2230 PMTs, which are arrayed like spokes around the central section end faces.

Each endcap plane just beyond the fifth steel plate is divided into quadrants. In each quadrant there are nine adjacent scintillator paddles forming a single plane. Single ended light signals are piped outside the steel to PMTs and processed in a manner identical to central section signals.

For $15° < \theta < 165°$, the coverage of the TC system is 96%. The timing resolution is about 1 ns.

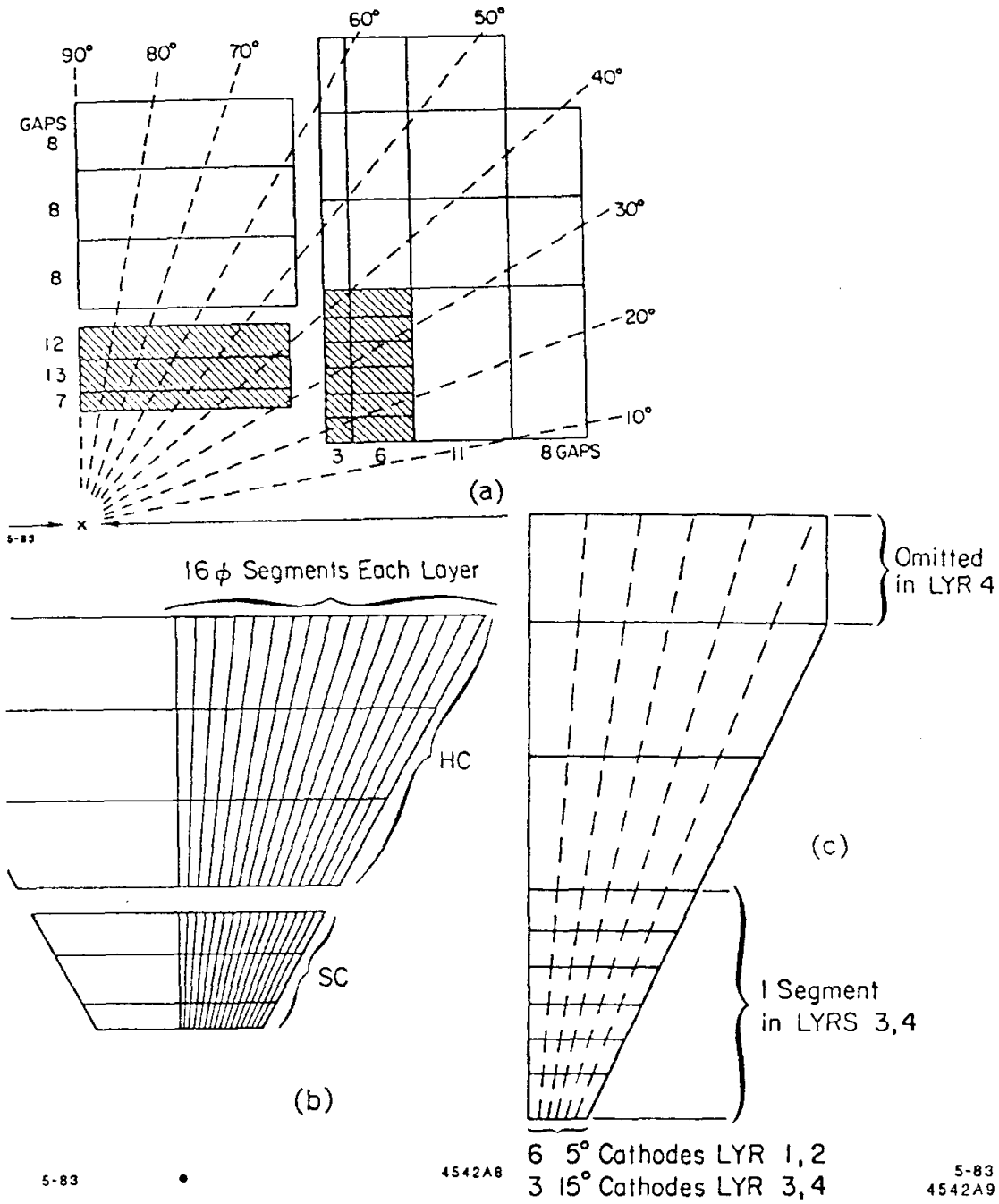

Figure 2.3. Segmentation of the various calorimeters. (a) Side view of the calorimetry. The electromagnetic shower systems are shown shaded. The number of wire planes in each radial layer is also indicated. (b) End view of the central section calorimetry. Each sextant of the SC and HC is divided into 32 azimuthal wedges of anode wires. These are further subdivided into 3 radial layers. (c) End view of the endcap calorimeter. The wire segmentation is discussed in the text.

2.2.1.4 Hadron Calorimeter

The central section Hadron Calorimeter (HC) is composed of six separate stacks of steel sandwiched with PWC planes. Each sextant stack is composed of 24 steel plates 2.5 cm thick, followed by 3 steel plates 10 cm thick, providing a total of 4.3 nuclear interaction lengths from the interaction point through the HC steel, for pions at normal incidence. The PWC modules are slid between the steel plates, each module enclosing a separate gas volume. As in the SC, the anode wires, at +HV, are 40 μm stainless steel, here supported only at the ends of aluminum extrusions by plastic feedthroughs which also serve as bulkheads for the gas connections. Each extrusion is $\sim$ 300 cm long, 20 cm wide, and 1.2 cm high, and enclosing eight side-by-side cells on four sides.

The first three steel plates in each sextant provide flux return for the solenoid field. The remaining steel in each HC sextant is surrounded by a four turn aluminum coil of conventional water cooled design generating a toroid field of 17.5 kG. The three solenoid flux return plates are separated from the remaining steel by an air gap and stainless steel spacers. All the toroid windings (including the toroid endcap windings, discussed later) are wired in series to a 77 V, 2500 A power supply.

The segmentation of the HC wires into wire groups is similar to the SC segmentation. There are 32 azimuthal wedges subdivided into 3 layers of 8 PWC planes per layer, resulting in 96 wire groups in each sextant. The first two layers have two ended output to allow for current division. The third layer is single ended. There is one PWC plane in each of the two gaps between the 10 cm steel plates; these are for muon tagging and are not considered part of the HC energy sums.

The HC has no clean *in situ* calibration signal for the HC, as the Bhabha events provide for the SC. A very similar HC assembly was placed in a test beam,[30] and the resolution measured for various incident pion momenta. The measured resolutions shown in Fig. 2.4 are consistent with a resolution of $\Delta E/E \sim 75\%/\sqrt{E}$, with E in GeV.

2.2.1.5 Muon Tracking

The muon tracking system consists of two parts; layers of drift chambers (MI) just inside the calorimeter steel, and layers of drift chambers (MO) just outside the steel. The MI system is composed of planar aluminum drift chambers. Each cell is 10 cm wide and 2.5 cm tall. The cells contain double sense wires, each 50 μm in diameter and made of gold-plated tungsten, connected to differential amplifiers.

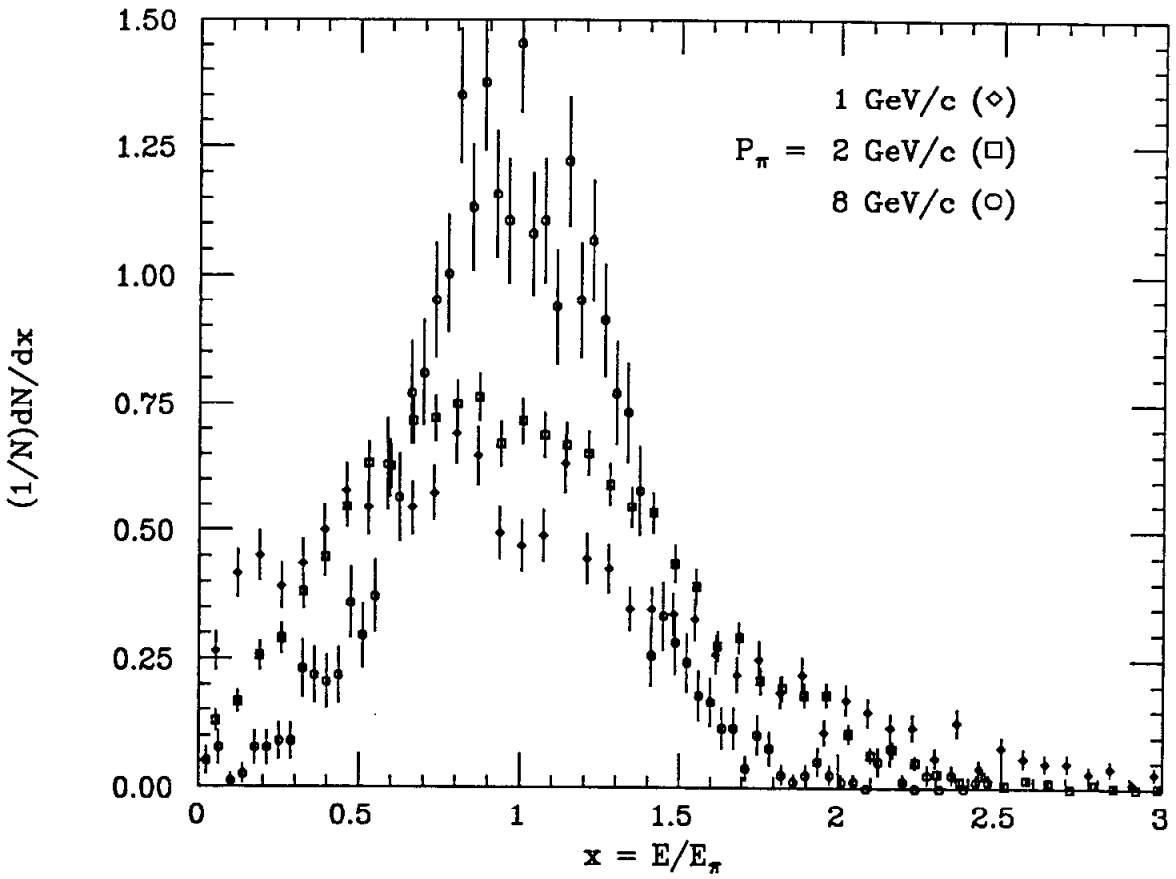

Figure 2.4. Resolution of a prototype HC assembly for a variety of incident of pion momenta. All momenta are consistent with a resolution of $\Delta E/E \sim 75\%/\sqrt{E}$, with E in GeV.

There is a single active layer just inside the central section calorimeter steel, and a triple layer just inside the endcap steel.

The MO system is composed of aluminum drift chambers that track charged particles emerging from the toroidally magnetized steel. There are four layers of drift chambers surrounding all but the bottom central section sextant. The chambers are aluminum drift tubes 10 cm in diameter, with 88 tubes in each sextant layer oriented perpendicular to the beam direction. The tubes have a single anode wire at +HV. The middle two tube layers are offset in the $\hat{z}$ direction by +1 cm and -1 cm in order to resolve the left-right ambiguity. Owing to interference from structural supports, the bottom drift chambers form three layers and are of planar design, similar to the MI chambers. The drift chambers surrounding the endcaps are identical in design to the central section drift tubes. The muon drift system outside of each endcap is divided into six layers. The innermost layer is horizontal, the next layer is rotated around the $\hat{z}$ direction by 60°. This rotation is continued four more times for the remaining layers.

Muons with $P \gtrsim 2$ GeV enter MO chambers and the momentum reconstructed by tracking the muon after being bent by the toroid field in the calorimeter steel. The track is projected back to the z-axis, the curvature computed and the muon momentum deduced. The point resolution in a drift tube is ~ 2 mm. The momentum resolution of the MO system combined with other detector subsystems is given by $\Delta P/P \sim 30\%$, which is dominated by multiple scattering through an angle given by $\theta_0(P) = 0.15\,\text{radian}/P$ with P in GeV/c. This angle corresponds to a deviation of about 1 cm for 14.5 GeV muons at the MO layers.

2.2.1.6 Endcap Calorimeters

The purpose of the endcap system (EC) is to extend the calorimetry to $98\% \cdot 4\pi$ sr. Each endcap is composed of 29 steel plates 2.5 cm thick and 2 steel plates 10 cm thick, sandwiched with PWCs. Aluminum toroid coils encircle each sextant of the endcaps steel, except for the first five steel plates which are used for the solenoid flux return. These coils have the same design as those in the HC system, discussed earlier. Each plane of PWCs is divided into 12 azimuthal wedges, such that two adjacent wedges form the outline of a central section sextant. The PWC system used in the EC generates position information by comparing the single ended anode wire pulse height and the pulse height from cathode strips placed orthogonal to the anodes. Each azimuthal wedge of about 100 50 μm Be-Cu wires

Table 2.1. Approximate factors of SHAM counts per GeV for incident pions, electrons and hadron jets on each of the three SC layers, the HC, the first two layers of the EC shower system, and the hadron part of the EC.

	SC			HC	EC		
	lyr1	lyr2	lyr3		lyr1	lyr2	had
jet	255	230	160	310	170	150	120
π	180	180	180	320	160	160	160
e	350	350	350	425	250	250	250

is divided into five layers in depth, forming wire groups. The first layer contains 3 PWC planes, the second 6 planes, the third 11 planes, the fourth 8 planes, and the last layer, sandwiched between the 10 cm plates, contains only 1 PWC plane used for muon tagging which is not used in the EC energy sums. Each 30° azimuthal segment contains six (layers 1 and 2) or three (layers 3 and 4) aluminum cathode strips. The first nine PWC planes have finer segmentation in order to function as electromagnetic shower chambers, the steel amounting to some $16X_0$. The EC system uses the same gas supply as the SC and HC. Each endcap is approximately 4 nuclear absorption lengths thick for pions at normal incidence.

The EC system can cover polar angles down to about 10° to the beam axis (the exact angle depends on ϕ). The resolution for Bhabha showers into the EC results in $\Delta E/E \sim 53\%/\sqrt{E}$, with E in GeV, over the full azimuthal range. The approximate correction of SHAM counts per GeV for incident pions, electrons and hadron jets incident on the various calorimetric detector components are shown in Table 2.1.

2.2.2 The Trigger System

The MAC trigger system operates off of logic signals generated from trigger counter signals, central drift chamber hits, and energy sums in the calorimetry exceeding certain thresholds. In order to perform crude event reconstruction for the trigger, the detector components are divided logically into smaller subcomponents. In the central section of MAC, the entire azimuth is divided into 18 wedges, each wedge representing a 20° slice. This breakdown for the trigger counters is illustrated in Fig. 2.5 where the following logical variables are defined:

S_i is TRUE when counter i is hit.

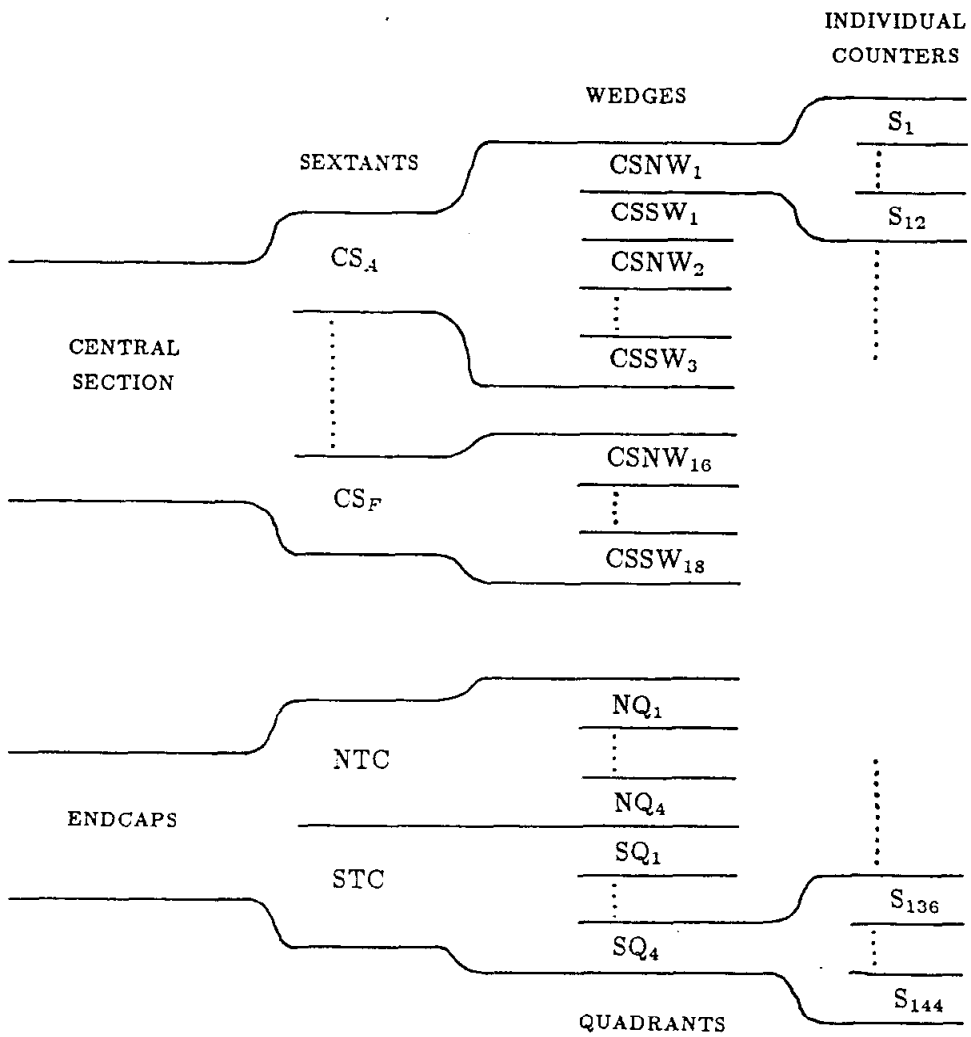

Figure 2.5. Breakdown of signals in the TC logic. These logic signals are used in the triggers. Key: S_i is TRUE when counter i is hit. CS_x is the OR of the twelve counters in central sextant x. $CSNW_n(CSSW_n)$ is the OR of the four north(south) counters in the n^{th} 20° azimuthal wedge of the central section. NTC(STC) is the OR of the 36 counters in the north(south) endcap. $NQ_n(SQ_n)$ is the OR of the 9 counters in the n^{th} quadrant of the north(south) endcap.

CS_x is the OR of the twelve counters in central sextant x.

$CSNW_n$($CSSW_n$) is the OR of the four north(south) counters in the n^{th} 20° azimuthal wedge of the central section.

NTC(STC) is the OR of the 36 counters in the north(south) endcap.

NQ_n(SQ_n) is the OR of the 9 counters in the n^{th} quadrant of the north(south) endcap.

The breakdown of the central drift logic is shown in Fig. 2.6 where the following logical variables are defined:

$SACDW_n$ is TRUE if in CD wedge n, there are ≥ 3 hits in layers 1-5, and there are < 3 hits in layers 5-10.

$LACDW_n$ is TRUE if in CD wedge n, there are ≥ 3 hits in layers 1-5, and there are ≥ 3 hits in layers 5-10.

A track leaving the IR point at a large angle relative to the beam direction and heading towards the central calorimeters should leave hits throughout all the CD layers in a wedge; for such a track $LACDW_n$ is TRUE. Alternately, a track leaving the interaction point at a small angle relative to the beam direction and heading towards the endcap calorimeters should leave hits throughout only the first few CD layers in a wedge; for such a track $SACDW_n$ is TRUE. Using the analog sums from the output of the PWC preamps, the hardware generates energy sub-sums for pieces of the detector geometry. The breakdown of these sub-sums from the PWC systems is shown in Fig. 2.7, where the energy sums are defined by

SC is the energy deposited in the shower chambers.

SC_x is the energy deposited in sextant x of the shower chambers.

HC is the energy deposited in the central hadron calorimeter.

HC_x is the energy deposited in sextant x of the central hadron calorimeter.

NEC(SEC) is the energy deposited in the north(south) endcap.

NECS(SECS) is the energy deposited in the finely segmented electromagnetic part of the north(south) endcap calorimeter.

$NECS_x$($SECS_x$) is the energy deposited in sextant x of the finely segmented electromagnetic part of the north(south) endcap calorimeter.

NECH(SECH) is the energy deposited in the remaining hadron part of the north(south) endcap calorimeter.

$NECH_x$($SECH_x$) is the energy deposited in sextant x of the remaining hadron part of the north(south) endcap calorimeter.

Note that these energy sums are scalar variables. The trigger logic generates logical

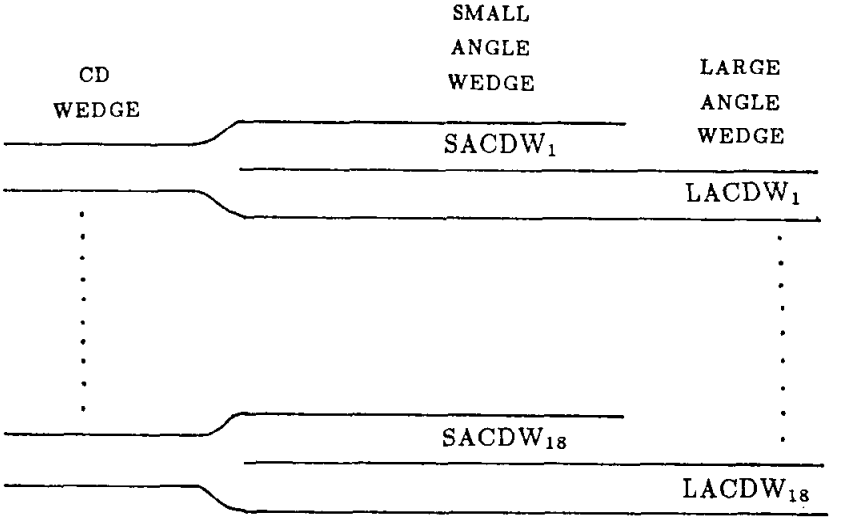

Figure 2.6. Breakdown of signals in the CD logic. These wedge logic bits are used to form the triggers. Key: SACDW_n is TRUE if in CD wedge n, there are ≥ 3 hits in layers 1-5, and there are < 3 hits in layers 5-10. LACDW_n is TRUE if in CD wedge n, there are ≥ 3 hits in layers 1-5, and there are ≥ 3 hits in layers 5-10.

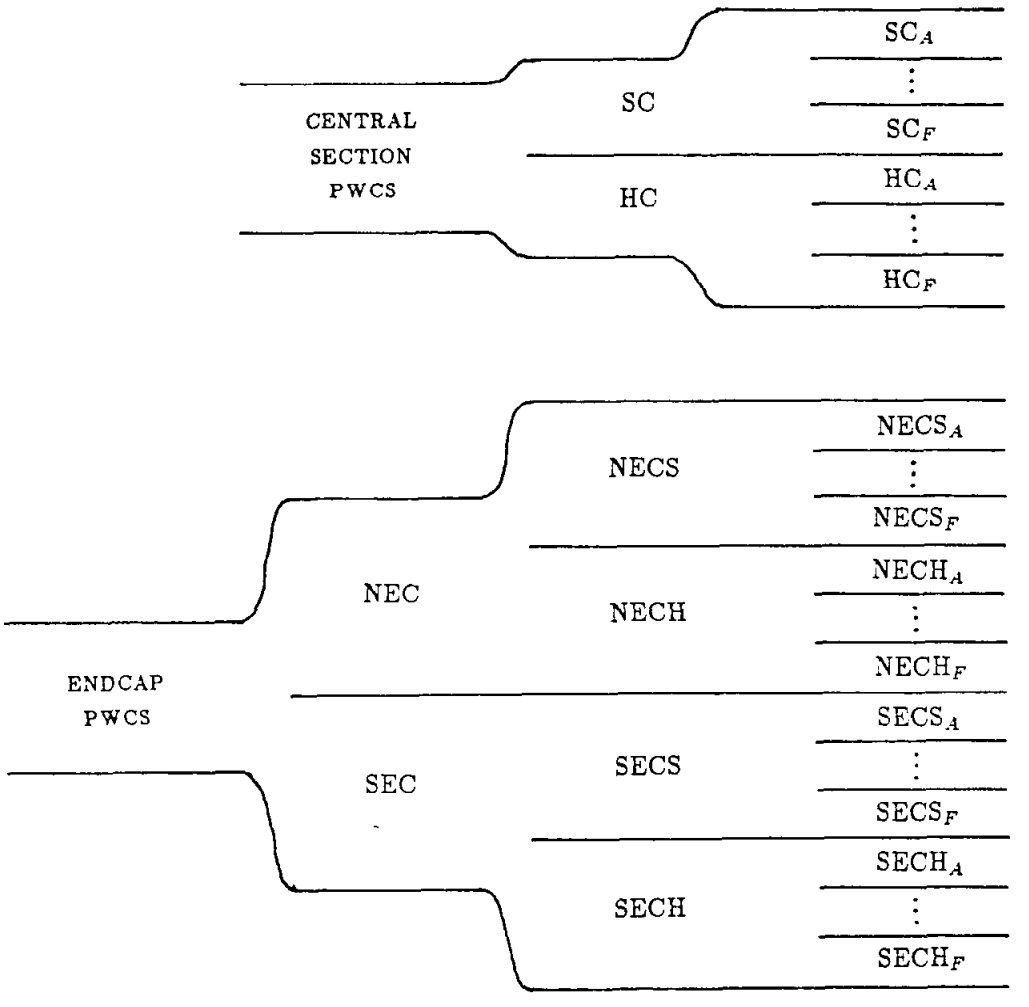

Figure 2.7. Breakdown of the PWC energy sub-sums. These analog sub-sums set logic bits for the trigger when they exceed certain thresholds. Key: SC is the energy deposited in the shower chambers. SC_x is the energy deposited in sextant x of the shower chambers. HC is the energy deposited in the central hadron calorimeter. HC_x is the energy deposited in sextant x of the central hadron calorimeter. NEC(SEC) is the energy deposited in the north(south) endcap. NECS(SECS) is the energy deposited in the finely segmented electromagnetic part of the north(south) endcap calorimeter. $NECS_x(SECS_x)$ is the energy deposited in sextant x of the finely segmented electromagnetic part of the north(south) endcap calorimeter. NECH(SECH) is the energy deposited in the remaining hadron part of the north(south) endcap calorimeter. $NECH_x(SECH_x)$ is the energy deposited in sextant x of the remaining hadron part of the north(south) endcap calorimeter.

variables from them when they exceed certain energy thresholds.

2.2.2.1 Hardware Trigger

The MAC hardware can signal the data acquisition system in three distinct ways. There can be triggers generated before the subsequent beam crossing. This is the fast trigger from the TC system. Other hardware triggers develop after the normal system reset is asserted. In order to prevent this reset from occurring, the trigger can generate a pause from earlier stages in its logic. This pause inhibits all system resets and gates in order to preserve the integrity of the nascent data until a hardware trigger decision is reached. A trigger formed after a pause is called a slow trigger.

Certain logic in the TC system can be generated with extremely fast NIM based comparator electronics. This logic comprises the Fast Scintillator Trigger (T_{scin}). The purpose of T_{scin} is to trigger on back-to-back charged particles that penetrate through the shower chambers into the scintillators. This type of trigger is designed for highly efficient $\mu^+\mu^-$ selection, though it also has high efficiency for the hadronic events used in this analysis. In terms of the logical flags defined in Fig. 2.5, T_{scin} is given by

$$\begin{aligned} T_{scin} =& (\mathrm{CS}_1 \cdot \mathrm{CS}_4) + \ldots + (\mathrm{CS}_3 \cdot \mathrm{CS}_6) \\ &+ (\mathrm{NQ}_1 \cdot \mathrm{SQ}_3) + \ldots + (\mathrm{NQ}_4 \cdot \mathrm{SQ}_2) \\ &+ \{\geq 3 \text{ of } (\mathrm{CS}_1, \ldots, \mathrm{CS}_6, \mathrm{NTC}, \mathrm{STC})\} \quad . \end{aligned}$$

This fast trigger is formed about 200 ns after the beam crossing, and runs at about 2 Hz.

Other hardware triggers take so long to fully form that they are asserted after the system reset would have occurred. While these triggers are forming, they generate pauses. There are three types of pauses that may be generated. First, there is a pause from any scintillator firing

$$P_{scin} = (\mathrm{S}_1 + \mathrm{S}_2 + \ldots + \mathrm{S}_{144}) \quad .$$

This pause runs at 200 Hz to 1000 Hz. A second pause is the neutral pause;

significant shower energy without a scintillator firing. This is defined by

$$P_{neut} = \overline{P_{scin}} \cdot \{\geq 2 \text{ of } (\mathrm{SC}_A > 500\,\mathrm{MeV}), \ldots, (\mathrm{CS}_B > 500\,\mathrm{MeV}), (\mathrm{NEC} > 500\,\mathrm{MeV}), (\mathrm{SEC} > 500\,\mathrm{MeV})\}.$$

This pause runs at about 3 Hz. The final pause is the CD pause, generated by evidence of activity in the CD. This pause requires two active CD wedges at least 90° apart and is defined by

$$P_{CD} = \{\geq 2 \text{ of } (\mathrm{LACDW}_1, \ldots, \mathrm{LACDW}_{18}) > 90^\circ \text{ apart}\} \quad .$$

This pause runs at 30-50 Hz.

Once the slow triggers assert a pause and inhibit further resets and gates, they can take one more beam crossing before asserting a trigger or allowing the MAC system to clear. The slow triggers provide crude tracking between the CD, TC and calorimeter elements.

The trigger that is most efficient for selecting multihadrons is the energy trigger, which simply demands a minimum energy deposition in two sections of the calorimetry and associated TC activity to accompany the endcap energy in order to provide for cosmic ray rejection. The energy trigger is defined by

$$\begin{aligned} T_{ener} \quad = \quad & \geq 2 \text{ of } \{\mathrm{SC}_A > 1.5\,\mathrm{GeV}, \ldots, \mathrm{SC}_F > 1.5\,\mathrm{GeV}, \\ & (\mathrm{CS}_A + \ldots + \mathrm{CS}_F) \cdot (\mathrm{HC} > 4.0\,\mathrm{GeV}), \\ & (\mathrm{NTC} \cdot \mathrm{NEC} > 2.8\,\mathrm{GeV}), \\ & (\mathrm{STC} \cdot \mathrm{SEC} > 2.8\,\mathrm{GeV})\} \quad . \end{aligned}$$

This trigger runs at approximately 1 Hz.

Another trigger is optimized for muon track selection. This is called the grand crate trigger and requires a CD wedge aligned (or nearly aligned) with a scintillator wedge and corresponding energy deposition in the calorimetry. The formal trigger

definition is

$$
\begin{aligned}
T_{GC} = \sum_{i=1}^{18} \mathrm{LACDW}_i \cdot \{ & \ \mathrm{CSNW}_i \cdot (\mathrm{HC}_{x(i)} > 500\,\mathrm{MeV}) + (\mathrm{NECH}_{x(i)} > 500\,\mathrm{MeV}) \\
& + \mathrm{CSSW}_i \cdot (\mathrm{HC}_{x(i)} > 500\,\mathrm{MeV}) + (\mathrm{SECH}_{x(i)} > 500\,\mathrm{MeV}) \\
& + \mathrm{CSNW}_{i+1} \cdot (\mathrm{HC}_{x(i)} > 500\,\mathrm{MeV}) + (\mathrm{NECH}_{x(i)} > 500\,\mathrm{MeV}) \\
& + \mathrm{CSSW}_{i+1} \cdot (\mathrm{HC}_{x(i)} > 500\,\mathrm{MeV}) + (\mathrm{SECH}_{x(i)} > 500\,MeV) \\
& + \mathrm{CSNW}_{i-1} \cdot (\mathrm{HC}_{x(i)} > 500\,\mathrm{MeV}) + (\mathrm{NECH}_{x(i)} > 500\,\mathrm{MeV}) \\
& + \mathrm{CSSW}_{i-1} \cdot (\mathrm{HC}_{x(i)} > 500\,\mathrm{MeV}) + (\mathrm{SECH}_{x(i)} > 500\,\mathrm{MeV}) \} \\
+ \sum_{i=1}^{18} \mathrm{SACDW}_i \cdot \{ & \mathrm{NQ}_{\ell(i)} \cdot \mathrm{NECH} > 500\,\mathrm{MeV} + \mathrm{SQ}_{\ell(i)} \cdot \mathrm{SECH} > 500\,\mathrm{MeV} \}
\end{aligned}
$$

where $x(i)$ is the k^{th} sextant containing wedge i. This trigger runs at about 2 Hz.

Yet another trigger providing events for this analysis is CD·SHOW2, which by demanding some CD activity with some associated shower chamber activity, is efficient for selecting 2γ hadron events. This trigger again has a high efficiency for single photon multihadrons. The trigger is defined by

$$
\begin{aligned}
T_{CD\cdot SHOW2} = & P_{CD} \\
& \cdot \{ \geq 2 \text{ of } (\mathrm{LACDW}_1, \ldots, \mathrm{LACDW}_{18}) > 90^\circ \text{ apart} \} \\
& \cdot \{ \geq 2 \text{ of } (\mathrm{SC}_A > 500\,\mathrm{MeV}), \ldots, (\mathrm{SC}_F > 500\,\mathrm{MeV}), \\
& \qquad (\mathrm{NECS}_A > 500\,\mathrm{MeV}), \ldots, (\mathrm{NECS}_F > 500\,\mathrm{MeV}), \\
& \qquad (\mathrm{SECS}_A > 500\,\mathrm{MeV}), \ldots, (\mathrm{SECS}_F > 500\,\mathrm{MeV}) \} \quad .
\end{aligned}
$$

This trigger runs at about 1 Hz.

In addition to the above triggers, there are additional triggers designed to select very specialized event topologies, and a random trigger that fires every few seconds as a diagnostic aid. Note that for multihadrons, there is a tremendous redundancy in terms of the overlap of three separately very efficient triggers. The overall trigger rate with typical beam conditions is $\sim$ 5 Hz. The CAMAC based electronics requires $\gtrsim$20 ms to read in a typical event record, resulting in a dead time of about 10%.

2.2.2.2 Software Trigger

An interrupt from a hardware trigger signals the data acquisition computer (a VAX 11/780) to initiate a DMA read operation from the CAMAC data bus. The

pedestal subtraction mode of BADC operation is used for data compression. The software trigger examines events accepted by the hardware trigger in more detail, but no detailed event reconstruction is done. Instead, the software trigger looks for coincidences between active sub-elements of the detector (the breakdown into logical sub-elements is shown in Figs. 2.5-2.7). In most cases the software trigger is a tighter and more sophisticated version of the hardware trigger counterpart. The software triggers also begin to assign events to physics catagories; a certain trigger might be highly enriched with low angle Bhabha events, for instance. At any time, there are about 20 active software triggers. The absolute number varies as test and special purpose triggers are occasionally added, while moribund triggers are removed. The software triggers for selecting multihadrons, however, have remained relatively constant. This discussion will concentrate on the software triggers with high efficiency for multihadrons.

The software version of the GC trigger has the same logic as the hardware trigger. This is also true for the CD·SHOW2 trigger.

Any event is passed by a software trigger that passes events with back-to-back showers. This trigger is formally given by

$$
\begin{aligned}
T = {} & (\mathrm{SC}_A > 500\,\mathrm{MeV}) \cdot (SC_D > 500\,\mathrm{MeV}) + \\
& \quad \ldots + (\mathrm{SC}_C > 500\,\mathrm{MeV}) \cdot (SC_F > 500\,\mathrm{MeV}) \\
& + \{(\mathrm{NECS}_A + \mathrm{NECH}_A) > 500\,\mathrm{MeV}\} \\
& \quad \cdot \{(\mathrm{SECS}_D + \mathrm{SECH}_D) > 500\,\mathrm{MeV}\} + \\
& \quad \vdots \\
& + \{(\mathrm{NECS}_F + \mathrm{NECH}_F) > 500\,\mathrm{MeV}\} \\
& \quad \cdot \{(\mathrm{SECS}_C + \mathrm{SECH}_C) > 500\,\mathrm{MeV}\} \quad .
\end{aligned}
$$

The software equivalent of the ENER trigger is more sophisticated. If the calorimetric energy is below threshold, the event will still pass if there is associated

CD and TC activity. The formal definition of this software trigger is given by

$$
\begin{aligned}
T = & T_{ener} \\
& + (\mathrm{SC} > 2.5\,\mathrm{GeV}) \\
& + \sum_{i=1}^{18} \mathrm{LACDW}_i \cdot (\mathrm{CSNW}_i + \mathrm{CSSW}_i) \\
& + \sum_{i=1}^{18} \mathrm{SACDW}_i \cdot (\mathrm{NQ}_{\ell(i)} + \mathrm{SQ}_{\ell(i)}) \\
& + \{(\mathrm{SC} + \mathrm{HC} + \mathrm{NEC} + \mathrm{SEC}) > 10.0\,\mathrm{GeV}\} \quad .
\end{aligned}
$$

For the SCIN hardware trigger to pass events from the software trigger, there must be associated CD activity or energy deposition. The trigger is defined as

$$
\begin{aligned}
T = & T_{scin} \\
& + \{\mathrm{NQ}_1 + \mathrm{NEC} > 500\,\mathrm{MeV}\} \\
& \quad \cdot \{\mathrm{SQ}_3 + \mathrm{SEC} > 500\,\mathrm{MeV}\} + \\
& \vdots \\
& + \{\mathrm{NQ}_4 + \mathrm{NEC} > 500\,\mathrm{MeV}\} \\
& \quad \cdot \{\mathrm{SQ}_2 + \mathrm{SEC} > 500\,\mathrm{MeV}\} \\
& + \sum_{i=1}^{18} \mathrm{LACDW}_i \cdot (\mathrm{CSNW}_i + \mathrm{CSSW}_i) \\
& + \sum_{i=1}^{18} \mathrm{SACDW}_i \cdot (\mathrm{NQ}_{\ell(i)} + \mathrm{SQ}_{\ell(i)}) \quad .
\end{aligned}
$$

For diagnostic purposes, typically every 100^{th} hardware trigger is passed unconditionally. The acceptance of the software trigger depends on the beam conditions and PEP luminosity. A typical acceptance is $\sim$ 60%. The overall efficiency through both levels of triggers, for the type of multihadron events used in this analysis, approaches 100%.

2.2.3 Post-trigger Event Handling

An event record is typically 2 kbyte long and is logged on a temporary disk file on the VAX. At the end of each ~2 hour run, the ~15k events in the data file

are transmitted over a high speed (approximately 50 kbaud) link to an IBM 3081K mainframe computer located on the SLAC site. The IBM spools the data file to a temporary disk file, and proceeds to archive the data on 6250 bpi tape. Once the archive tape is written on the IBM, the VAX is free to erase the local disk file. This elegant data path frees the lone MAC shift operator from tape handling.

Events in the IBM data files are then passed through filtering software to separate clean events from cosmic rays, beam gas and other junk events. This filtering performs detailed reconstruction of the event, generates data summary records, and appends flags to the event to indicate specific "masks" are satisfied. The "masks" are divided into levels. An event must satisfy at least one level-1 mask in order to pass the filter. Additional levels of "masks" are informational flags that, once appended to the event, allow very fast selection of events with specified combinations of mask bits set on or off. The off-line filter passes about 10% of the events. Information on the off-line filter may be found in Ref. 27. The overall structure of the MAC data flow system is shown in Fig. 2.8. The selection of events for this analysis from these filtered events is described in Chapt. 3 and Chapt. 5.

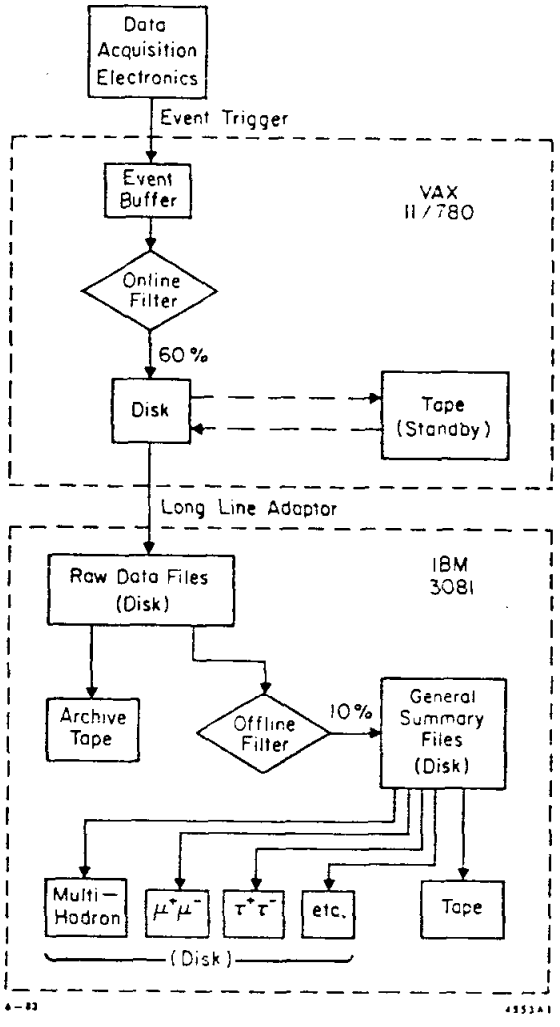

Figure 2.8. The MAC data flow structure. The transfer of data between the VAX 11/780, situated at the experiment, and an IBM 3081/K, the main SLAC computer, is completely automated.

3. Event Selection for the α_s Study

This analysis uses data taken through the Spring of 1984 with the MAC detector at the PEP e^+e^- storage ring operating at $\sqrt{s} = 29\,\mathrm{GeV}$. The integrated luminosity is about $220\,\mathrm{pb}^{-1}$, corresponding to approximately 120k one-photon e^+e^- annihilation events. This large sample of hadronic events permits the use of tight cuts, removing almost all backgrounds and events capable of introducing bias, without statistically limiting the analysis. The event selection for the α_s study proceeds in two consecutive steps:

Hadron Filter–Select all possible one photon annihilation hadronic events consistent with background contamination of only a few percent.

Quality Filter–Select hadronic events that will introduce minimal bias in the thrust direction and event plane determination, while simultaneously reducing much of the remaining backgrounds.

The surviving multihadron events are well reconstructed, and don't require substantial corrections for detector bias. Additionally, events passing these filters are used as input to a *3-jet* filter, described in Chapt. 5.

3.1 Definitions

The thrust axis used is in the sense of Ref. 31:

$$T = \frac{\max_{|\hat{n}|=1} \sum_i |\hat{n} \cdot \vec{E}_i|}{E_{vis}} \qquad \begin{array}{l} i \text{ runs over all 2-ended calorimeter hits,} \\ \text{and } E_{vis} = \sum_i |\vec{E}_i|. \end{array}$$

where calorimetric vectors replace momentum vectors used in the original definition. Single ended calorimeter hits typically account for less than 1 GeV of the visible energy deposition. To determine the thrust direction, the orientation of the unit vector $\hat{n}$ is varied in order to maximize the quantity T. The resultant maximal T is the thrust value, and the corresponding $\hat{n}$ is the thrust axis direction, $\hat{T}$. Notice there are two opposite choices for $\hat{n}$ that yield the same maximal thrust value. $\hat{T}$ is chosen at random between the two.

If the thrust calculation is repeated, with the added constraint that $\hat{n}\cdot\hat{T} = 0$, the resultant quantities are T_{maj}, the value of the major axis, and $\hat{T}_{maj}$, the direction of the major axis. Here again, the ambiguity as to which of the two directions $\hat{T}_{maj}$ will take is decided at random.

The minor axis is defined in the relation $\hat{T}_{min} \equiv \hat{T} \times \hat{T}_{maj}$. The value of the minor axis is generated in a similar way as,

$$T_{min} = \frac{\sum_i |\hat{T}_{min} \cdot \vec{E}_i|}{E_{vis}} \qquad i \text{ runs over all 2-ended calorimeter hits.}$$

These thrust related axes have an approximate physical interpretation when applied to the initial partons. $\hat{T}$ corresponds to a direction either parallel or antiparallel to the direction of the harder of the two primary quarks. $\hat{T}_{maj}$ and $\hat{T}$ together define the parton event plane. $\hat{T}_{min}$ is normal to the parton event plane. These orthonormal unit vectors are diagrammed in Fig. 3.1 for an α_s^1 parton skeleton. An appendix contains a more detailed discussion of the thrust algorithm employed in this analysis.

Two useful hemispheric energy flow moments are given by

$$hE_{\perp}^{in}\begin{pmatrix} one \\ side \end{pmatrix} \equiv \sum_i |\vec{E}_i \cdot \hat{T}_{maj}| \qquad \begin{array}{l} i \text{ runs over all two-ended calorimeter hits} \\ \text{on the same side of the event relative to} \\ \text{the thrust axis} \end{array}$$

and

$$hE_{\perp}^{in}\begin{pmatrix} other \\ side \end{pmatrix} \equiv \sum_i |\vec{E}_i \cdot \hat{T}_{maj}| \qquad \begin{array}{l} i \text{ runs over all two-ended calorimeter hits} \\ \text{on the other side of the event relative to} \\ \text{the thrust axis} \end{array}$$

To account for instrumental fluctuations in calorimeter response, a scaled energy flow is frequently used in this analysis. The scaled moments, normalized to the visible energy, are given by

$$X\begin{pmatrix} one \\ side \end{pmatrix} = \frac{hE_{\perp}^{in}\begin{pmatrix} one \\ side \end{pmatrix}}{E_{vis}} \qquad \text{and} \qquad X\begin{pmatrix} other \\ side \end{pmatrix} = \frac{hE_{\perp}^{in}\begin{pmatrix} other \\ side \end{pmatrix}}{E_{vis}} \quad ,$$

where E_{vis} is the calorimetric energy for the whole event.

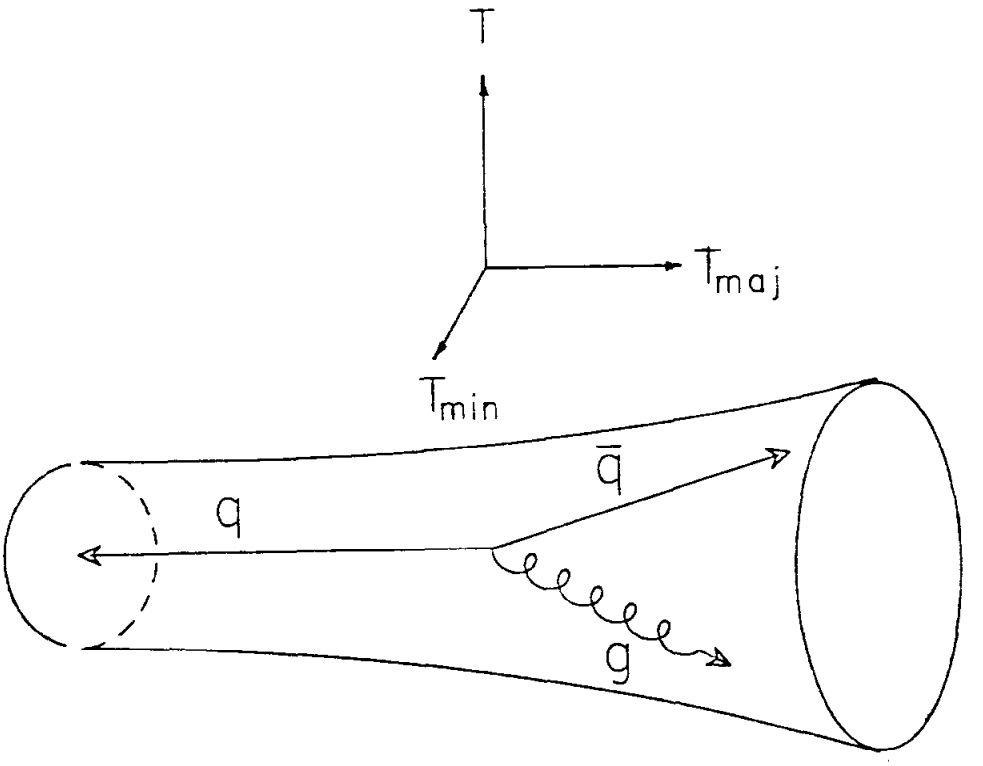

Figure 3.1. Thrust related directions applied to an α_s^1 parton skeleton. The thrust axis $\hat{T}$ is along the "long" axis of the event. The event plane contains $\hat{T}$ and the major axis, $\hat{T}_{maj}$. The normal to the event plane is the minor axis, $\hat{T}_{min}$.

3.2 The MAC Database

This analysis uses approximately $220\,\mathrm{pb}^{-1}$ of e^+e^- annihilation data taken at $\sqrt{s}$ of 29 GeV. This integrated luminosity yielded approximately 40M triggers which were written to archival tape. They were filtered down to approximately 4 M "physics" events stored in the MAC database. The event selection leading to these 4 M events was described in the previous chapter. Further filtering gave a sample of approximately $100K$ hadronic events. The hadron filter is discussed in the next section. The remaining filtering is specific to this analysis. The filter used to select events for the α_s measurement is described later in this chapter. Events used for the α_s measurement were filtered again to produce the event sample used for the energy flow study. Details of this filter are given in chapter 5.

3.3 Hadron Filter

Multihadron events are selected with the hadron filter, a set of cuts to select events arising from one photon annihilation into hadrons, over a broad range of particle multiplicities and production angles. The event selection for the hadron filter has been previously detailed;[26] only a brief review is offered below for completeness.

The following quantities will be used as the basis of cuts in the hadron filter:

- $E_{vis} = \sum_{i=1}^{N} |\vec{E}_i|$, where N, 2-ended calorimeter hits are used in the summation;
- $E_\perp = \sum_{i=1}^{N} |E_{i\perp}|$ is the transverse energy;
- $I = |\sum_{i=1}^{N} \vec{E}_i| / E_{vis}$ is the energy imbalance;
- $\rho_{sum} = \sum_{i=1}^{M_{ch}} |\vec{P}_i|$, where M_{ch} charged tracks are used in the summation;
- Z_v is the z-position of the event vertex;
- $H_{cd} =$ (number of CD hits)$/M_{ch}$ is the average number of drift chamber hits;
- $\rho_{cal} = \frac{1}{N} \sum_{i=1}^{N} |\vec{E}_i|$ is the average energy per calorimeter hit; and
- E_{had} is the sum the energy in the hadron part of the calorimetry.

With the above quantities, we construct a set of loose and tight cuts, the philosophy being that an event passing the tight cuts is very likely to be a single photon multihadron event, while an event failing the loose cuts is likely to be a background event. The precise placement of the loose and tight cuts is given in Table 3.1. An event failing the loose cuts is rejected. Events passing the loose cuts are subjected to the selection logic shown in Fig. 3.2. The hadron filter is estimated to be $\sim 78\%$

Table 3.1. Cuts used in the hadron filter. Events passing all the tight cuts are accepted. Events failing any of the loose cuts are rejected. Events passing all loose cuts, but only some of the tight cuts, are either rejected or subject to hand scanning, depending on the particular tight cuts failed.

cut	loose	tight
E_{vis}	$> 12\,\mathrm{GeV}$	$> 15\,\mathrm{GeV}$
$E_{\perp}$	$> 7.5\,\mathrm{GeV}$	$> 9.1\,\mathrm{GeV}$
I	< 0.65	< 0.55
M_{ch}	≥ 3	≥ 5
P_{sum}	$> 2.0\,\mathrm{GeV/c}$	$> 4.5\,\mathrm{GeV/c}$
$\lvert Z_v \rvert$	$< 5\ cm$	$< 5\ cm$
H_{cd}	> 5.75	> 6.30
ρ_{cal}	$< 1.1\,\mathrm{GeV}$	$< 0.7\,\mathrm{GeV}$
E_{had}	no cut	$> 1.5\,\mathrm{GeV}$

efficient, and to allow only $\sim 3\%$ contamination, mostly by 2γ ($\sim 2\%$) and $\tau^+\tau^-$ events ($\sim 1\%$). The hadron filter passed 100475 events out of the $220\,\mathrm{pb}^{-1}$ sample.

3.4 Quality Filter

The detector response, owing to the barrel-like segmentation and construction of the apparatus, is very uniform in ϕ, but less uniform in θ. The central calorimeters cover the approximate angular range $60^\circ < \theta < 120^\circ$ away from the beam (see Fig. 2.3). The region $30^\circ < \theta < 60^\circ$ and $120^\circ < \theta < 150^\circ$ is a transition region between the central and end-cap calorimeters, and is responsible for variations in calorimeter response. For thrust angles in the range $\theta < 30^\circ$ and $\theta > 150^\circ$, energy is likely to be lost in the direction of the beam-pipe.

Our analysis requires unbiased reconstruction of thrust direction and event plane orientation. The most uniform calorimeter response, with the smallest energy leakage, is achieved within the MAC central calorimeters. The quality filter is therefore designed to select hadronic events with thrust directions constrained to the central section, and event planes near perpendicular to the beam direction.

3.4.1 Formal Cuts for the Quality Filter

The quality filter cuts are given in Table 3.2 in terms of the following quantities:

$\theta_{thrust} \equiv \theta$ of the thrust axis

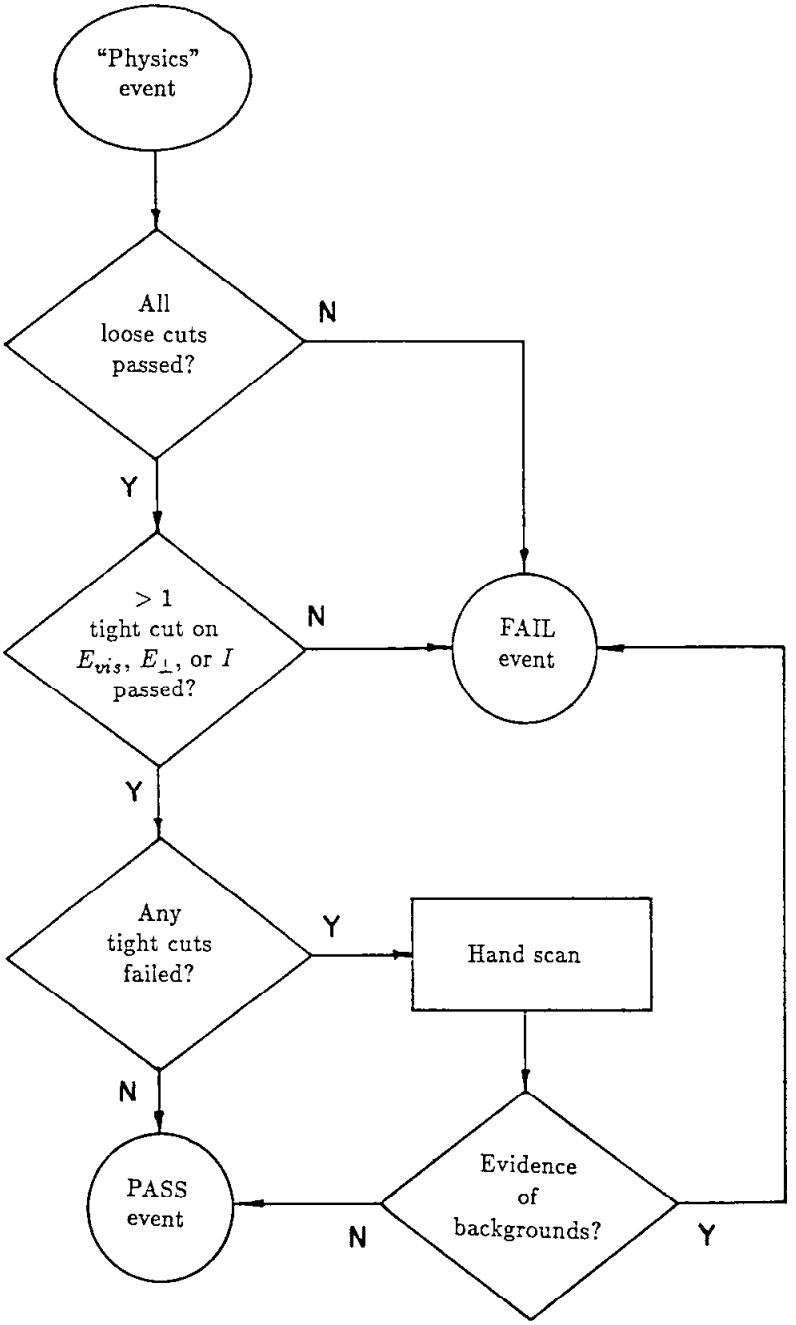

Figure 3.2. The logic of the hadron filter. Events failing any loose cut are discarded. Events passing all the tight cuts are accepted. Events passing all loose cuts, but only some of the tight cuts, are either rejected or subject to hand scanning, depending on the particular tight cuts failed.

Table 3.2. Cuts used for the quality filter. These cuts orient the event plane to lie approximately transverse to the beam, and ensure that almost all of the event energy is deposited in the central calorimeters. The energy flow of these events is minimally distorted by the detector.

$60° < \theta_{thrust} < 120°$
$E_{EC}/E_{CC} < 0.25$
$24\,\text{GeV} < E_{vis} < 34\,\text{GeV}$

$E_{vis} \equiv \sum_i |\vec{E}_i|$, i runs over all 2-ended calorimeter hits

$E_{EC} \equiv \sum_i |\vec{E}_i|$, i runs over all hits in the end-cap calorimeters

$E_{CC} \equiv \sum_i |\vec{E}_i|$, i runs over all hits in the central calorimeters

The thrust direction cut selects events depositing energy primarily in the central calorimeters. The cut on E_{EC}/E_{CC} further constrains energy deposition to be in the central calorimeters, and also tends to orient the event plane to lie perpendicular to the beam direction, so that the event plane is within the central calorimeters. The E_{vis} cut minimizes large gain fluctuations and cuts out 2γ contamination. Figure 3.3 indicates the placement of the various cuts. The correlations between the cuts in the quality filter are given in Table 3.3. Several hundred events were hand scanned. There was no evidence of backgrounds in the sample.

3.4.2 Acceptance

The cuts on θ_{thrust}, E_{EC}/E_{CC} and E_{vis} each pass about 50% of the events. Overall, about 21% of the events passing the hadron filter pass the quality filter cuts, corresponding to 21061 events. The entire event selection procedure through the quality filter is shown in the flowchart of Fig. 3.4.

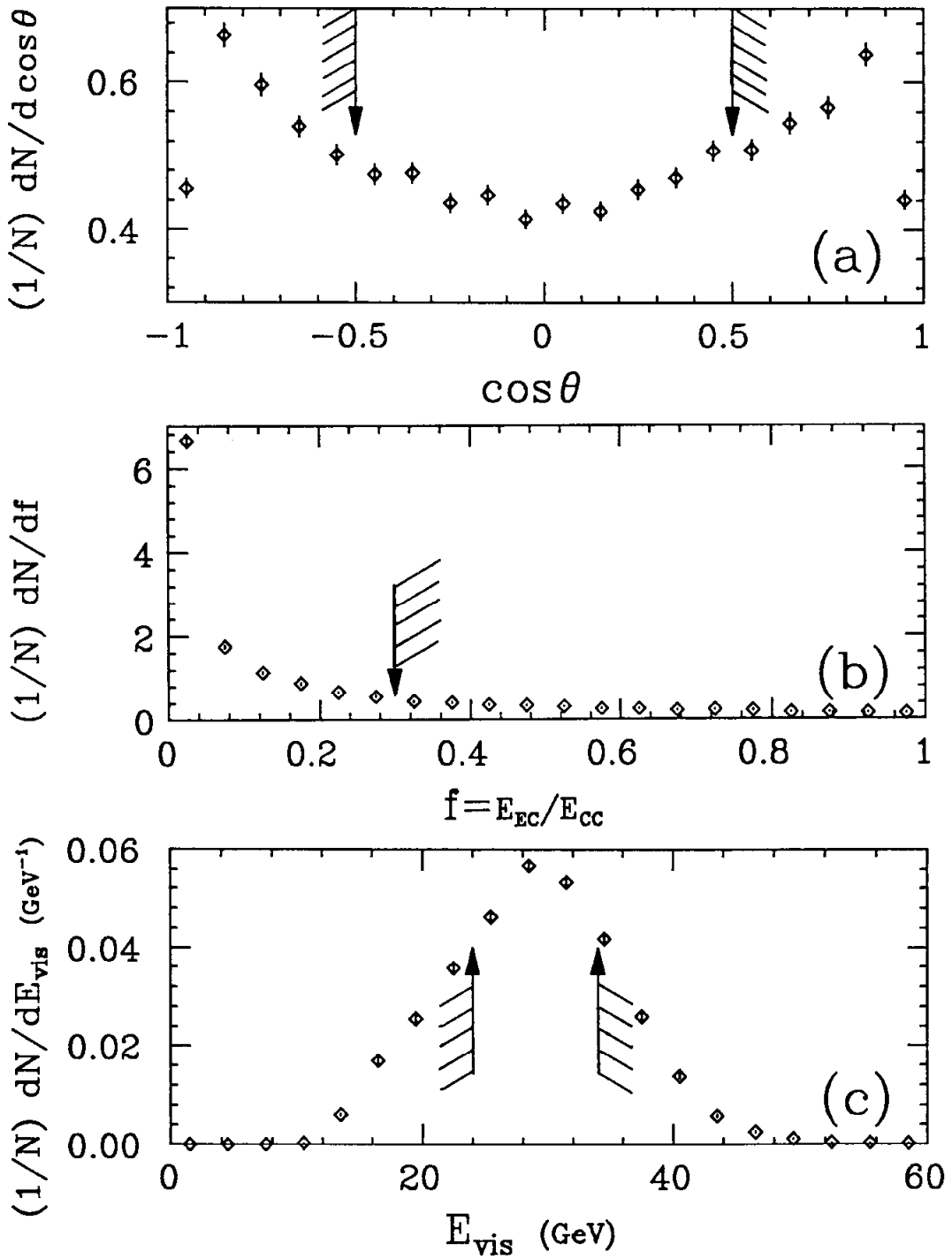

Figure 3.3. Location of cuts in the quality filter as shown for the data: (a) θ_{thrust} determined with calorimetry; (b) end-cap energy divided by central-section energy; (c) total calorimeter energy. These cuts orient the event plane to lie approximately transverse to the beam, and ensure that almost all of the event energy is deposited in the central calorimeters. The energy flow of these events is minimally distorted by the detector.

Table 3.3. Quality filter cuts: correlations.

Number of original 100475 events passing further cuts
(% passing cuts)

	θ_{thrust}	E_{EC}/E_{CC}	E_{vis}
θ_{thrust}	45649 (45%)	43334 (43%)	24776 (25%)
E_{EC}/E_{CC}		55842 (56%)	31777 (32%)
E_{vis}			51752 (52%)

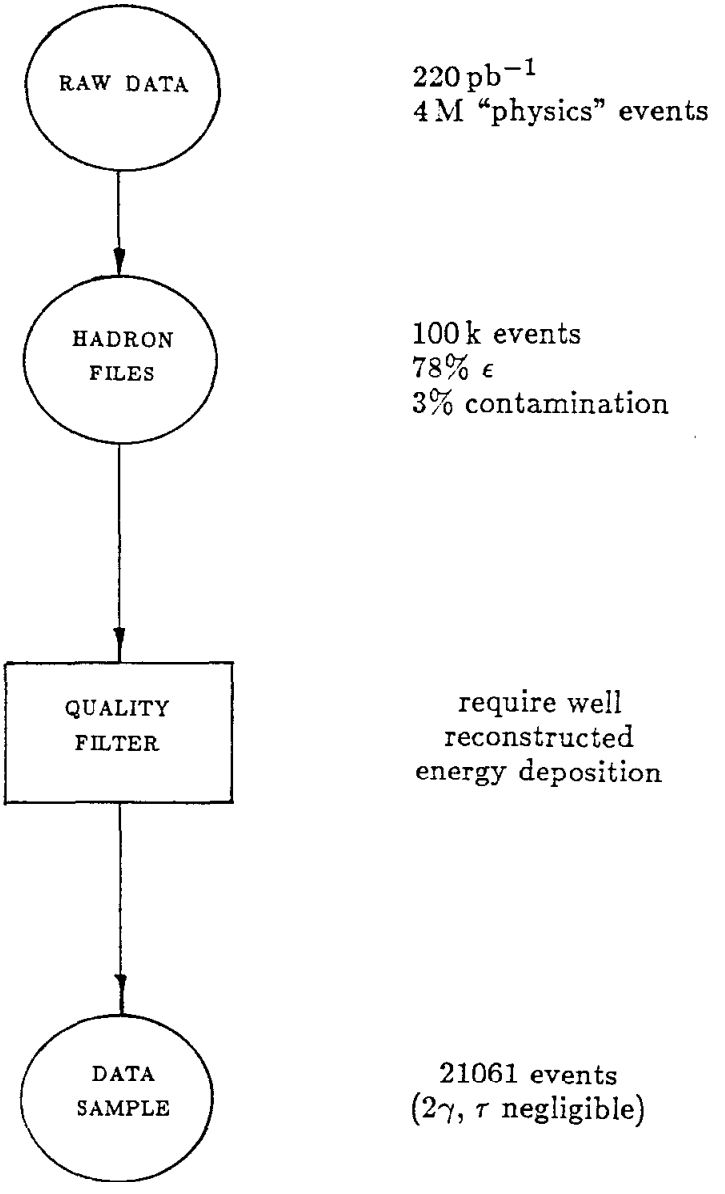

Figure 3.4. Flowchart of the event selection through the quality filter. The data sample of several million "physics" events (mostly Bhabha events) contains about 100 k multihadron events which the hadron filter selects. This sample is reduced to 21061 events by the quality filter. The energy flows of the surviving events are likely to be well reconstructed by the MAC calorimetry.

4. Measuring α_s

With the exception of R and 2γ methods, the measurements of α_s at PEP and PETRA follow a similar pattern. This pattern is delineated in Fig. 4.1 and is divided into two stages; (1) generation of Monte Carlo predictions for some particular measurable quantity "X"; and (2) a fitting procedure that varies the modeling parameters, which includes α_s, in order to give good agreement between the predicted and measured "X". The various PEP and PETRA measurements differ only in the choice of the quantity "X" The ideal "X" should have the following properties:

- high sensitivity to variations in α_s;
- low sensitivity to the IR cuts used in the QCD matrix elements; and
- low sensitivity to the soft fragmentation parameters.

4.1 The Sensitivity of $hE_{\perp}^{in}(\text{fat})$ to Fragmentation Parameters

We wish to use $hE_{\perp}^{in}(\text{fat})$, defined by

$$hE_{\perp}^{in}(\text{fat}) = \max\left\{hE_{\perp}^{in}\binom{one}{side}, hE_{\perp}^{in}\binom{other}{side}\right\} \quad ,$$

as the quantity "X". We expect that gluon emission will manifest itself in fragmentation with larger jet $E_{\perp}$. So, the fatter side of a hadronic event should be associated with this harder perturbative QCD process. In addition, by projecting the event energy into the event plane, the contribution of single gluon emission is enhanced relative to higher order multiple gluon emission. This decreases uncertainties coming from higher order QCD contributions. We therefore embark on a campaign of determining how closely $hE_{\perp}^{in}(\text{fat})$ approaches the ideal "X".

4.1.1 Sensitivity to α_s

As expected, $hE_{\perp}^{in}(\text{fat})$ is sensitive to variations in α_s. This sensitivity is shown in Fig. 4.2 for Monte Carlo events satisfying the quality filter at α_s of 0.0, 0.1 and

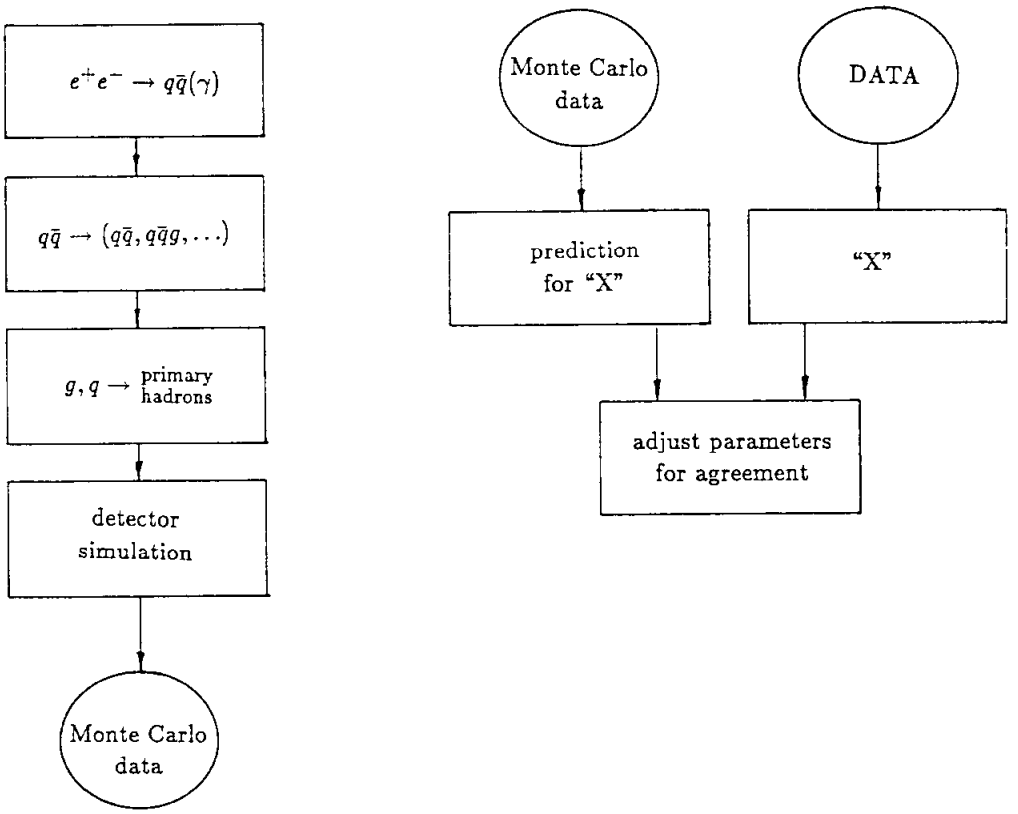

Figure 4.1. The generic measurement of α_s by PEP and PETRA experiments using shape, cluster and energy-energy correlation methods. The quantity "X" is a set of measurable quantities that are fit to the data by adjusting the modeling parameters. The quantity "X" should be sensitive to α_s, and much less sensitive to the remaining fragmentation parameters.

0.2, where the String model was used for the fragmentation. Observe that the bin contents in the tail of the distribution are approximately proportional to α_s.

4.1.2 *Sensitivity to σ_q*

We expect the transverse energy structure of hadronic events to also show sensitivity to σ_q, the width of the secondary quark $P_\perp$ distribution relative to the primary parton direction for the IJM model, or to the axis of the string in the string rest frame, in the case of the STR model. This sensitivity of $hE_\perp^{in}(\text{fat})$ to σ_q is shown in Fig. 4.3 for the rather extreme range of $\sqrt{2}\sigma_q$ represented by 300, 440 and 600 MeV/c, using the String fragmentation hypothesis. This sensitivity, though not as great as seen by varying α_s, is still non-negligible, even out to the extreme tail of the distribution.

4.1.3 *Sensitivity to Remaining Parameters*

The remaining fragmentation parameters have substantially less effect on the $hE_\perp^{in}(\text{fat})$ distribution, especially in the tail. These other fragmentation parameters are discussed in decreasing order of sensitivity.

The IR cut used in the QCD matrix elements has a slight effect on the $hE_\perp^{in}(\text{fat})$ distribution. The IR cut used is an invariant mass cut between any two partons in the event. Specifically, the IR cut requires $Y_{ij} > Y_{min}$, where $Y_{ij} = M_{ij}^2/s$ is the square of the scaled invariant mass between partons i and j. As Y_{min} increases, the number of *3* and *4-jet* events decrease, though the hard wide angle radiative component is largely unaffected. This tends to decrease the population in the tail of the normalized $hE_\perp^{in}(\text{fat})/E_{vis}$ distribution. In practice, Y_{min} is set small enough so that its exact value is experimentally unresolvable. The lower limit of allowed Y_{min} values is reached when it results in unphysical values for the QCD matrix elements. A more complete discussion of the role of the IR cut may be found in Appendix A. The sensitivity of $hE_\perp^{in}(\text{fat})$ to the QCD IR cut is show in Fig. 4.4. It should be noted that $hE_\perp^{in}(\text{fat})$ is only weakly sensitive to Y_{min}, with the sensitivity falling off towards the tail of the distribution; the crossover point being somewhere before $hE_\perp^{in}(\text{fat})/E_{vis} = 0.2$.

The shape of the fragmentation functions used has a slight effect on the population in the tail of the $hE_\perp^{in}(\text{fat})$ distribution. As an example of this dependence, we show in Fig. 4.5 the effect of changing the peak of the Peterson form of the charmed quark fragmentation function, Z_c^{max}, from 0.4 to 0.8. From looking

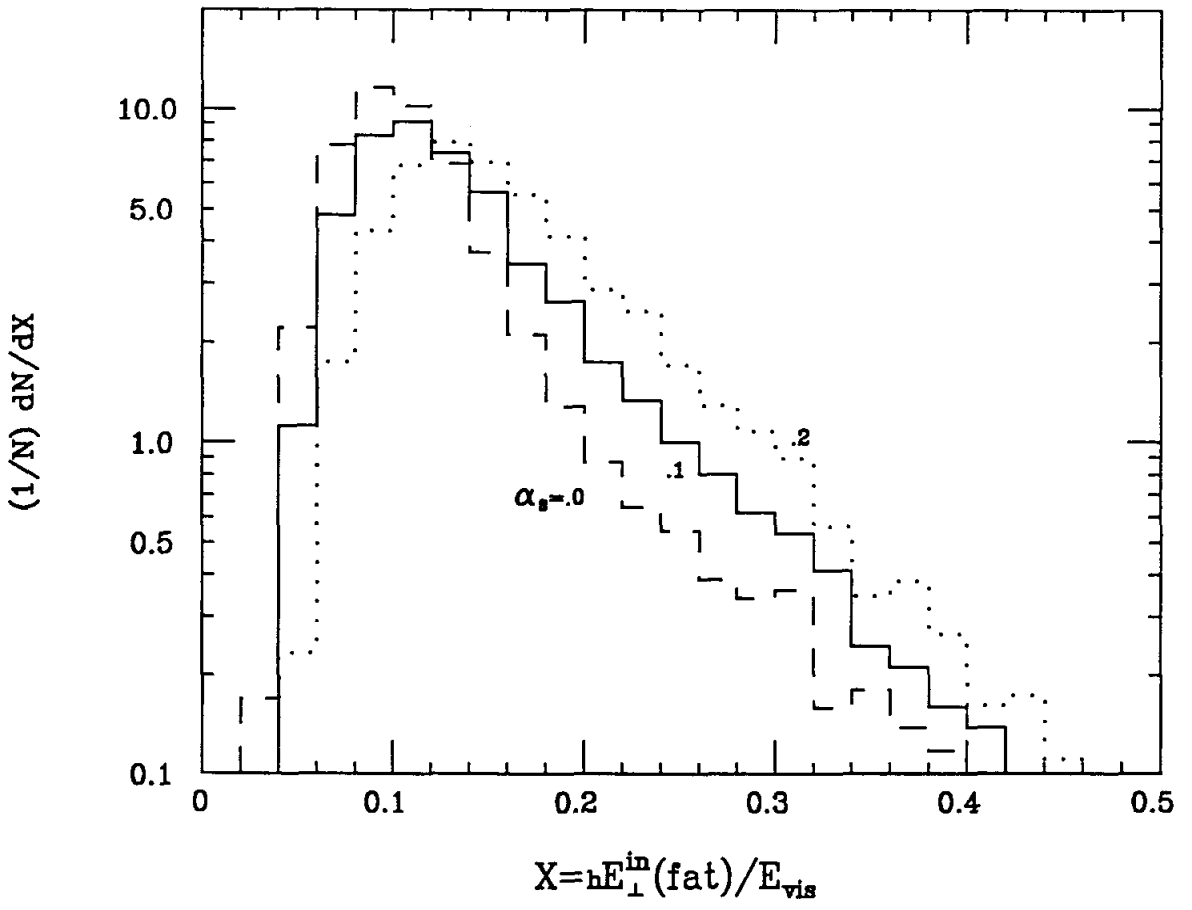

Figure 4.2. Sensitivity of $hE_{\perp}^{in}$(fat) to variations in α_s. The two curves shown are for a String model using α_s of 0.0, 0.1 and 0.2. The population in the tail is proportional to α_s. The sensitivity of $hE_{\perp}^{in}$(fat) to α_s is much greater than to the other fragmentation parameters.

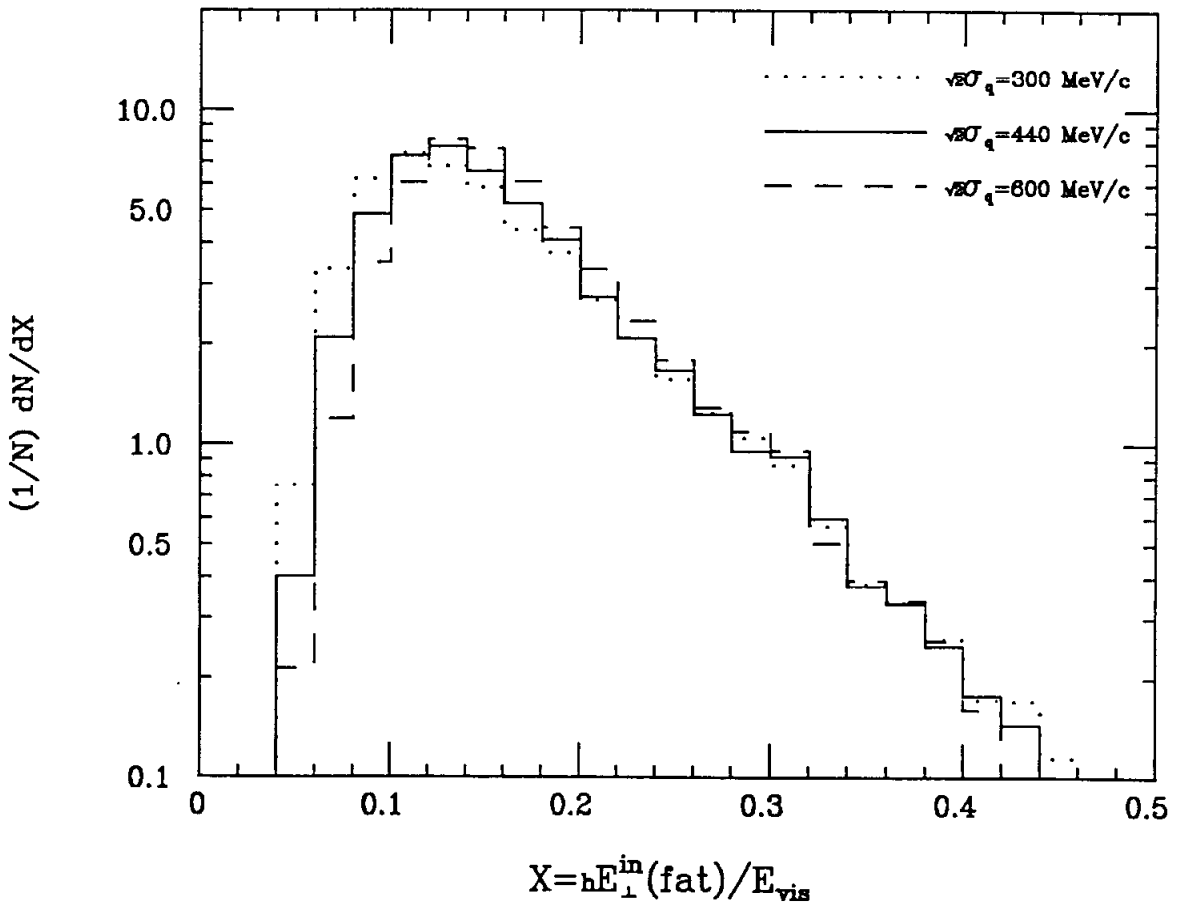

Figure 4.3. Sensitivity of $hE_{\perp}^{in}(\text{fat})$ to variations in σ_q. The three curves shown are for a String model using the rather wide range of $\sqrt{2}\sigma_q$ values represented by 300, 440 and 600 MeV/c. There is a slight sensitivity out to the tail of the distribution. This sensitivity, though considerably less than that from α_s, requires that σ_q be fit simultaneously with α_s. The remaining fragmentation parameters have a much smaller effect on the $hE_{\perp}^{in}(\text{fat})$ distribution.

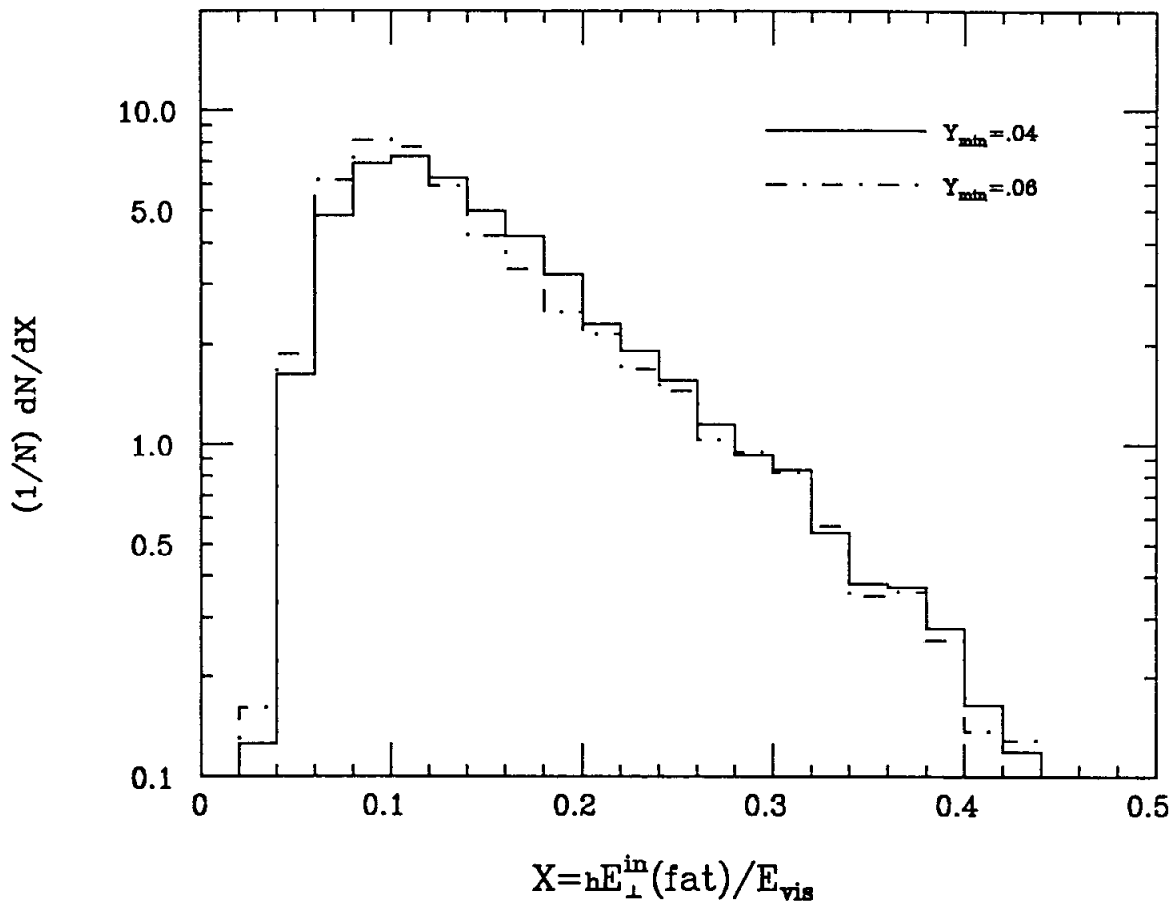

Figure 4.4. Lack of sensitivity of $hE_{\perp}^{in}$(fat) to variations in Y_{min}. The two curves shown are for a String model using two widely separated values of Y_{min} of 0.04 and 0.06. The shape of the distribution is not sensitive to he precise placement of the IR cutoff in the QCD matrix elements.

at Fig. 4.6, which shows the maximum Z value of the Peterson $D(Z)$ distribution as a function of ϵ, the values Z_c^{max} of .4 and .8 correspond to an ϵ_c range of .9 to .05. This represents an extreme range of values for the charmed quark fragmentation function,[32] yet the effect on the $hE_\perp^{in}(\text{fat})$ distribution is only slight and is restricted to the tail of the $hE_\perp^{in}(\text{fat})$ distribution. The experimental uncertainty in the bottom quark fragmentation function is greater, though the suppression of bottom quarks by a factor of four relative to charmed quarks makes the smaller uncertainty in the charmed quark fragmentation more significant. The uncertainty in the a parameter of the Field and Feynman fragmentation functions for the lighter quarks is considerably less.[33]

Other parameters of the soft fragmentation were varied in a similar manner in order to determine their effect on the $hE_\perp^{in}(\text{fat})$ distribution. Only two of these parameters appeared to have even a slight effect on the $hE_\perp^{in}(\text{fat})$ distribution. These two parameters are $P/(P+V)$, the fraction of pseudoscalar to vector mesons produced in the fragmentation, and $P(qq)/P(q)$, the ratio of diquark pairs to quark pairs produced in the fragmentation (this regulates baryon production in these models). The remaining parameters had no statistically significant effect on the $hE_\perp^{in}(\text{fat})$ distribution.

4.1.4 Summary of Sensitivities

We summarize here the results of our program of determining the sensitivity of $hE_\perp^{in}(\text{fat})$ to the various fragmentation parameters:

- Very sensitive to α_s;
- Sensitive to σ_q, sensitivity diminishing in the tail region;
- Very weak sensitivity, especially in the tail region, to Y_{min} and $D(Z)$;
- Barely discernable sensitivity to $P/(P+V)$ and $P(qq)/P(q)$; and
- No sensitivity to a host of remaining parameters.

4.2 The Fit Procedure

Consideration of the previous section reveals the following points:

- $hE_\perp^{in}(\text{fat})$ is insensitive to most fragmentation parameters in the tail of the distribution; and
- Since $hE_\perp^{in}(\text{fat})$ retains some sensitivity to σ_q, even in the tail of the distribution, α_s and σ_q must be fit simultaneously.

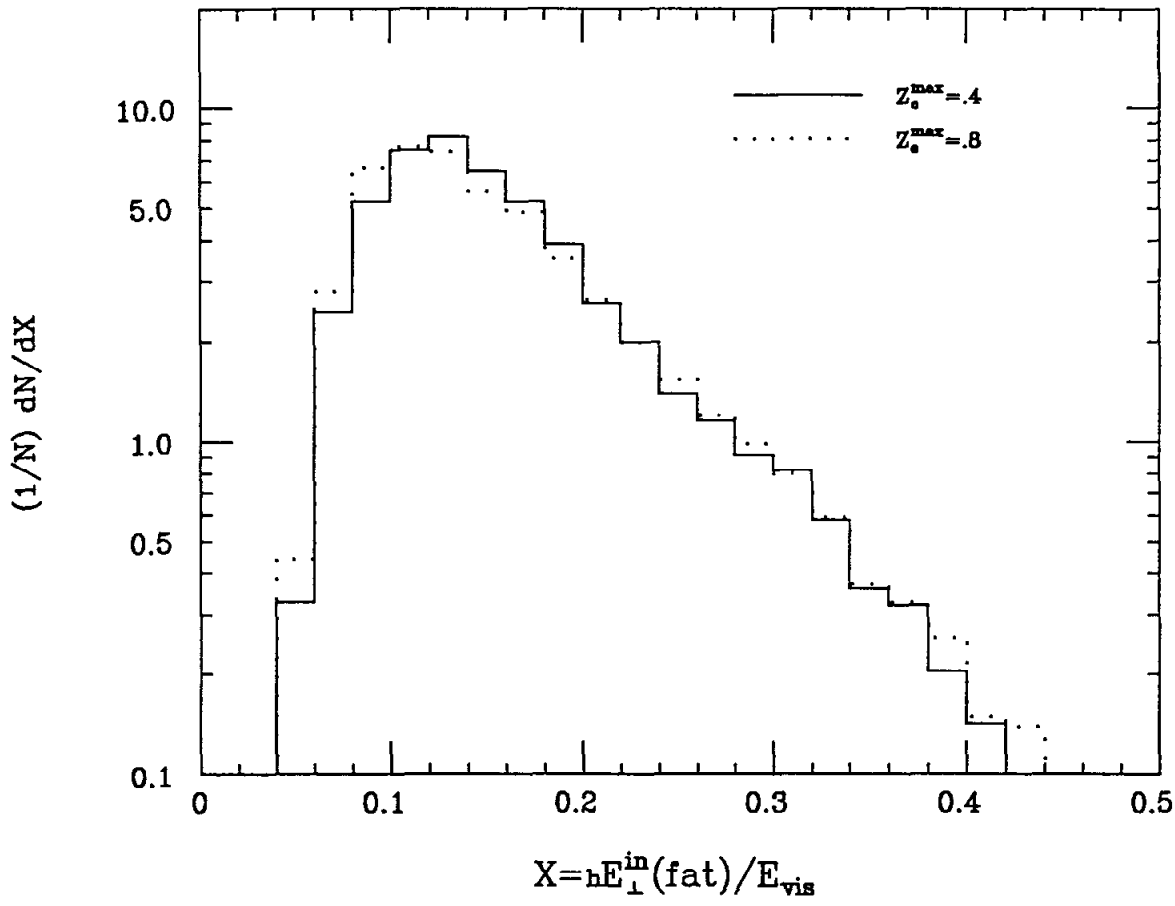

Figure 4.5. Lack of sensitivity of $hE_{\perp}^{in}(\text{fat})$ to variations in Z_c^{max}, the peak of the charmed quark fragmentation function. The two curves shown use the Peterson form for the charmed quark fragmentation function with two extreme Z_c^{max} values of .4 and .8. The shape of the light quark fragmentation functions are much more well measured. The shape of the b quark fragmentation function is poorly known, but the rate of b production is small.

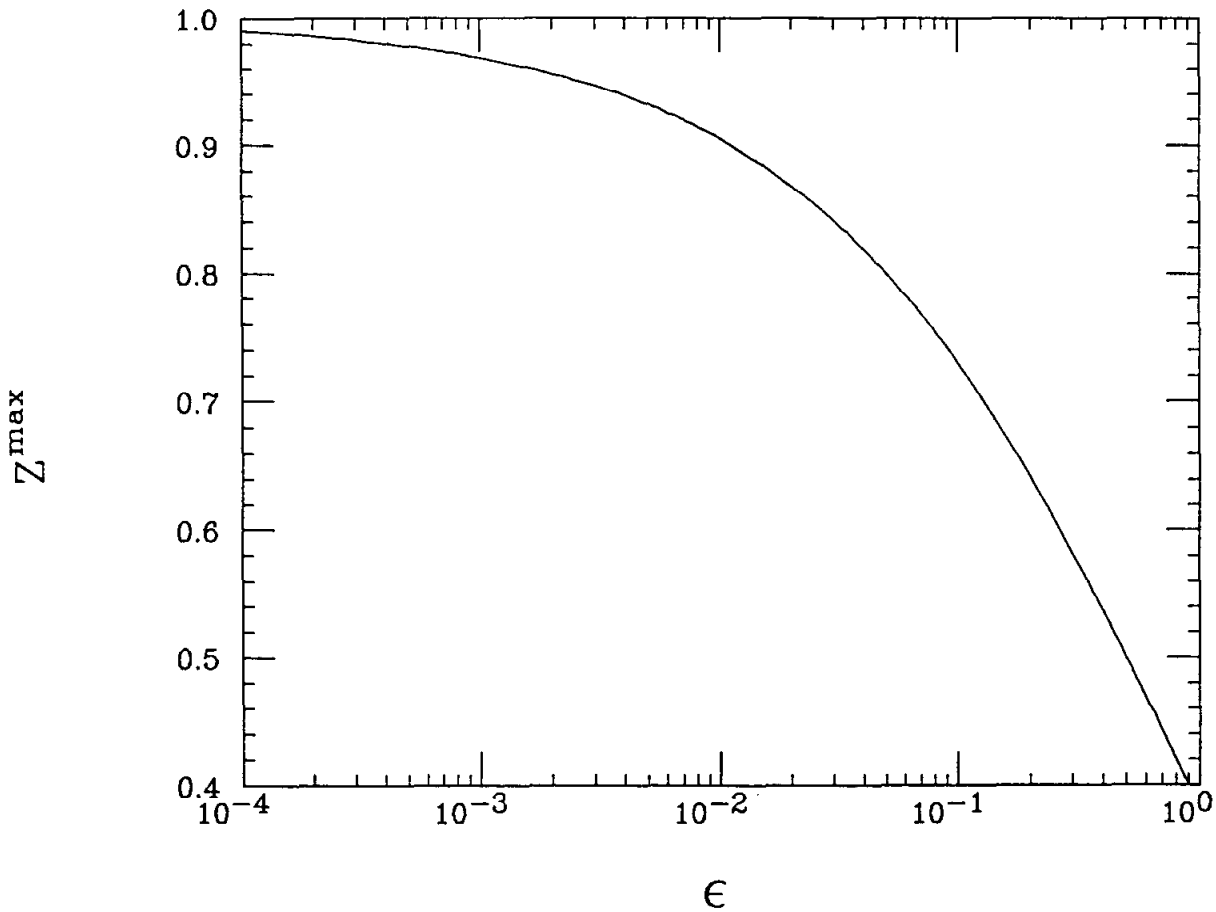

Figure 4.6. Peak of the Peterson fragmentation function, Z^{max}, as a function of ϵ. Most studies of heavy quark fragmentation functions quote a value of ϵ.

The fit procedure is comprised of two parts; constructing an analytic expression representing the bin contents of $hE_{\perp}^{in}(\text{fat})$, as a function of α_s and σ_q, and the varying α_s and σ_q so as to obtain good agreement between the data and the analytic expression.

4.2.1 *Construction of the Analytic Form of* $hE_{\perp}^{in}(\text{fat})$

The objective here is to construct an analytic expression for the contents of the i^{th} bin of $hE_{\perp}^{in}(\text{fat})$ as a function of α_s and σ_q. Ideally, at each value of α_s and σ_q required in the fitting procedure, a complete Monte Carlo prediction of $hE_{\perp}^{in}(\text{fat})$ should be made. However, these Monte Carlo predictions are computer intensive, taking about 5 sec/event, making a direct approach unfeasible.

To avoid this problem, the bin contents of $hE_{\perp}^{in}(\text{fat})$ are estimated via a lattice approximation. In this approximation, we generate 16 Monte Carlo predictions *e.g.*,

		α_s			
		.08	.10	.12	.14
$\sqrt{2}\sigma_q$ (GeV/c)	300	•	•	•	•
	370	•	•	•	•
	440	•	•	•	•
	510	•	•	•	•

with each • indicating a Monte Carlo prediction using the corresponding value of α_s and σ_q. These 16 predictions are fit to an analytic expression of the form

$$N^k(\sigma_q, \alpha_s) = \sum_{i=0}^{2} \sum_{j=0}^{2-i} a_{ij} \sigma_q^i \alpha_s^j \quad ,$$

where $N^k(\alpha_s, \sigma_q)$ is the predicted contents of the k^{th} bin of $hE_{\perp}^{in}(\text{fat})$ as a function of α_s and σ_q. Subsequent fits show the $i = 2$ and $j = 2$ terms to be small.

4.2.2 *Fit* $N^k(\alpha_s, \sigma_q)$ *to* $hE_{\perp}^{in}(\text{fat})$

The previous section discussed the construction of $N^k(\alpha_s, \sigma_q)$, the predicted contents of the k^{th} bin of $hE_{\perp}^{in}(\text{fat})$ as a function of α_s and σ_q. Here, we precede to fit $N^k(\alpha_s, \sigma_q)$ to $hE_{\perp}^{in}(\text{fat})$.

We have previously observed that the tail of the $hE_{\perp}^{in}(\text{fat})$ distribution is less sensitive to variations of the fragmentation parameters. We thus fit bins of

Table 4.1. Best fit α_s and σ_q in the tail of the $hE_{\perp}^{in}$(fat) distribution for STR and IJM fragmentation. The χ^2 values shown have 18 DOF. The IJM models consider gluon fragmentation where $g \rightarrow q$ or $g \rightarrow q\bar{q}$, and energy-momentum conservation according to the Ali or Hoyer schemes, and a case ("No E-P") where there is no energy-momentum conservation imposed.

energy-momentum conservation scheme	α_s	σ_q (MeV/c)	χ^2	gluon fragmentation scheme
String	$.167 \pm .006$	299 ± 33	13.4	
Ali	$.128 \pm .007$	225 ± 27	12.2	
Hoyer	$.109 \pm .007$	217 ± 44	13.2	$g \rightarrow q$
No E-P	$.141 \pm .005$	207 ± 23	13.0	
Ali	$.125 \pm .009$	260 ± 35	10.8	
Hoyer	$.109 \pm .004$	208 ± 23	8.9	$g \rightarrow q\bar{q}$
No E-P	$.153 \pm .007$	225 ± 19	17.3	

$X(\text{fat}) = hE_{\perp}^{in}(\text{fat})/E_{vis}$ for $X(\text{fat}) \geq 0.2$. These remaining bins (18) are used in a χ^2 fitting procedure.

The final step is to use the values of α_s and σ_q resulting from the fit procedure as input values for a full Monte Carlo simulation of $hE_{\perp}^{in}$(fat). This is then compared with the data in order to verify that the fitting procedure gives correct results.

4.3 Results of the Fit

The α_s, σ_q and minimal χ^2 values for the fit to the tail of the $hE_{\perp}^{in}$(fat) are given in Table 4.1 for STR and IJM fragmentation. The IJM models consider gluon fragmentation where $g \rightarrow q$ or $g \rightarrow q\bar{q}$, and energy-momentum conservation according to the Ali or Hoyer schemes, and a case ("No E-P") where there is no energy-momentum conservation imposed. A total of 18 bins were used in the fit. These fitted values of σ_q are consistent with the width of hadronic $P_{\perp}$ distributions reported from SPEAR[34] and DORIS[35] experiments.

As a check of the fitting procedure, the best-fit values of α_s and σ_q from Table 4.1 were used as input parameters for a full Monte Carlo simulation of $hE_{\perp}^{in}$(fat) for comparison with the data. In Fig. 4.7, is shown a Monte Carlo simulation using the best-fit String values of α_s and σ_q from Table 4.1. Selected

statistical error bars for the Monte Carlo are included on the figure. The fits using the quadratic analytic expression $N^k(\alpha_s, \sigma_q)$ and the full Monte Carlo simulation both provide good fits to the data.

The α_s, σ_q and minimal χ^2 values for the fit to all the bins of $hE_\perp^{in}(\text{fat})$ are given in Table 4.2 for STR and IJM fragmentation. A total of 26 bins were used in the fit. The entire distribution is more sensitive to a host of other fragmentation parameters besides α_s and σ_q; no attempt has been made to adjust these other parameters around their nominal values. We consider the fits to just the tail of the $hE_\perp^{in}(\text{fat})$ distribution less prone to systematic errors from the other fragmentation parameters and are the primary results of this chapter; these resulting values of α_s and σ_q are examined in more detail in the following sections.

4.4 Correlations Between α_s and σ_q

In this sort of analysis, where we are fitting α_s using the transverse energy structure of jets, we must carefully examine the role of σ_q. Both α_s and σ_q contribute to the broadening of the fat jet, so the effect of a large σ_q is to mimic a small α_s. Since the tail of $hE_\perp^{in}(\text{fat})$ is less sensitive to variations in σ_q than in α_s, the range of σ_q over which there can be a reasonable fit is quite large. If α_s and σ_q are correlated, then there might be a common value of α_s, and very different values of σ_q, that nonetheless give reasonable fits to the data for an IJM and STR model. We wish to ensure that the difference in α_s from fits using different fragmentation models isn't an artifact coming from the particular values of the fragmentation parameters used in the fit.

This concern is checked in Fig. 4.8, which shows the $\Delta\chi^2 = 1$ (inner curves) and $\Delta\chi^2 = 2$ contours (outer curves) for the fits of α_s and σ_q to the data for IJM ($g \to q$, energy-momentum with the Ali scheme) and STR fragmentation from a fit to the tail of the $hE_\perp^{in}(\text{fat})$ distribution. An obvious feature of this figure is a correlation between α_s and σ_q. Contours for the other IJM fragmentation schemes show a similar qualitative behavior. The STR model tends to show less correlation. This is probably due to the slightly different role that σ_q takes in the two models. In IJM fragmentation, σ_q is the width of the $P_\perp$ spectrum of the secondary quarks relative to the primary parton direction. In STR fragmentation, σ_q is again the width of the $P_\perp$ spectrum of the secondary quarks, but here relative to the string direction. In general, the string is boosted with respect to the lab, and this distinction serves to decouple the STR σ_q from the STR α_s. It's important to note, however, that these

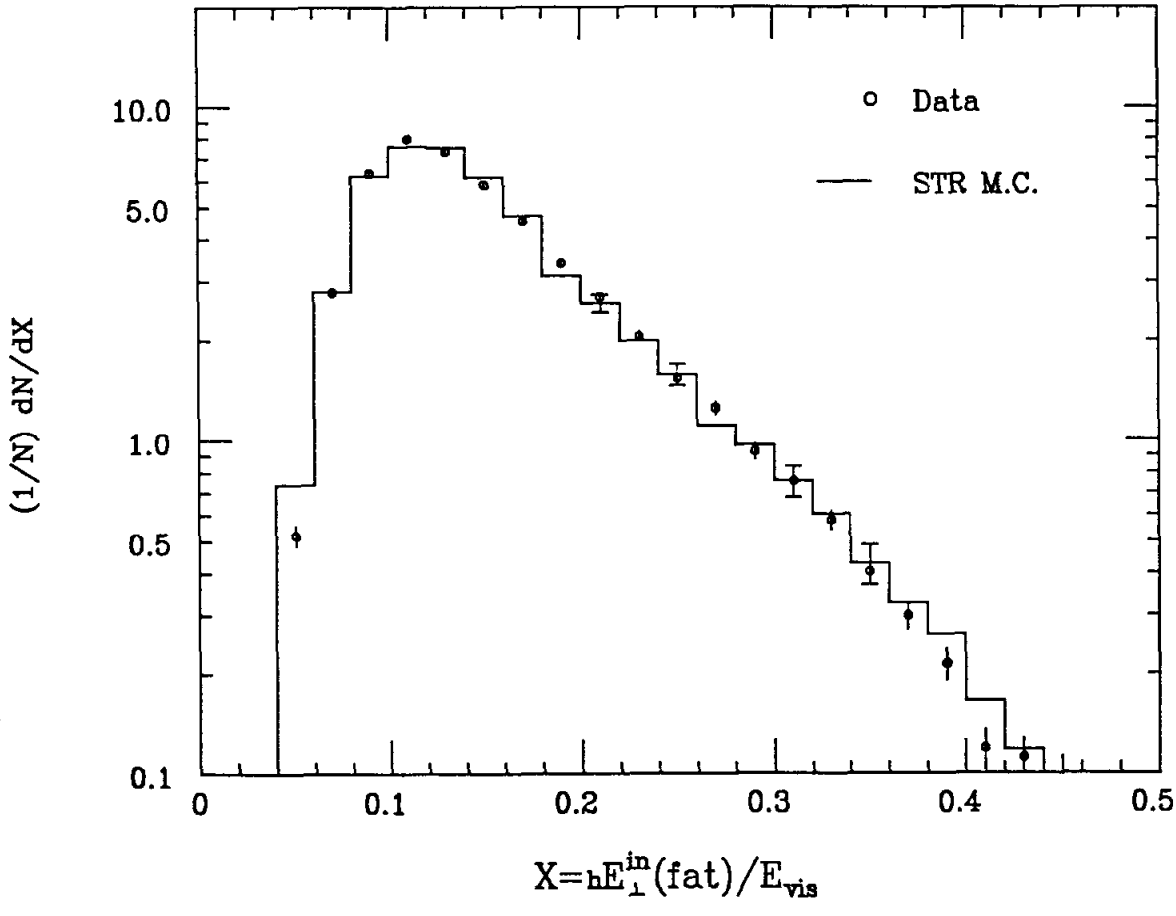

Figure 4.7. The String Monte Carlo compared to the data. This Monte Carlo simulation uses the best-fit String values of α_s and σ_q of Table 4.1. The region $X(\text{fat}) > 0.2$ was used in the fit. Selected statistical error bars for the Monte Carlo are included on the Monte Carlo curve. The low $X(\text{fat})$ region we determined to be more sensitive to the unfitted fragmentation parameters. The good fit in the tail of the distribution confirms the correctness of the fitting procedure.

Table 4.2. Fit of α_s and σ_q over all bins of $hE_{\perp}^{in}$(fat) for STR and IJM fragmentation. The χ^2 values shown have 26 DOF. The IJM models consider gluon fragmentation where $g \rightarrow q$ or $g \rightarrow q\bar{q}$, energy-momentum conservation according to the Ali or Hoyer schemes, and a case (no E-P) where there is no energy-momentum conservation imposed. These fitted values are sensitive to fragmentation parameters other than α_s and σ_q.

energy-momentum conservation scheme	α_s	σ_q (MeV/c)	χ^2	gluon fragmentation scheme
String	$.163 \pm .003$	283 ± 7	25.2	
Ali	$.118 \pm .005$	278 ± 11	47.1	
Hoyer	$.090 \pm .003$	335 ± 7	129.4	$g \rightarrow q$
No E-P	$.120 \pm .003$	292 ± 5	98.0	
Ali	$.113 \pm .005$	309 ± 4	36.8	
Hoyer	$.089 \pm .003$	346 ± 7	114.5	$g \rightarrow q\bar{q}$
No E-P	$.122 \pm .003$	300 ± 6	77.2	

correlations aren't sufficient to allow any overlap between the IJM and STR models in (α_s, σ_q) space. There is no combination of parameters allowing reasonable fits to the data with STR and IJM fragmentation models using the same value of α_s.

4.5 Conclusions

We now compare the various α_s values resulting from this study with each other, and with α_s values reported by other collaborations.

4.5.1 Comparisons of α_s Values From This Analysis

We observe several inter-relationships among the α_s values reported in Table 4.1. Most striking is the observation that the α_s value resulting from using the String hypothesis is larger than the α_s values resulting from the various IJM hypotheses. The fractional difference between STR and IJM models, $[\alpha_s(STR) - \alpha_s(IJM)]/\alpha_s(STR)$, is given in Table 4.3 for the various IJM fragmentation schemes considered. Note that invoking energy-momentum considerably increases the fraction $[\alpha_s(STR) - \alpha_s(IJM)]/\alpha_s(STR)$, to about 30% for the Ali, and about 50% for the Hoyer energy-momentum conservation schemes. The values of α_s

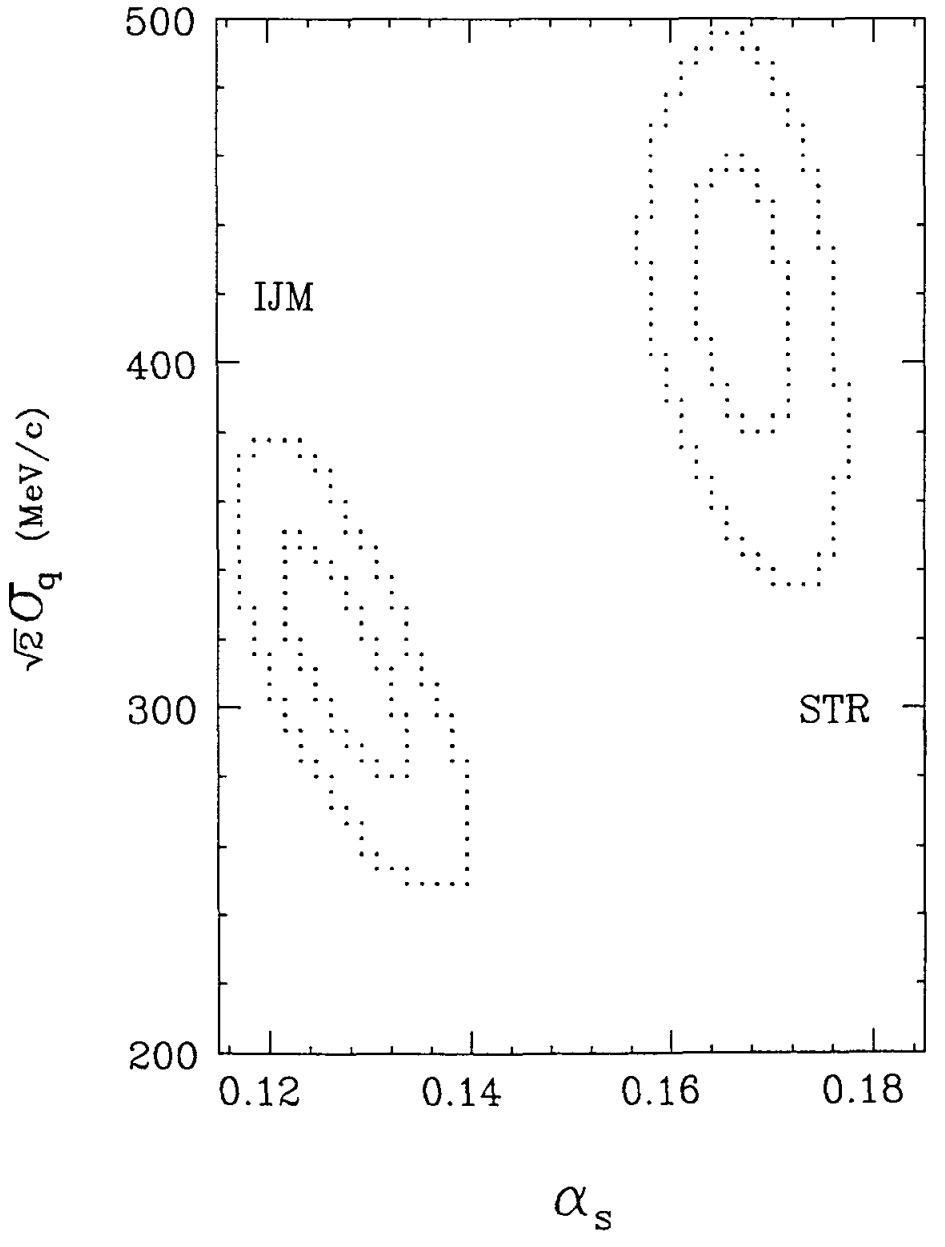

Figure 4.8. $\Delta\chi^2 = 1$ and $\Delta\chi^2 = 2$ contours in α_s and σ_q fits using IJM ($g \rightarrow q$, energy-momentum with the Ali scheme) and STR fragmentation. There are no values of fragmentation parameters that will allow the IJM and STR models to share a common value of α_s and still provide reasonable fits to the data.

Table 4.3. $[\alpha_s(STR) - \alpha_s(IJM)]/\alpha_s(STR)$ for the range of IJM fragmentation schemes considered in Table 4.1. The STR model yields larger values of α_s than IJM fragmentation.

energy-momentum conservation scheme	$\frac{\alpha_s(STR)-\alpha_s(IJM)}{\alpha_s(STR)}$	gluon fragmentation scheme
Ali	30%	
Hoyer	53%	$g \rightarrow q$
No E-P	18%	
Ali	34%	
Hoyer	53%	$g \rightarrow q\bar{q}$
No E-P	9%	

resulting from IJM fragmentation without invoking energy-momentum conservation are only slightly reduced from the STR α_s. This behavior is typical of any energy-momentum conservation scheme applied to IJM fragmentation. A more complete discussion of this point may be found in Appendix A.

This analysis shows no statistically significant difference between the α_s values fitted using IJM fragmentation with $g \rightarrow q$ and the α_s values fitted using IJM fragmentation with $g \rightarrow q\bar{q}$, where both cases incorporate either the Ali or Hoyer schemes for energy-momentum conservation. IJM fragmentation without invoking energy-momentum conservation gives slightly higher α_s values.

4.5.2 Comparisons With Previous MAC Results

There are two previous MAC measurements of α_s. One result uses the technique of fitting the energy-energy correlation asymmetry using the entire hadronic data sample. The other result determines α_s from a precision measurement of R. These previous measurements are shown in Fig. 4.9, where for the shape and energy-energy correlation asymmetry, only the α_s values fitted using the STR and IJM with $g \rightarrow q$ and energy-momentum conservation using the Ali scheme are shown. The R measurement α_s value shown uses the $\overline{MS}$ renormalization scheme. These other MAC results are detailed in the sections following.

4.5.2.1 Energy-Energy Correlation Asymmetry

The energy-energy correlation asymmetry method is based on a technique suggested by Basham, Brown, Ellis and Love (BBEL)[36]. The idea is as follows:

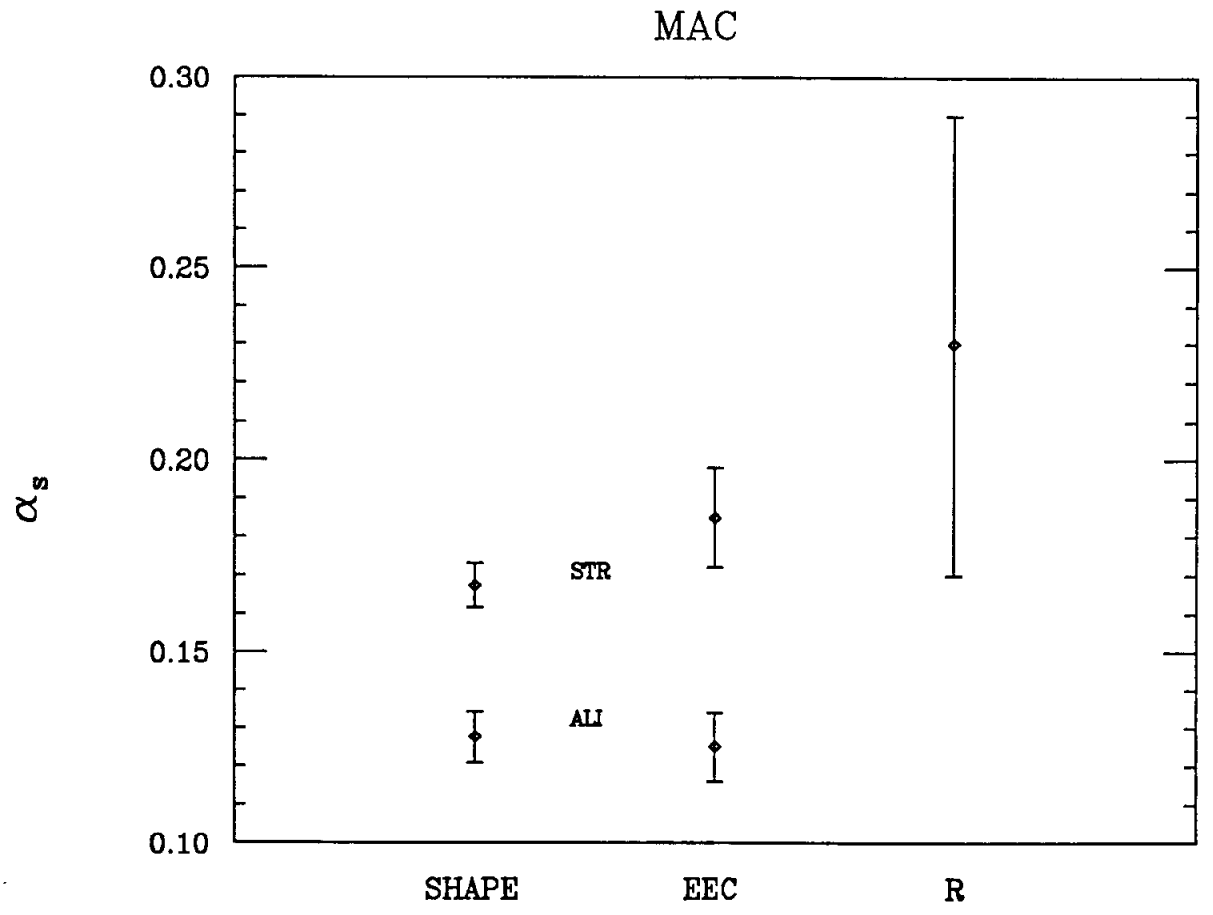

Figure 4.9. MAC α_s measurements using shape (present analysis) energy-energy correlation asymmetry and R. For the shape and energy-energy correlation asymmetry, the α_s values fitted using the STR and IJM with $g \rightarrow q$ and energy-momentum conservation using the Ali scheme are shown. The R measurement α_s value uses the $\overline{MS}$ renormalization scheme. The R measurement is only minimally affected by the systematic errors of the fragmentation models. The shape and energy-energy correlation measurements are model dependent and show qualitative agreement.

First, the energy-energy correlation cross section is measured using a finite angular resolution modification of the perfect resolution cross section

$$\frac{1}{\Sigma}\frac{d\Sigma}{d\cos\chi} = \frac{1}{N}\sum_{1}^{N}\sum_{ij}\frac{E_i E_j}{E_{vis}^2}\delta(\cos\chi_{ij} - \cos\chi) \quad ,$$

where N is the total number of hadronic events, and χ_{ij} is the angle between the i^{th} and j^{th} energy vector in any one event. Then, the energy-energy correlation asymmetry cross section is determined from

$$A(\cos\chi) = \frac{1}{\chi}\left\{\frac{d\Sigma}{d\cos\chi}(\pi - \chi) - \frac{d\Sigma}{d\cos\chi}(\chi)\right\} \quad .$$

The shape of the asymmetry cross section depends on α_s, and, in principle, very little on the nonperturbative parts of the hadronization.

We have followed the BBEL prescription for the MAC energy-energy correlation asymmetry measurement of α_s. The QCD matrix elements used $O(\alpha_s^2)$ calculations, and the asymmetry was corrected for detector effects and initial state QED radiation. The results of the fit[37] are given in Table 4.4. The values of α_s from the shape analysis are consistent with the α_s values from the earlier energy-energy correlation asymmetry analysis. The values for α_s fitted with the string hypothesis are almost 1σ apart, with the shape-derived α_s being smaller. The energy-energy correlation asymmetry determination of α_s also gives a bigger difference between the $g \to q$ and $g \to q\bar{q}$ modes of gluon fragmentation than the shape analysis does, though the effect is indeed slight.

4.5.2.2 R Measurement

MAC has recently reported on a precision measurement of R,[38] defined by the relation

$$R = \frac{\sigma(e^+e^- \to hadrons)}{\sigma(e^+e^- \to \mu^+\mu^-)} \quad .$$

The theoretical expression for R has a weak dependence on α_s, that depends on the renormalization scheme, given to $O(\alpha_s^2)$ by[39]

$$R = 3\sum_{i=1}^{n_f} e_q^2\left[1 + \frac{\alpha_s}{\pi} + R_2\left(\frac{\alpha_s}{\pi}\right)^2 + \ldots\right]$$

Table 4.4. MAC α_s values from the energy-energy correlation asymmetry. The results use $O(\alpha_s^2)$ QCD matrix elements, and are corrected for detector effects and initial state QED radiation.

energy-momentum conservation scheme	α_s	gluon fragmentation scheme
String	$.185 \pm .013$	
Ali	$.125 \pm .009$	$g \rightarrow q$
Hoyer	$.105 \pm .007$	
Ali	$.140 \pm .010$	$g \rightarrow q\bar{q}$
Hoyer	$.110 \pm .008$	

where $R_2 = 1.98 - 0.115 n_f$ in the $\overline{MS}$ renormalization scheme, and n_f is the number of quark flavors. The value of R measured by MAC is

$$R = 3.96 \pm .03(stat) \pm .09(syst) \quad .$$

Using n_f of 5, we get $\alpha_s = .23 \pm .07$, where the statistical and systematic errors are added in quadrature.

We interject here a comment regarding the choice of renormalization scheme when determining α_s. For two different renormalization schemes, MS and $\overline{MS}$, The R_2 factor in the expansion of R into powers of α_s/π is

$$R_2 = \begin{cases} 7.35 - 0.442 n_f & (MS) \\ 1.98 - 0.115 n_f & (\overline{MS}) \end{cases} \quad .$$

Using the MAC result for the value of R, given above, α_s is determined in second order to be

$$\alpha_s = \begin{cases} .19 \pm .05 & (MS) \\ .23 \pm .07 & (\overline{MS}) \end{cases} \quad .$$

We see that the value of the second order α_s derived from R measurements, and from any other method, strongly depends on the renormalization scheme used in the exact $O(\alpha_s^2)$ calculations. In the remaining discussion, we will use α_s calculated using $\overline{MS}$ renormalization. The $\overline{MS}$ scheme is the standard renormalization prescription used

for QCD calculations. This standardization allows comparisons to be made with other experiments. By construction, the second order QCD corrections computed using $\overline{MS}$ renormalization tend to be quite small. This feature probably motivates this rare display of cooperation, though there is no guarantee that the next order corrections aren't large. The QCD matrix elements used in the present analysis are calculated with the $\overline{MS}$ scheme.

We observe that the MAC R result using the $\overline{MS}$ scheme is consistent with the shape and energy-energy correlation asymmetry α_s values fitted with the STR hypothesis, but not with the various IJM hypotheses. The difference between $\alpha_s(R)$ and α_s(IJM) amounts to about 1/10 unit of R.

4.5.3 Comparisons with Similar PEP/PETRA Experiments

There have been a number of α_s measurements performed at PEP and PETRA utilizing shape, cluster and energy-energy correlation asymmetry methods. In addition, the JADE collaboration has also reported a precision measurement of R. As discussed above, the $O(\alpha_s^2)$ corrections to the QCD matrix elements can be quite large, we therefore compare MAC results only with other measurements using $O(\alpha_s^2)$ QCD matrix elements computed in the $\overline{MS}$ renormalization scheme.

Before detailing the other PEP and PETRA measurements of α_s, a caution is in order: There is no agreement on the values of the soft hadronization parameters to be used, and in general, the soft fragmentation parameters used by each collaboration in fitting α_s remain unstated in the literature. We have seen that it is possible for these parameters, especially σ_q, to have a substantial effect on the fitted value of α_s. In Fig. 4.10 are shown the PEP and PETRA values of α_s and σ_q fitted using the STR fragmentation hypothesis. The references for data in Fig. 4.10 are provided in a following table. Not all groups reporting α_s values also report the value of σ_q used. The trend shown in Fig. 4.10 is for the STR value of σ_q to be about 300 MeV/c or less, with a relatively large spread.

The various PEP and PETRA α_s measurements using shape, cluster, energy-energy correlation asymmetry and R are shown in Fig. 4.11. For the shape, cluster and energy-energy correlation asymmetry, only the α_s values fitted using the STR and IJM with $g \rightarrow q$ and energy-momentum conservation using the Ali scheme are shown. The R measurement α_s values use the $\overline{MS}$ renormalization scheme. The numerical values and references for the data points shown in Fig. 4.11 are given in Table 4.5

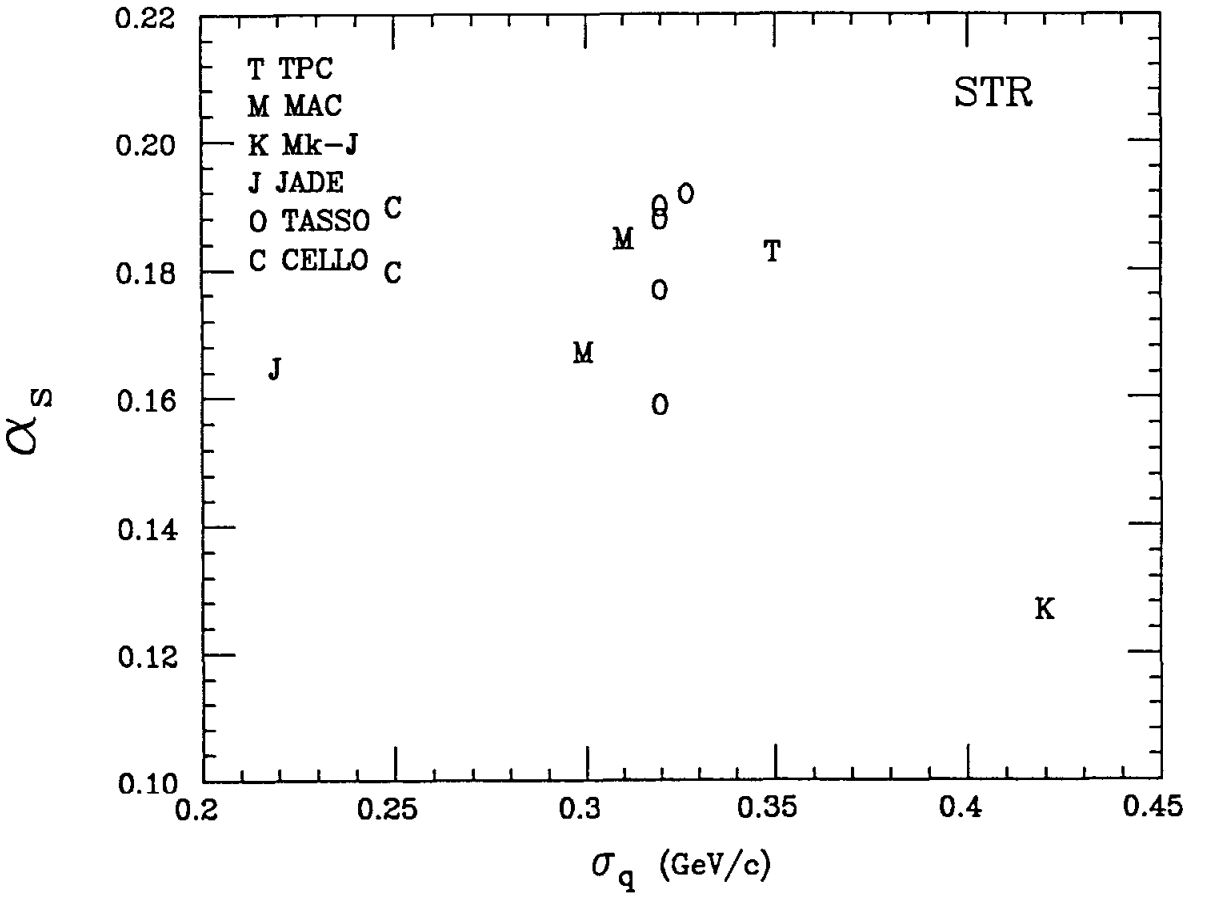

Figure 4.10. PEP and PETRA measurements of α_s and σ_q using the STR fragmentation hypothesis. There is no convergence among the various experimental on the values of fragmentation parameters to use. Not all groups reporting α_s values report simultaneous σ_q results. It is possible for the fitted values of σ_q and α_s to be correlated.

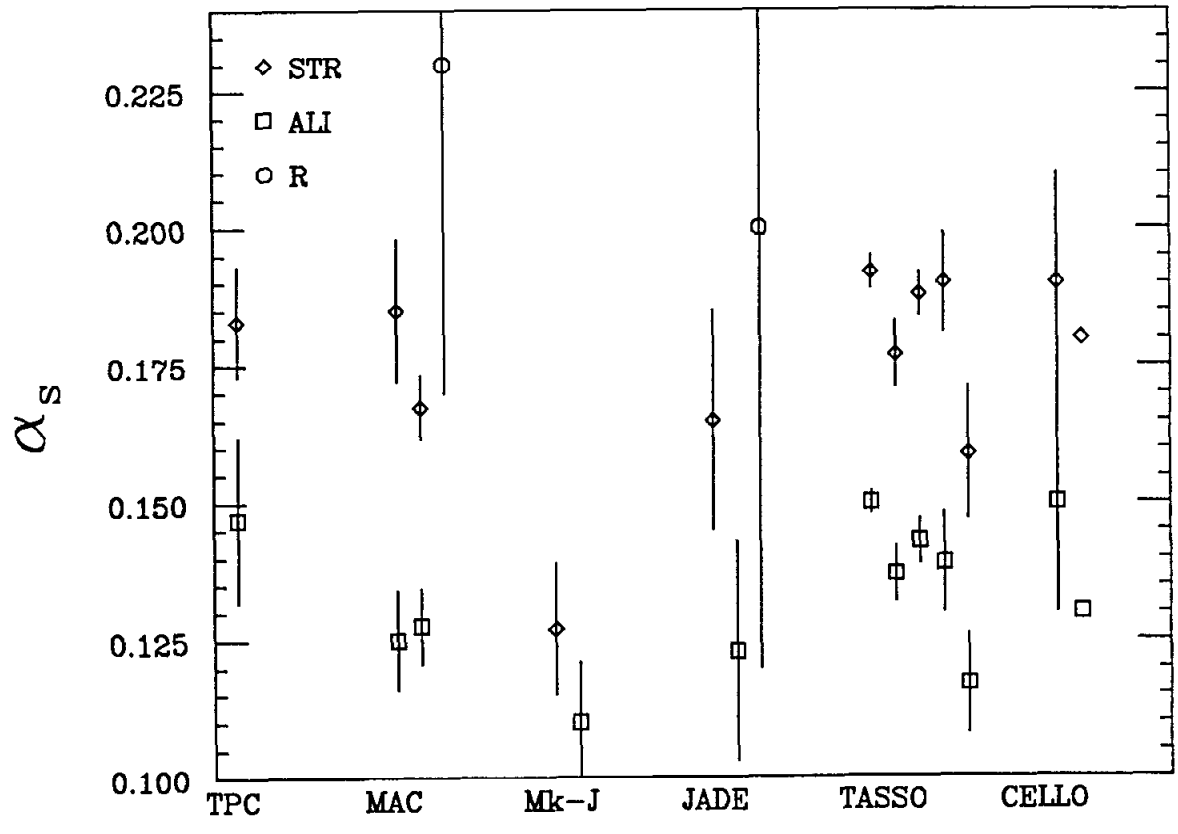

Figure 4.11. PEP and PETRA α_s measurements using shape, cluster, energy-energy correlation asymmetry and R. For the shape and energy-energy correlation asymmetry, only the α_s values fitted using the STR and IJM with $g \rightarrow q$ and energy-momentum conservation using the Ali scheme are shown. The R measurement α_s values use the $\overline{MS}$ renormalization scheme. The STR model produces larger values of α_s than the IJM models.

Table 4.5. PEP and PETRA α_s values, along with references, for shape, cluster, energy-energy correlation asymmetry and R studies. For the shape and energy-energy correlation asymmetry, only the α_s values fitted using the STR and IJM with $g \rightarrow q$ and energy-momentum conservation using the Ali scheme are shown. The R measurement α_s values use the $\overline{MS}$ renormalization scheme. The STR models yield larger α_s values than the IJM models.

collaboration	α_s STR	α_s IJM	method
TPC	$.183 \pm .010$	$.147 \pm .015$	shape[40]
MAC	$.185 \pm .013$	$.125 \pm .009$	eec[37]
	$.23 \pm .06$		R[38]
	$.167 \pm .006$	$.128 \pm .007$	shape[41]
Mk-J	$.127^{+.010}_{-.012}$	$.110^{+.008}_{-.011}$	eec[42]
JADE	$.165 \pm .02$	$.123 \pm .02$	eec[43]
	$.20 \pm .08$		R[44]
TASSO	$.192 \pm .003$	$.150 \pm .002$	shape[45]
	$.177 \pm .006$	$.137 \pm .005$	cluster[45]
	$.188 \pm .004$	$.143 \pm .004$	shape[45]
	$.190 \pm .009$	$.139 \pm .009$	eec[45]
	$.159 \pm .012$	$.117 \pm .009$	eec[45]
CELLO	$.19 \pm .02$	$.15 \pm .02$	eec[46]
	.18	.13	cluster[46]

With the exception of the Mk-J STR value of α_s, the MAC and the other PEP and PETRA shape, cluster and energy-energy correlation asymmetry results display overall agreement. For the STR and IJM model with $g \rightarrow q$ and energy-momentum according to the Ali scheme, the following trends emerge.

$$.16 \lesssim \alpha_s \lesssim .20 \qquad (STR)$$
$$.11 \lesssim \alpha_s \lesssim .15 \qquad (IJM) \quad .$$

The consensus here is for $\alpha_s(\text{STR}) > \alpha_s(\text{IJM})$ by factors of about 30%. The lone dissenter on this point is the Mk-J collaboration.

A short history of the Mk-J α_s measurements is in order. Their first second-order α_s measurement[47] entitled "Model-Independent Second-Order Determination of the Strong-Coupling Constant α_s", was published in 1983 and fitted α_s using the energy-energy correlation asymmetry cross section. Their reported value of α_s is

$$\alpha_s = \begin{cases} .14 \pm .01 & (\text{STR}) \\ .12 \pm .01 & (\text{IJM}) \end{cases} \quad .$$

Their second and most recent publication[42] also made use of the energy-energy correlation asymmetry. The α_s value reported is shown in Table 4.5. The quantity they are fitting to the data is an integral of the energy-energy correlation asymmetry cross section, I, given by

$$I = \int_{-.72}^{0} A(\cos\chi) d(\cos\chi) \quad .$$

Of interest is Fig. 2 in their most recent publication, which shows the integral I for Mk-J data points, along with curves of I for STR and IJM (Ali FORTRAN code) fragmentation models. Unfortunately, their data and Monte Carlo predictions are shown uncorrected for detector effects, making direct comparisons with other experiments difficult. We can, however, form the quantity

$$\Delta = \frac{I(Ali) - I(STR)}{I(Ali)} \quad ,$$

which is relatively insensitive to detector effects. We show in Fig. 4.12 the Mk-J values of Δ as computed from the values of I shown in Fig. 2 for a range of $\sqrt{s}$. The Monte Carlo curve for Δ was generated for the case of an ideal detector, and is, incidentally, the curve describing the magnitude of $\{\alpha_s(STR) - \alpha_s(IJM)\}/\alpha_s(STR)$ for the bulk of the PEP and PETRA results shown in Table 4.5. The Monte Carlo fragmentation parameters were kept unchanged throughout the range of $\sqrt{s}$ used in the modeling. What Fig. 4.12 shows is that the Mk-J Monte Carlos predict a much smaller difference between STR and IJM fragmentation than the present analysis or the other PEP and PETRA analyses of Table 4.5. This disagreement extends to even relatively small $\sqrt{s}$, and seems to be at the heart of their two published assertions on the lack of model dependence in their measurements of α_s. Interesting also, is the unusually large value of σ_q used by Mk-J in their fits using STR fragmentation (420 MeV/c used by Mk-J, but $\lesssim$300 MeV/c used by the remaining PEP and PETRA experiments: see Fig. 4.10), though Mk-J claims no sensitivity to this parameter.

A more important point concerns the details of the $O(\alpha_s^2)$ cross section used. The Mk-J claims to have calculated virtual corrections (as well as QED and detector effects) with the aid of a Monte Carlo integration, full details of which have yet to be published. Their recent publication states that their result is related to, and is consistent with Gottschalk and Shatz,[48–50] who studied the effects of subleading resolution parameter terms in the $O(\alpha_s^2)$ cross section. These subleading terms were found by these authors to be non-negligible in certain regions of *3-jet* phase space. Gottschalk and Shatz have not yet distributed the corresponding *4-jet* piece of the cross section. Hence, the full effect of subleading terms on α_s fits has yet to be determined for other measurements. Accordingly, the claim that other experiments are in accord with Mk-J results has not in fact been verified.

We conclude that while the Mk-J method is interesting, resolution must await fuller details of the method used.

4.5.4 Comparisons with Remaining Experimental Results

The remaining experiments that measure α_s prefer to instead report $\Lambda_{\overline{MS}}$ given to two loops by the relation

$$\alpha_s(Q^2) = \frac{12\pi}{(33-2n_f)\ln\frac{Q^2}{\Lambda^2} + 6\left(\frac{153-19n_f}{33-2n_f}\right)\ln\ln\frac{Q^2}{\Lambda^2}} \quad ,$$

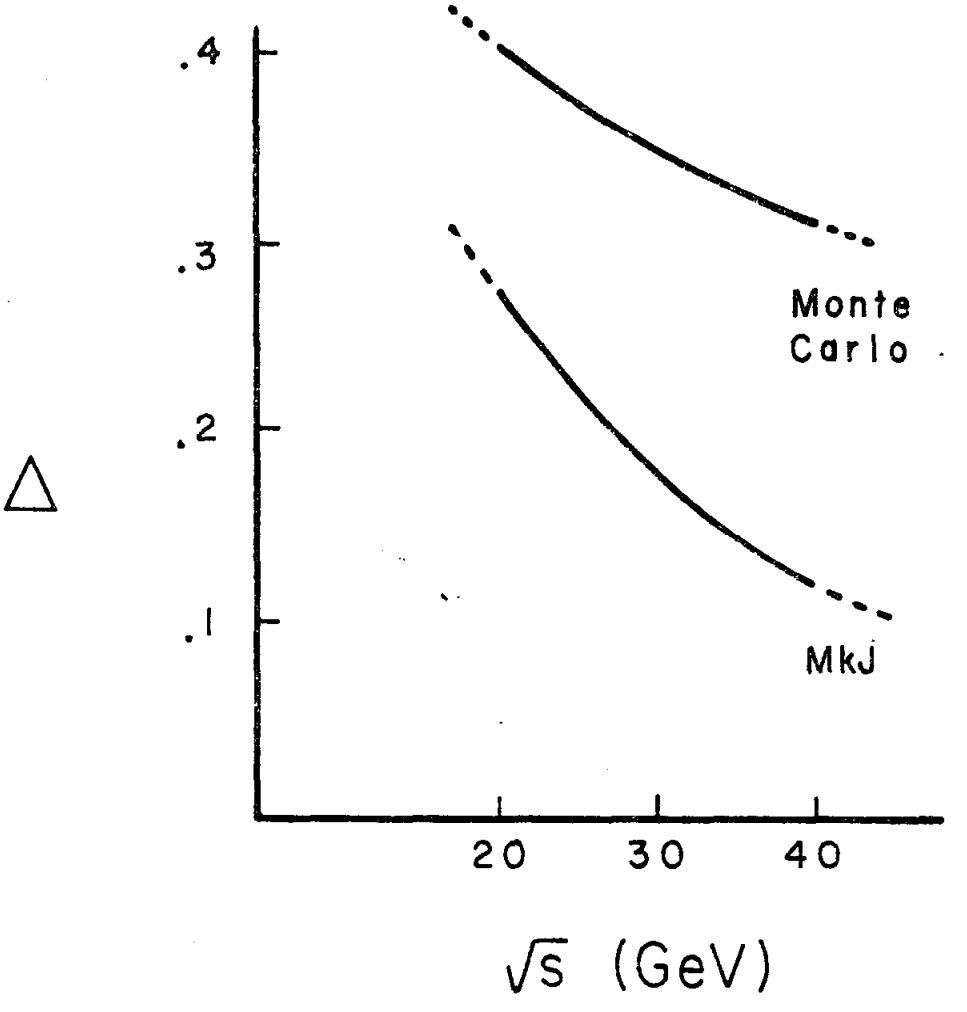

Figure 4.12. Mk-J Δ and Monte Carlo predictions for Δ as a function of $\sqrt{s}$. The Mk-J values are from their most recent publication[42] reporting α_s values. The Mk-J Monte Carlo predicts a smaller difference between IJM and STR fragmentation than seen in the present investigation, or by the rest of the PEP and PETRA experiments.

with n_f the number of available quark flavors. Note that since $\Lambda_{\overline{MS}}$ grows exponentially with α_s, the roughly symmetric errors expected for α_s measurements become grossly asymmetric when converted to $\Lambda_{\overline{MS}}$, as demonstrated in Fig. 4.13. To facilitate comparison with the remaining results, we convert the PEP and PETRA shape, cluster, R and energy-energy correlation asymmetry fits of α_s (shown in Fig. 4.11) into $\Lambda_{\overline{MS}}$, and present the results in Fig. 4.14.

4.5.4.1 Other e^+e^- Experiments

There are two remaining catagories of experiments performed at e^+e^- machines that measure α_s.

The first method, employed at PEP and PETRA, is to measure the shape of the photon structure function $F_2^\gamma(x,Q^2)/\alpha$ in the 2γ process $e^+e^- \rightarrow e^+e^- + \textit{hadrons}$. The Q^2 dependence of F_2^γ at fixed x is given by[51]

$$F_2^\gamma(x,Q^2) \sim \ln(Q^2/\Lambda^2) \quad ,$$

with x interpreted as the momentum fraction of the virtual parton in the photon. The reported fits of Λ to $F_2^\gamma(x,Q^2)/\alpha$ are shown in table Table 4.6, along with the references. The TPC-2γ result is preliminary, but was included as it will probably emerge as the best 2γ measurement of Λ.

The second method of measuring α_s at e^+e^- accelerators is to measure the relative width of the onia resonances into hadrons and muon pairs. The ratio of the hadronic to muonic width is given in the $\overline{MS}$ scheme by[54]

$$\frac{\Gamma_g}{\Gamma_{\mu\bar{\mu}}} = \frac{10(\pi^2-9)}{81\pi q^2}\frac{\alpha_s^3(M^2)}{\alpha^2} \times \left(1 + \frac{\alpha_s(M^2)}{\pi}\left\{-14.0 + \frac{3}{2}(11-\frac{2}{3}n_f)\left[1.161 + \ln(\frac{2M}{M_\Upsilon})\right]\right\} + \ldots\right)$$

where M^2 is the Q^2 scale for α_s, n_f is the number of available quark flavors, M_Υ is the mass of the onia resonance and q is the quark charge. By making the assignment $M \simeq 0.48\,M_\Upsilon$, the $O(\alpha_s^1)$ term in the curly bracket vanishes. The dependence of $\Lambda_{\overline{MS}}$ on M is weak; $\Delta\Lambda_{\overline{MS}} \approx \Delta M \cdot (40\frac{\text{MeV}}{M_\Upsilon})$. The data on the $\Upsilon(1s)$[55],[56] combined with the above expression yields $\Lambda_{\overline{MS}} = 118^{+16}_{-15}$ MeV, where we have used n_f of 4 and set $M = .48 M_{\Upsilon(1s)}$.

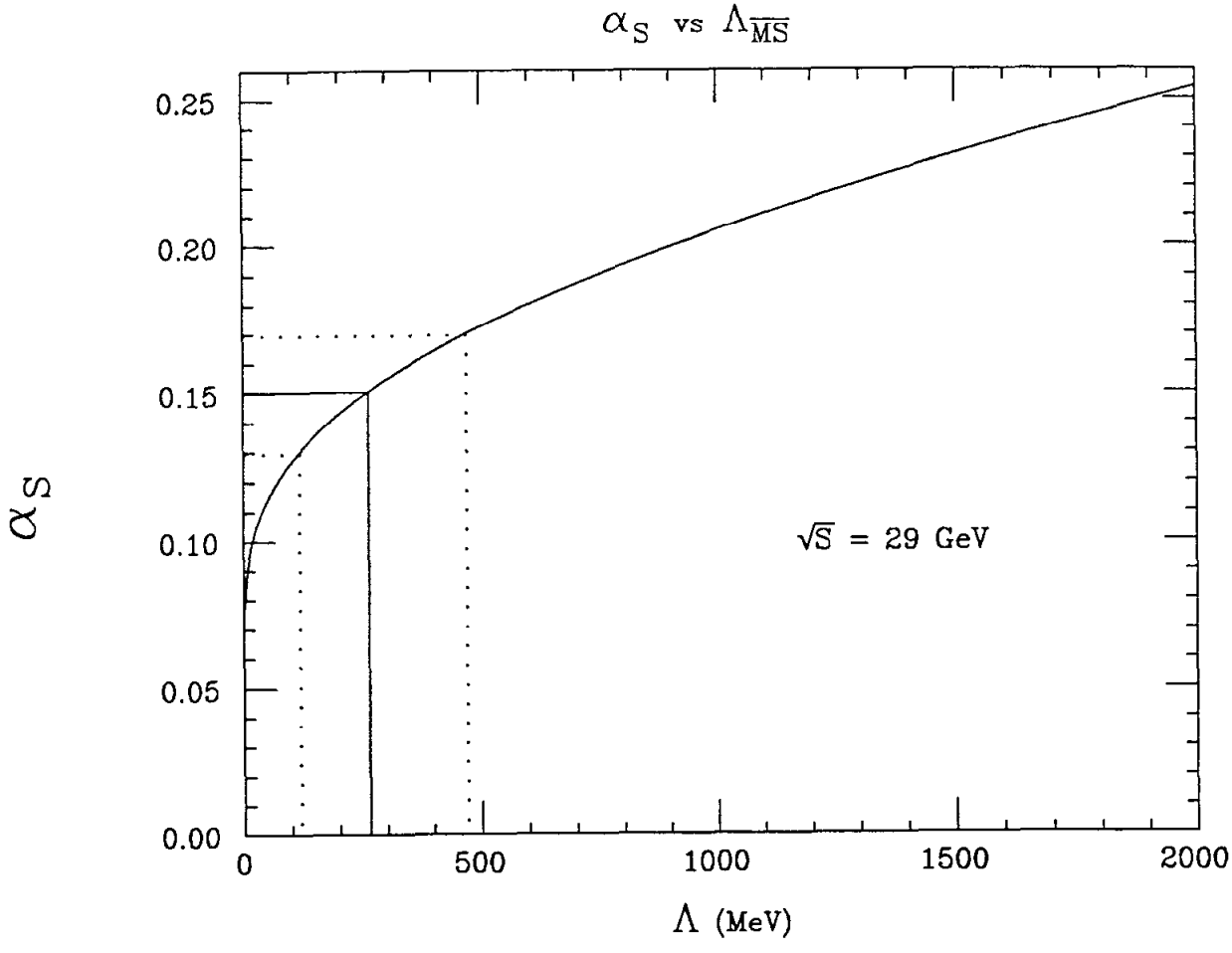

Figure 4.13. α_s vs $\Lambda_{\overline{MS}}$ at $\sqrt{s}$ of 29 GeV. Experiments that study a large range of Q^2 prefer to report the value of $\Lambda_{\overline{MS}}$. Note how errors symmetric in α_s become very asymmetric when converted to errors in $\Lambda_{\overline{MS}}$.

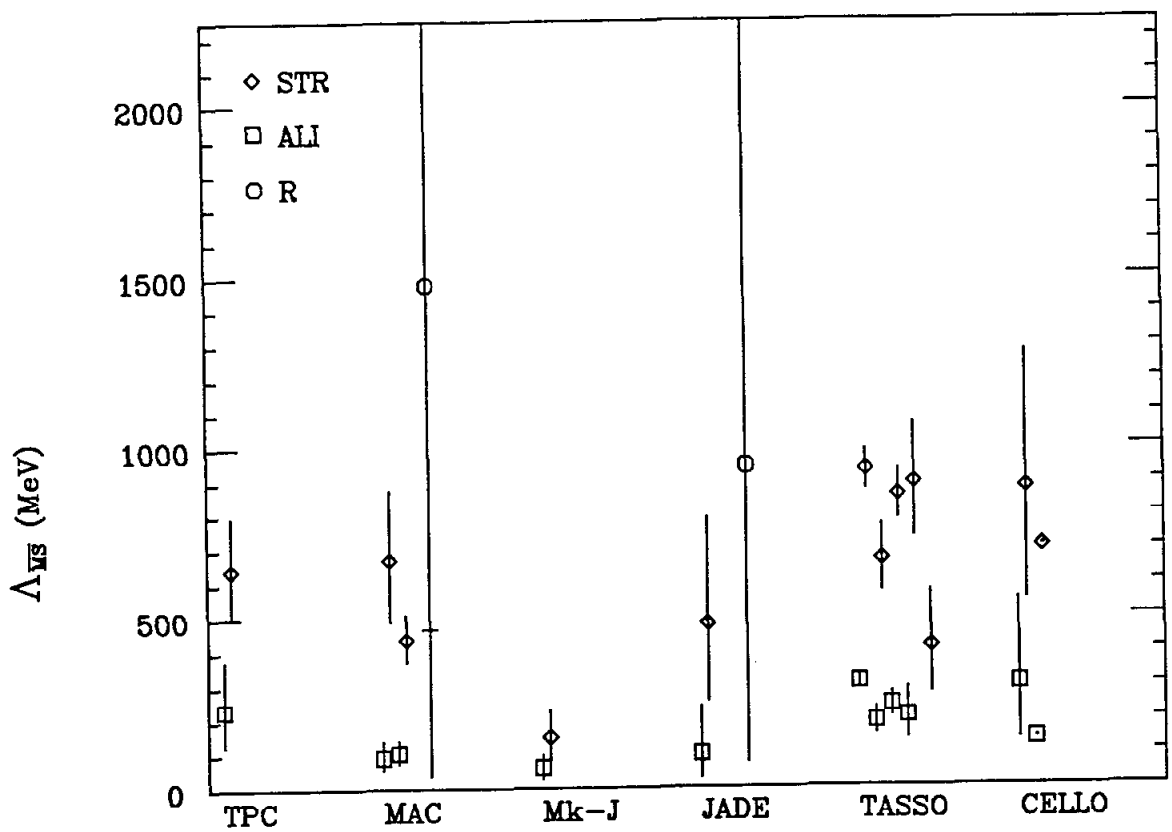

Figure 4.14. PEP and PETRA $\Lambda_{\overline{MS}}$ measurements using shape, cluster, energy-energy correlation asymmetry and R. This contains the same data as Fig. 4.11. Note that both 1σ and 2σ errors are indicated for the MAC R measurement of α_s. The R measurements favor STR models.

Table 4.6. Fits of Λ using $F_2^\gamma(x,Q^2)/\alpha$. The TPC result is preliminary.

Collaboration	Λ MeV/c
PLUTO[52]	190^{+50+60}_{-40-50}
JADE[52]	250 ± 90
TPC-2γ[53]	≈ 200

The values of Λ from F_2^α and the $\Upsilon(1s)$ are shown in Fig. 4.15. These two methods tend to yield $\Lambda \lesssim 200$ MeV.

4.5.4.2 Deep Inelastic Scattering

Deep inelastic lepton scattering experiments fit $\Lambda_{\overline{MS}}$ by measuring scaling violations of the structure functions. Although deep inelastic scattering experiments originated at Stanford and SLAC in the 1960's using electrons as the leptonic probe, the field is now dominated by experiments using the higher energy μ and ν beams available at CERN and FERMILAB.

The dependence of F_2^μ, F_2^ν and F_3^ν on the quark momentum distributions $(u(x), d(x), \ldots)$ is given by[57]

$$F(x)_2^{\mu,\nu} \sim \left[(u+\bar{u}) + (d+\bar{d}) + (s+\bar{s}) + \ldots\right]$$
$$F(x)_3^{\nu} \sim \left[(u-\bar{u}) + (d-\bar{d}) + (s-\bar{s}) + \ldots\right] \quad .$$

There is a QCD effect on the structure functions because QCD branchings serve to distribute the valence quark momentum among the singlet parton components in the nucleon. These fundamental branchings are shown in Fig. 4.16a, and the qualitative effect of the branchings on F_2 are shown in Fig. 4.16b. We see in Fig. 4.16b that when a valence quark emits a gluon, the high x region of F_2 becomes depleted, and the low x region fills in due to the $g \to q\bar{q}$ branchings. The F_3 structure function and the high x region of F_2 are both generically called the nonsinglet structure function F^{ns}, while F_2, including the low x region is called the singlet structure function F^s.

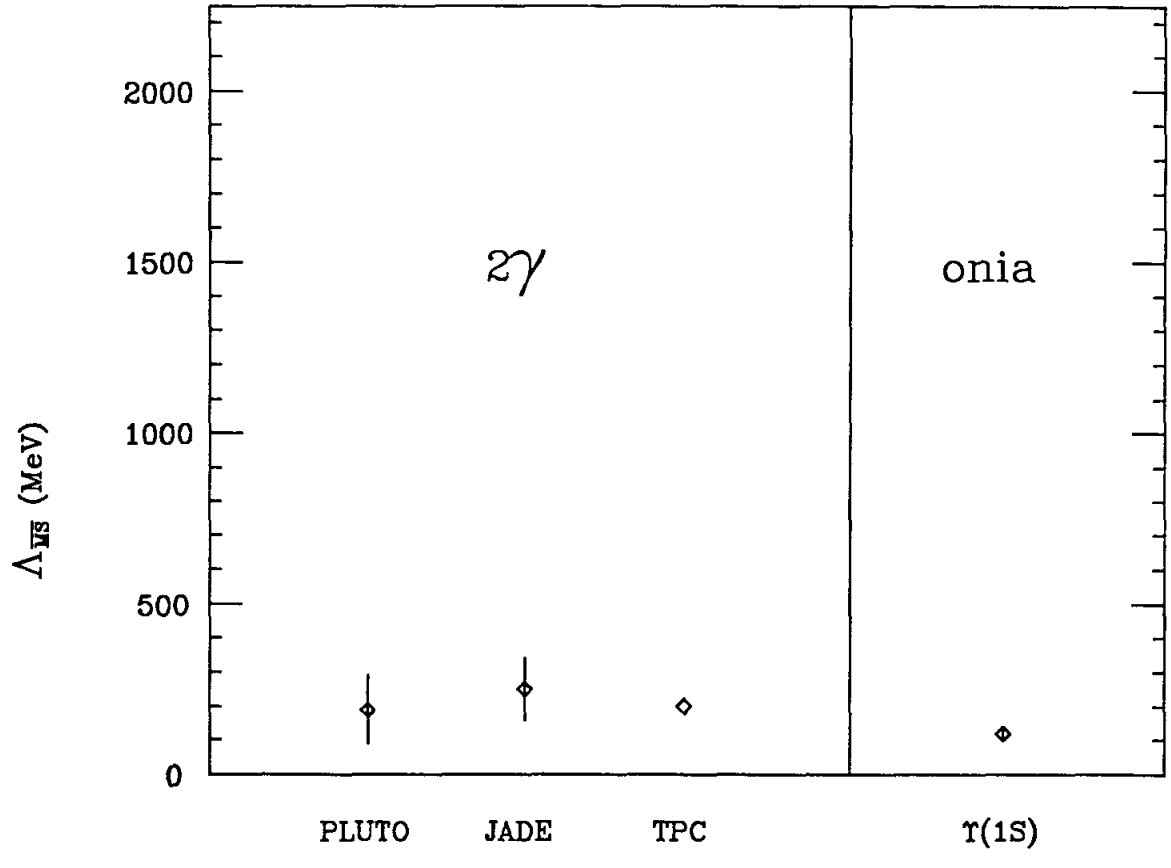

Figure 4.15. Λ from F_2^α and $\Upsilon(1s)$. The scale is the same as that used on Fig. 4.14. The onia and 2γ values of Λ are inconsistent with the hypothesis of STR fragmentation.

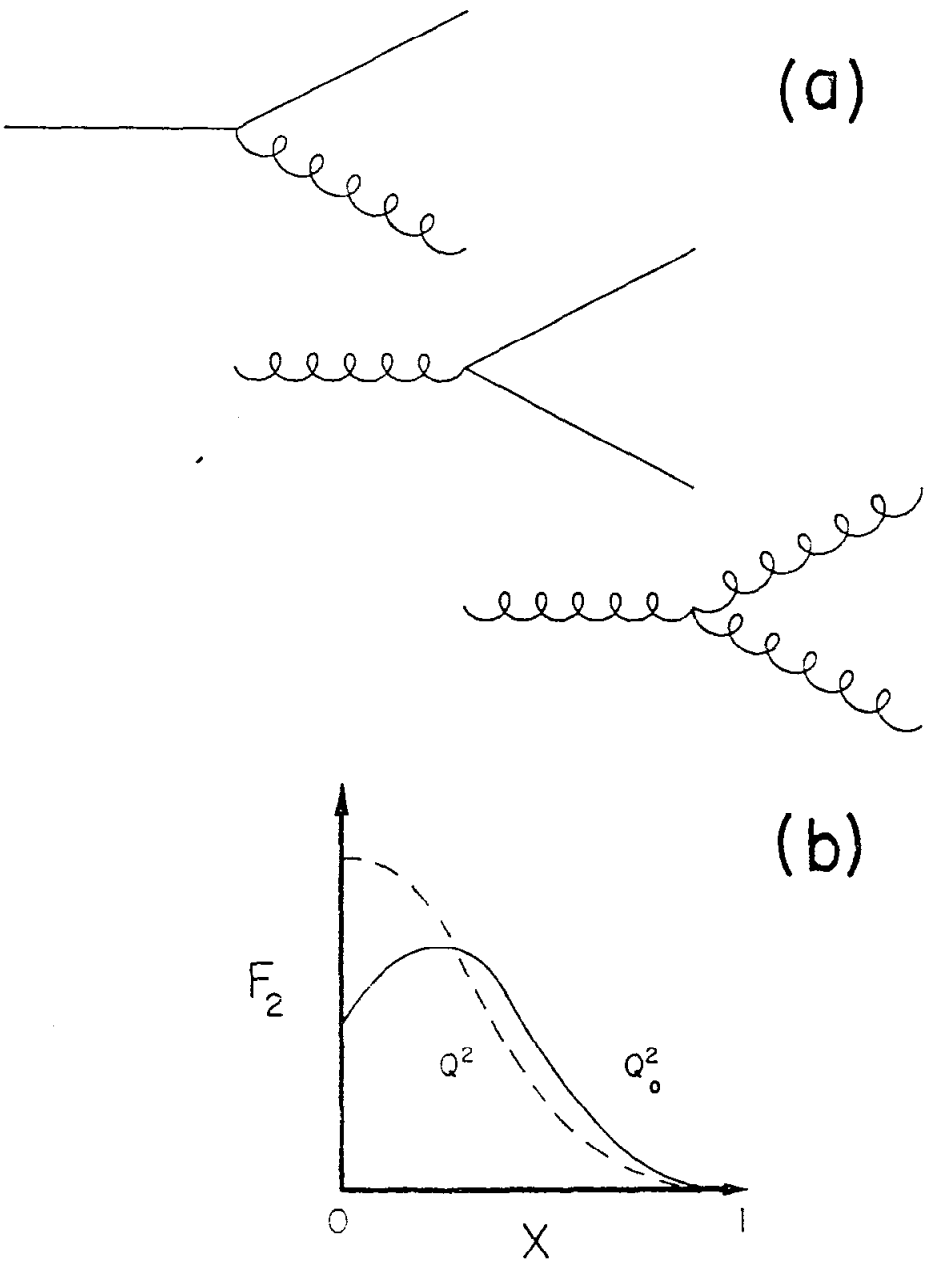

Figure 4.16. Fundamental QCD branchings on quarks and gluons in a nucleon (a). These branchings induce scaling the violations shown qualitatively in (b), where $Q^2 > Q_0^2$.

The recent deep inelastic measurements of α_s use the Altarelli and Parisi splitting formalism[58] where the Q^2 evolution of the structure functions has the form

$$Q^2 \frac{\partial F(x,Q^2)}{\partial Q^2} = \int_x^1 dz F\left(\frac{x}{z}, Q^2\right)\left[\frac{\alpha_s(Q^2)}{\pi} P_{g\to q\bar{q}}(z) + \ldots\right] \quad .$$

The solution $F(x,Q^2)$ is found by numerical methods[59],[60] with $\Lambda_{\overline{MS}}$ the parameter fit to the data. Calculational difficulties limit the fits using F^s to $O(\alpha_s^1)$, while the fits using F^{ns} have been carried out to $O(\alpha_s^2)$.

The reported Λ values (from deep inelastic experiments using the Altarelli and Parisi formalism) are shown in Table 4.7, along with the references. Λ_{lo} is the fit to Λ using a one loop calculation, while $\Lambda_{\overline{MS}}$ is from a fit using a two loop calculation. The first three collaborations in Table 4.7 represent muon scattering experiments, and the remaining three use neutrino beams. The deep inelastic Λ values are shown in Fig. 4.17. In principle, the μ experiments provide the cleanest reconstruction of the scattering kinematics. Of the μ experiments, the EMC result using Hydrogen targets suffer the least from nuclear target effects. The EMC μP experiments give Λ values around 100 MeV.

4.5.4.3 Summary of the Conclusions

There is a large body of α_s and Λ measurements. We summarize the comparisons of the result from this analysis with earlier MAC results, and other α_s measurements.

- MAC results
  - $.16 \lesssim \alpha_s(\mathrm{STR}) \lesssim .20$
  - $.11 \lesssim \alpha_s(\mathrm{IJM}) \lesssim .15$
  - There is model dependence
  - $\alpha_s(\mathrm{STR})$ and $\alpha_s(R)$ are consistent
  - $\alpha_s(\mathrm{IJM})$ and $\alpha_s(R)$ may be inconsistent [$\alpha_s(\mathrm{IJM})$ too small]
- MAC results compared to similar PEP/PETRA results
  - MAC confirms α_s values and model dependence shown in Table 4.5
- MAC results compared to onia, 2γ and deep inelastic
  - R slightly inconsistent (R too big, $\Delta R \approx 1/10$)
  - $\alpha_s(\mathrm{STR})$ inconsistent [$\alpha_s(\mathrm{STR})$ too big]
  - $\alpha_s(\mathrm{IJM})$ consistent

Table 4.7. Fits of $\Lambda_{\rm lo}$ and $\Lambda_{\overline{MS}}$, using the Altarelli and Parisi formalism, from deep inelastic lepton scattering experiments. $\Lambda_{\rm lo}$ is a fit to Λ using a one loop calculation, while $\Lambda_{\overline{MS}}$ is from a fit using a two loop calculation.

collab.	reaction	fit to	$\Lambda_{\rm lo}$ (MeV)	$\Lambda_{\overline{MS}}$ (MeV)	ref
BCDMS	μC	F_2^{ns}	85^{+60+90}_{-40-70}	32^{+20+30}_{-15-25}	61
BFP	μFe	F_2^s	$230 \pm 40 \pm 80$		62
EMC	μP	F_2^{ns}	$110^{+58+124}_{-46-69}$	$139^{+68+156}_{-56-87}$	63 64
		F_2^s	81^{+36+44}_{-30-32}		64
	μFe	F_2^{ns}	$122^{+22+144}_{-20-70}$	$173^{+29+158}_{-27-97}$	63 64
		F_2^s	163^{+22+99}_{-22-64}		64
CCFRR	νFe	F_2^s	360 ± 100	340 ± 100	65
		xF_3^{ns}	88^{+163}_{-78}		65
		xF_3^{ns}, F_2^{ns}	266^{+114}_{-104}		65
		xF_3^{ns}		120^{+200}_{-106}	65
		xF_3^{ns}		193^{+272}_{-156}	65
CHARM	$\nu CaCO_3$	xF_3^{ns}	$187^{+130}_{-110} \pm 70$	$310 \pm 140 \pm 70$	66 67
		$xF_3^s, F_2^s, \bar{Q}$	$190^{+70}_{-40} \pm 70$		66
CDHS	νFe	xF_3^{ns}	200^{+200}_{-100}		68
		$F_2^{ns}(R = R_{QCD})$	275 ± 80	300 ± 80	68
		$F_2^{ns}, \bar{Q}(R = .1)$	180 ± 20		68
		$F_2^{ns}, \bar{Q}(R = R_{QCD})$	290 ± 30		68

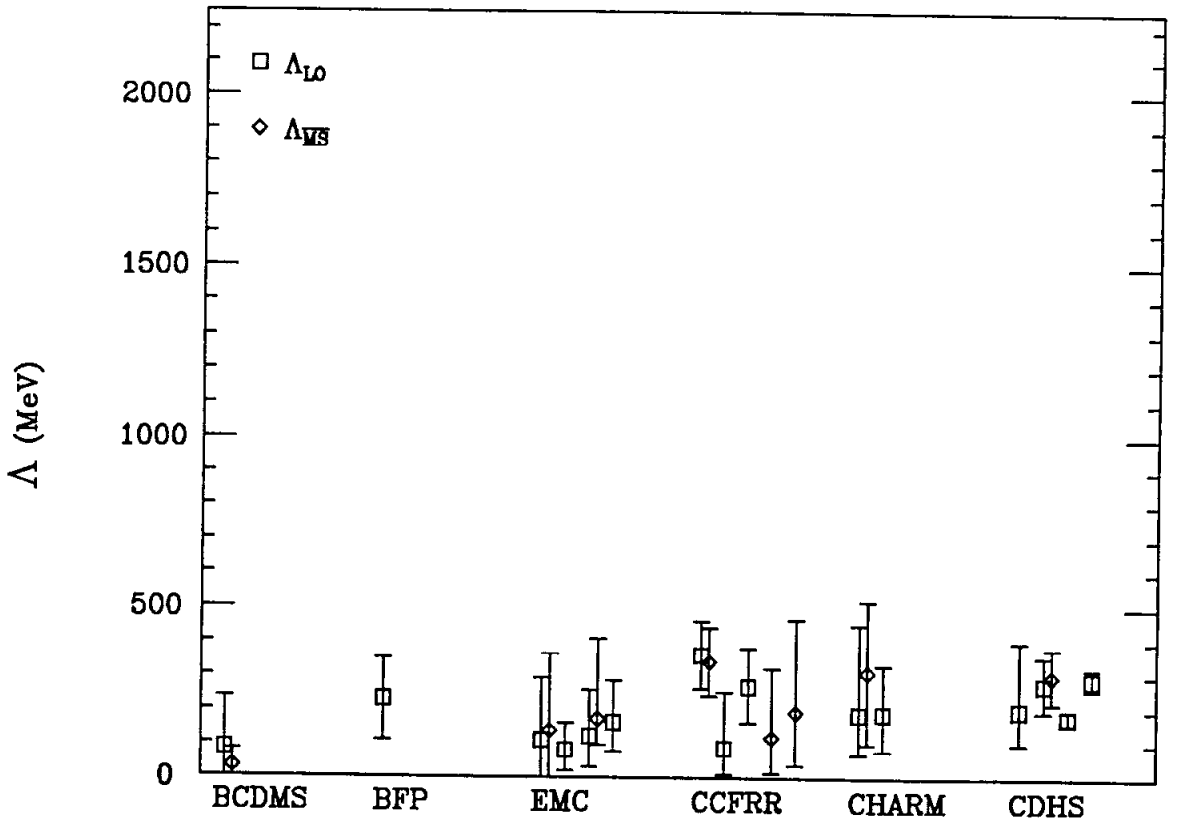

Figure 4.17. Λ_{lo} and $\Lambda_{\overline{MS}}$ measurements, using the Altarelli and Parisi formalism, from deep inelastic lepton scattering experiments, Λ_{lo} is a fit to Λ using a one loop calculation, while $\Lambda_{\overline{MS}}$ is from a fit using a two loop calculation. The scale is the same as that used on Fig. 4.14. Like the onia and 2γ values of Λ, the Λ values from deep inelastic scattering tend to be smaller than expected from STR fragmentation.

5. Event Selection for the Energy Flow Analysis

In the previous chapter, the χ^2 fits of α_s to the whole of the $hE_\perp^{in}(\text{fat})$ distribution showed a difference between the model hypotheses in the goodness of fit. Expanding on this theme, the following two chapters examine rather subtle aspects of the hadronic energy flow in order to determine which of the fragmentation models better describe the data. We will be explicitly looking for asymmetries in energy flow around the thin jet in the event plane. This analysis calls for a sample of events enriched with a hard gluon bremsstrahlung component; the hard gluons resulting in *3-jet* events. The selection of this gluon enriched event sample is the focus of this chapter.

5.1 *3-jet* Filter

We start with the events selected by the quality filter, the selection of which was illustrated schematically in Fig. 3.4. These 21061 events are passed through a filter, called the *3-jet* filter, the purpose of which is to enhance the population of *3-jet* events in the sample. The choice of cuts used by the *3-jet* filter arose from consideration of several statistical tendencies. One tendency is for *3-jet* events to appear in the $P_\perp$ spectrum as an enhancement in the high $P_\perp$ tail. This is an observation from the previous chapter and a well known method of *3-jet* tagging. Heavy quarks can also show such an enhancement, but then the effect tends to appear in both jets. A light quark pair radiating one hard gluon tends to produce $P_\perp$ enhancement in only one jet. In a statistical sense then, *3-jet* events involving light primary quarks selectively "fatten" one jet.

5.1.1 Formal Cuts for the 3-jet Filter

The selection is achieved by requiring that one hemisphere of the event fragment "fat", and the other fragment "thin". Formally, we demand:

$$\frac{hE_\perp^{in}}{E_{vis}}\begin{pmatrix} one \\ side \end{pmatrix} > 0.18 \qquad \text{and} \qquad \frac{hE_\perp^{in}}{E_{vis}}\begin{pmatrix} other \\ side \end{pmatrix} < 0.18$$

Figure 5.1a shows the placement of this cut. The precise placement of this cut is constrained at the extremes by two considerations. While *2-jet* events don't contribute to an asymmetry, the sheer number of *2-jet*-like events dilutes the slight asymmetry expected from string models. So, in the interest of enhancing the signal to noise ratio, we are tempted to place the $hE_{\perp}^{in}/E_{vis}$ cut at the largest value consistent with maintaining good statistics. However, as the cut becomes harder, the number of events with gluons as the first or second hardest parton is enhanced. These events containing a very hard gluon have an opposite sign asymmetry. The procedure that led to placement of the $hE_{\perp}^{in}/E_{vis}$ cut at 0.18, and the effect of the cut placement on the thin jet asymmetry is discussed in the next chapter.

There is an additional energy flow asymmetry, entering with the same asymmetry expected from string fragmentation, as a result of the detector response to hard radiative photons. To exclude this hard photon contribution, we require that the hadronic jets be almost back-to-back,

$$160^{\circ} < \cos^{-1}\left\{\hat{T}_{hemi}\begin{pmatrix} one \\ side \end{pmatrix} \bullet \hat{T}_{hemi}\begin{pmatrix} other \\ side \end{pmatrix}\right\}$$

where

$$\hat{T}_{hemi}\begin{pmatrix} one \\ side \end{pmatrix} \equiv \frac{\sum_i \vec{E}_{\parallel i}}{|\sum_i \vec{E}_i|} \quad \begin{array}{l} i \text{ runs over all two-ended calorimeter hits on the} \\ \text{same side of the event relative to the thrust axis} \end{array}$$

and

$$\hat{T}_{hemi}\begin{pmatrix} other \\ side \end{pmatrix} \equiv \frac{\sum_i \vec{E}_{\parallel i}}{|\sum_i \vec{E}_i|} \quad \begin{array}{l} i \text{ runs over all two-ended calorimeter hits on the} \\ \text{other side of the event relative to the thrust axis} \end{array}$$

This cut serves to eliminate hard low angle radiative photons with missing energy, or photons radiated at wide angles relative to either hadron jet into the calorimetry where the higher energy deposition of a photon electromagnetic shower relative to a hadron interacting in the lead of the shower chambers skews the direction of $\hat{T}_{hemi}$. Figure 5.2 shows the placement of the cut. Recall from Table 2.1 that E_e/E_π deposited in the MAC shower chambers is approximately 2. However, since hadronic events contain a substantial electromagnetic component, the ratio of interest is E_e/E_{had} which is approximately 1.5 .

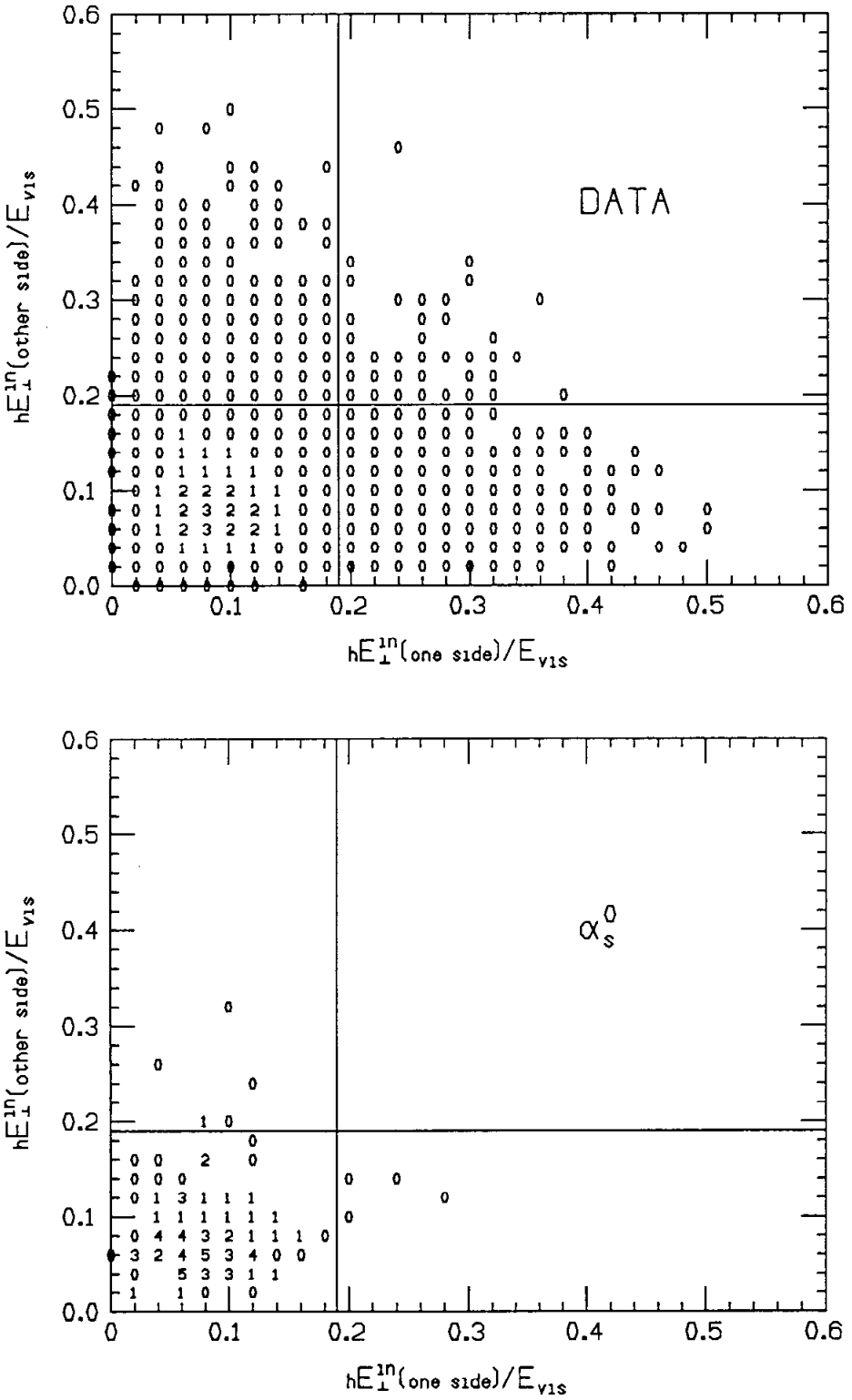

Figure 5.1. Placement of cuts used in the *3-jet* filter:
$hE_\perp^{in}\binom{one}{side}/E_{vis}$ vs. $hE_\perp^{in}\binom{other}{side}/E_{vis}$ for (upper figure) Data passed by the quality filter; (lower figure) corrected $O(\alpha_s^0)$ Monte Carlo events. Three jet events are selected by the cut. Each unit of the z-axis accounts for 10^{-3} units of N/N_{tot}.

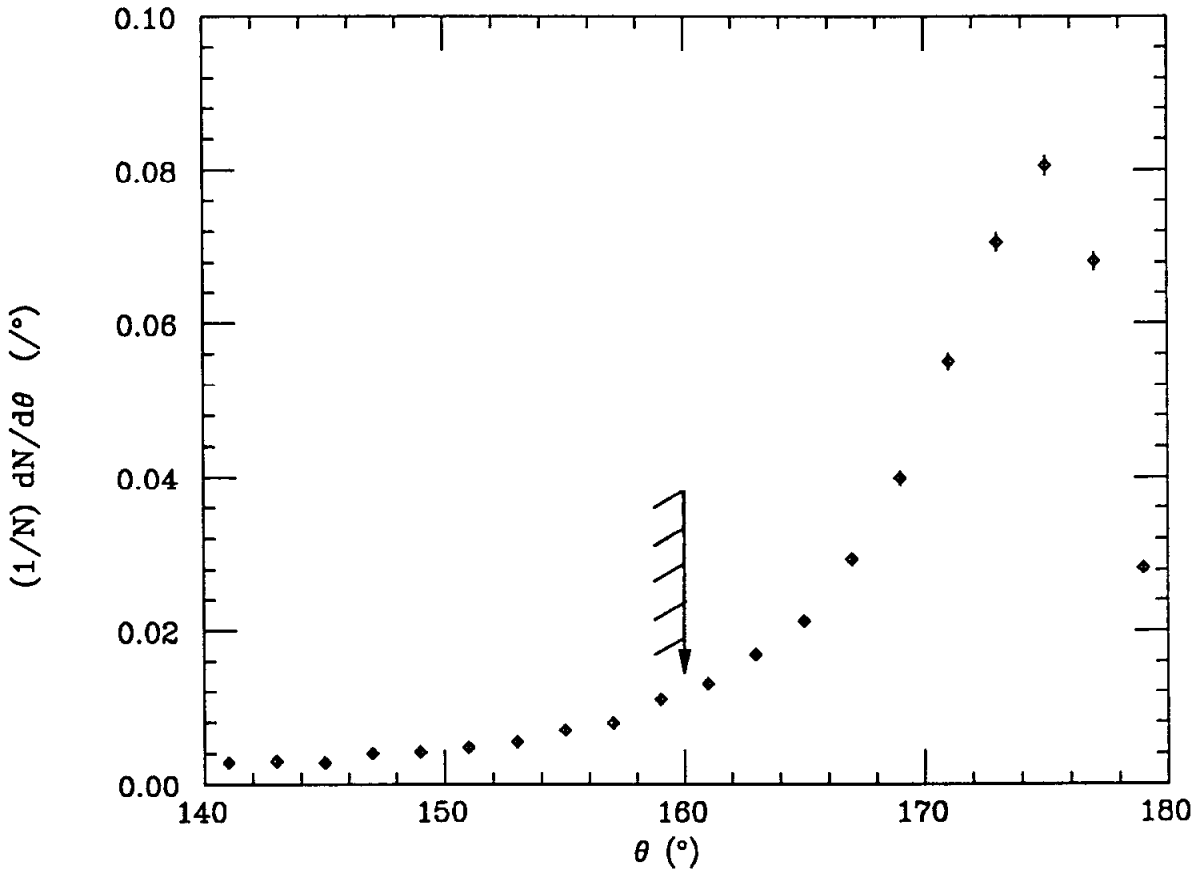

Figure 5.2. Back to back angle between $\hat{T}_{hemi}\binom{one}{side}$ and $\hat{T}_{hemi}\binom{other}{side}$. The greater energy deposition from electromagnetic showers skews the direction of the whole event thrust axis. This would generate an artificial asymmetry. Hard radiative photons are eliminated by requiring a back-to-back angle between the hemispheric thrust axes for the two jets.

Table 5.1. *3-jet* filter cuts: correlations.

% of events passing cut

	cut on hemi-thrust opening angle	cut on $hE_{\perp}^{in}/E_{vis}\binom{one}{side}$ vs $hE_{\perp}^{in}/E_{vis}\binom{other}{side}$
cut on hemi-thrust opening angle	92	22
cut on $hE_{\perp}^{in}/E_{vis}\binom{one}{side}$ vs $hE_{\perp}^{in}/E_{vis}\binom{other}{side}$		24

Acceptances for individual cuts of the *3-jet* filter is are given in Table 5.1. About 20% of the events passed by the quality filter pass the *3-jet* filter cuts. The overall acceptance for the combined quality filter and *3-jet* filter is about 4%, corresponding to a final data sample of 5017 events.

5.1.2 Acceptance of the Event Filters for Various Classes of Events

The *3-jet* filter is designed to generate a significant enhancement of *3-jet* events. An additional goal is to reduce the QED radiative background of $e^+e^- \rightarrow q\bar{q}\gamma$. The efficiencies and acceptances for radiative gluons and photons through the cuts of the *3-jet* filter are considered separately in the following sections.

5.1.2.1 Hard Radiative Photons

A Monte Carlo simulation of the energy spectrum of photons passing the quality filter is shown in Fig. 5.3 (diamonds), and should be compared to the predicted energy spectrum for radiative photons passing the *3-jet* filter, also shown in Fig. 5.3 (squares). The very hard photon component of the spectrum is significantly reduced,

with the mean photon energy, for the photon energy cutoffs discussed in Appendix A, falling 60% to 0.7 GeV from 1.8 GeV.

5.1.2.2 3-jet Events

The *3-jet* filter is designed to pass events containing radiative gluons. The efficiency is determined with Monte Carlo techniques. A Monte Carlo data file is prepared in the usual way (see Appendix A), except that single quark pairs are the only allowed primary partons. This $O(\alpha_s^0)$ simulation is then compared to the usual $O(\alpha_s^2)$ simulation with respect to $E_\perp^{in}$. Figure 5.1b shows a scatterplot of $hE_\perp^{in}/E_{vis}\binom{one}{side}$ vs. $hE_\perp^{in}/E_{vis}\binom{other}{side}$ for the $O(\alpha_s^0)$ file. The difference between Fig. 5.1a and Fig. 5.1b is solely due to events containing radiative gluons.

By varying the cut "x" in the passing criteria

$$\frac{hE_\perp^{in}}{E_{vis}}\binom{one}{side} > x \qquad \text{and} \qquad \frac{hE_\perp^{in}}{E_{vis}}\binom{other}{side} < x,$$

the acceptance of the *3-jet* filter varies, along with the level of $O(\alpha_s^0)$ contamination. Shown in Fig. 5.4 is the acceptance for $O(\alpha_s^2)$ events $(q\bar{q} + q\bar{q}g + \cdots)$ as a function of x (the usual 20° colinearity is still required). Also shown in Fig. 5.4 is the corresponding level of $q\bar{q}$ contamination. At x of 0.18, about 20% of the quality filter events are passed by the *3-jet* filter, with a contamination of $\sim$ 25% from $O(\alpha_s^0)$ events.

5.2 *3-jet* Filter Acceptance as a Measure of α_s

As a consistency check, it is worthwhile to note that a crude measure of α_s results from counting the number of events passing the *3-jet* filter. Since the *3-jet* filter selects *3-jet* events, the acceptance of the filter will depend on α_s. In Fig. 5.5 is shown the predicted acceptance of the *3-jet* filter for particular models of IJM and STR fragmentation. The acceptance for the data is shown by the dotted line. These measured α_s for the two model hypothesis are given approximately by:

$$\alpha_s = \begin{cases} 0.13 & IJM \\ 0.18 & STR \end{cases} .$$

These α_s values are in agreement with results from Chapter 4. Notable about this result is the observation that a fit to the STR hypothesis measures an α_s about

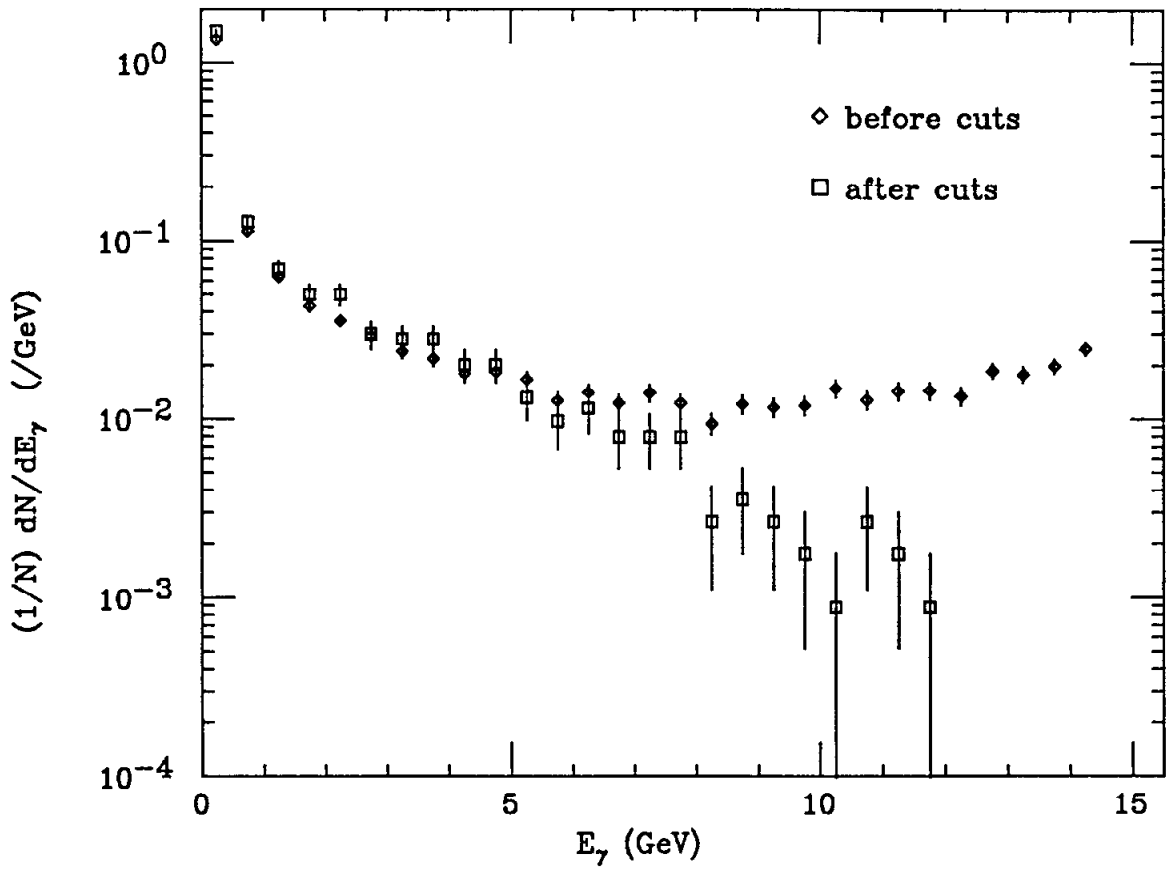

Figure 5.3. Monte Carlo prediction for the initial state photon spectra for Monte Carlo events passing the quality filter (diamond); Monte Carlo events passing the *3-jet* filter (square). The back-to-back cut on the hemispheric thrust axes directions reduces the hard electromagnetic component of hadronic events.

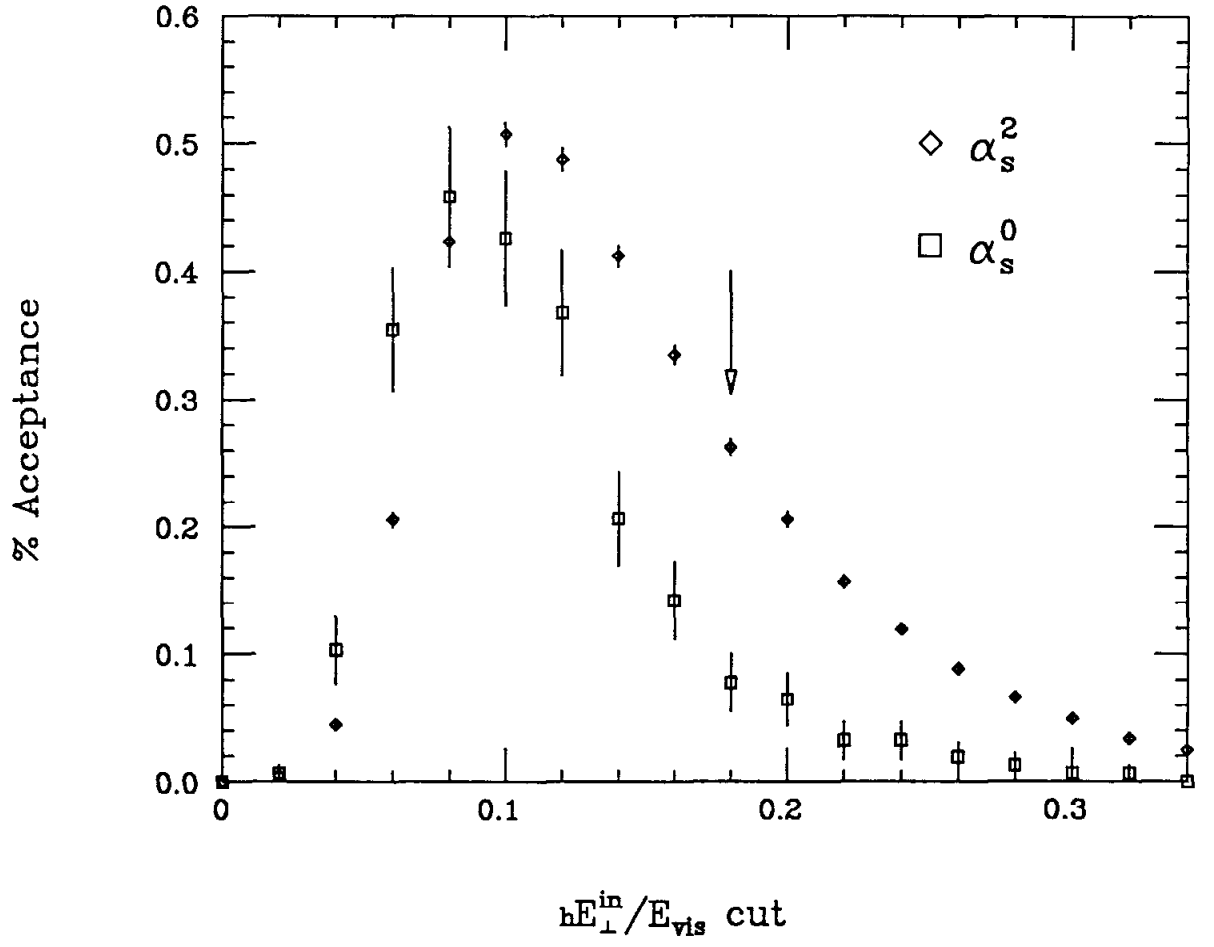

Figure 5.4. Acceptance for $O(\alpha_s^2)$ (diamond) and $O(\alpha_s^0)$ (square) events passed by the *3-jet* filter. The *3-jet* component is significantly enhanced.

50% larger than the fit to the IJM hypothesis. That there is a difference between models we have earlier observed in Chapter 4 to be characteristic of fits of α_s. One effect of the string then, is to modify the energy flow in the jet containing the gluon to yield a smaller jet $E_\perp$. Further model dependence of the energy flow asymmetry around the thin jet in the event plane for hadronic events is considered in the next chapter.

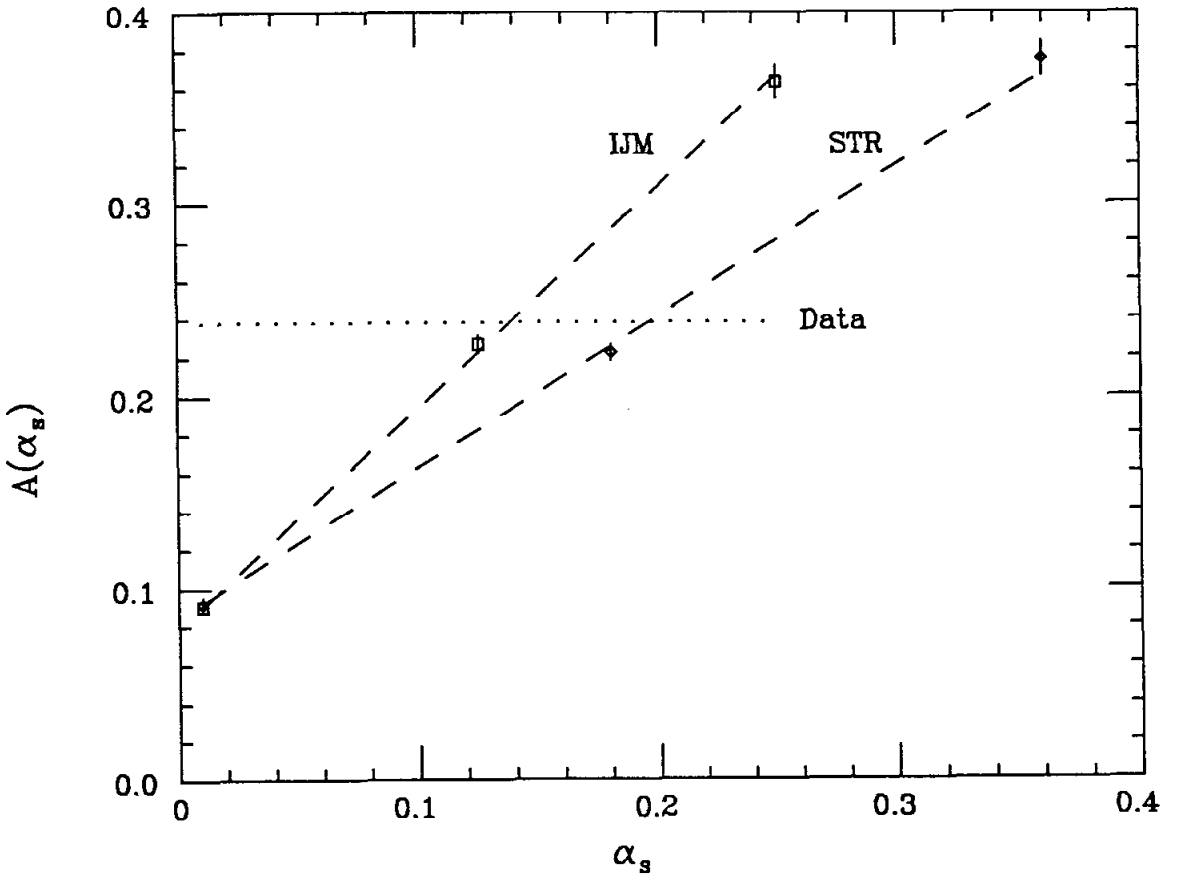

Figure 5.5. Acceptance of the *3-jet* filter as a function of α_s for (a) a particular IJM model, and (b) a particular STR model. The dotted line is the measured acceptance for the data. The α_s values are in agreement with results of Chapter 4.

6. The Energy Flow Analysis

We have previously seen in Fig. 1.8 that different fragmentation models provide differing predictions for the energy flow in the regions between the primary partons. There are three separate operations that were applied to $O(\alpha_s^1)$ skeletons in order to generate this figure. First, all skeletons were oriented to lie in the same plane. Next, the skeletons were rotated around the event plane so that the harder quark direction coincided with the 0° direction in the plane. Finally, if necessary, the parton skeleton was flipped around the axis of the harder quark so that the gluon was on a specific side of the event plane. The difference in energy flow between IJM and STR fragmentation for the parton skeleton of Fig. 1.8 is as large as a factor of four in the region between the quark and anti-quark jets. However, this rather dramatic difference between the energy flow of between the models is difficult to observe experimentally. The reason is that we do not know the parton directions in a hadronic event. The parton directions must be inferred from those of the final state particles, and are necessarily only approximations. The less than perfect efficiency for determining the parton orientation considerably reduces the magnitude of the observed differences in energy flow. Nonetheless, there are observable effects; one of which is an energy flow asymmetry around the thin jet in a *3-jet* event. We look at this particular aspect of the energy flow, using the data sample discussed in the previous chapter.

6.1 Standard Event Orientation

In order to investigate the effects demonstrated in Fig. 1.8, we must look at the energy flow of hadronic events with the events placed in a standard orientation. We wish this standard orientation to have the following simple correspondence when applied to $O(\alpha_s^1)$ hadronic events:

- The hadronic event plane should correspond to the parton event plane.

- The direction of the thin hadron jet should correspond to the direction of the harder of the two quarks.
- The less energetic side of the fat hadron jet should correspond to the gluon side of the parton event plane.

When these correspondences are violated, the signal to noise ratio in the energy flow analysis is reduced. The accuracy of these correspondences is discussed in the following section.

6.1.1 Reconstruction of the Parton Event Plane

The starting point is to take the events selected by the *3-jet* filter, discussed in the previous chapter, and reconstruct the original parton event plane orientation and thrust axis direction. The original parton thrust axis is reconstructed rather well. From Monte Carlo simulation, Fig. 6.1a shows the difference in angle between the parton thrust axis direction, and the thrust axis direction after fragmentation and calorimeter simulation. The difference in angle is about 5°. Some of this difference is due to details of the fragmentation process, and some to detector effects. We show in Fig. 6.1b the difference in angle between the parton thrust axis direction and the thrust axis direction after fragmentation, as measured by an ideal detector. It can be seen that a significant portion of the parton thrust axis misassignment is inherent in the fragmentation process.

As a measure of how well the parton event plane is determined, we compare the difference in angle between the major-axis direction, and the major-axis direction deduced calorimetrically, in Fig. 6.2a, according to a Monte Carlo. The angular difference is about 20°; larger than the thrust axis mismeasurement. Again, we isolate the amount of this difference due solely to fragmentation effects by comparing, in Fig. 6.2b the difference in direction between the parton major-axis direction, and the major-axis direction as measured by an ideal detector. We again note that a significant part of the parton event plane mismeasurement is inherent in the fragmentation process. The larger misassignment of the major axis direction may be partially offset by projecting the calorimeter energy vectors onto the event plane.

The angle differences shown in Fig. 6.2a and b are relatively insensitive to the choice of fragmentation model.

6.1.2 Reconstruction of the Harder Quark Direction

In order to look at energy flow around the event plane, a 0° direction in the

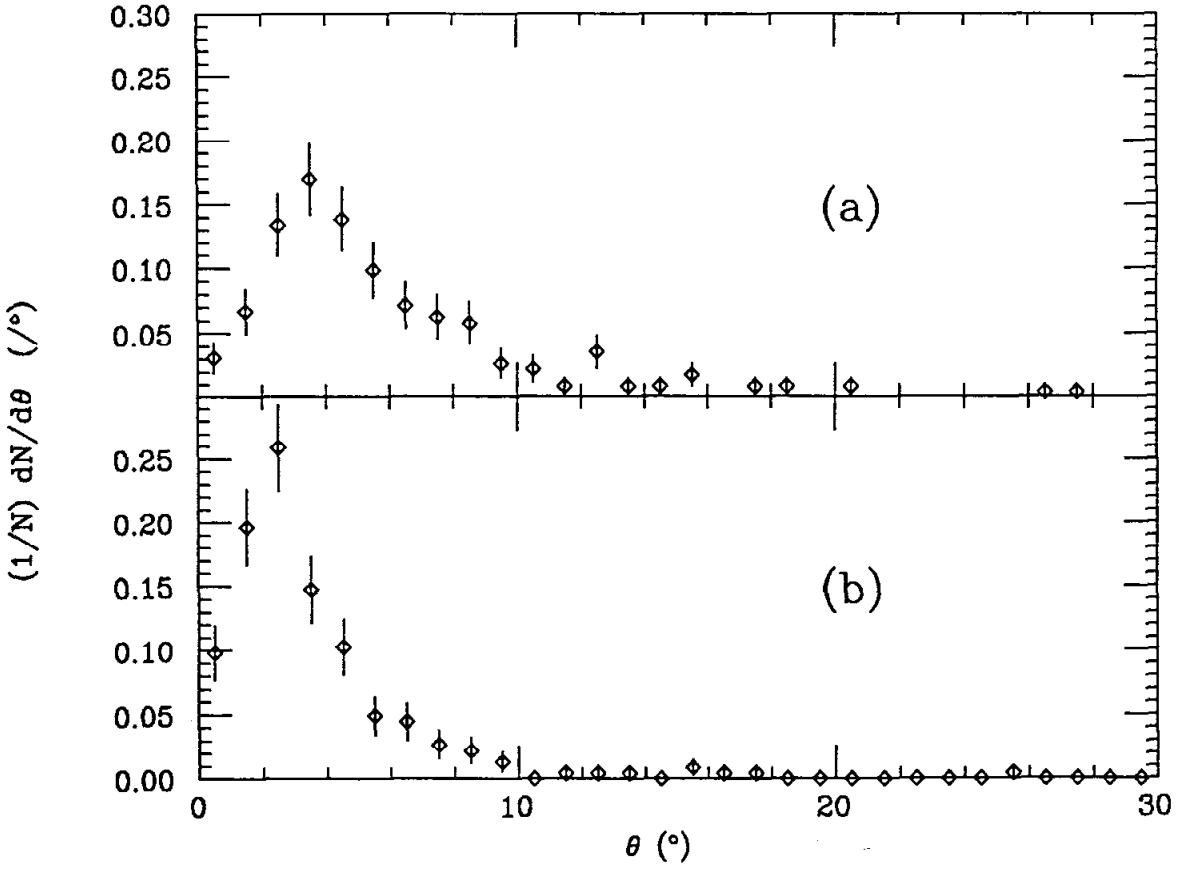

Figure 6.1. Thrust direction misassignment estimated by Monte Carlo: (a) Angle between the parton and final state thrust direction, corrected for detector effects; (b) Angle between the parton and final state thrust direction, uncorrected for detector effects. A significant amount of the thrust direction misassignment is inherent in the fragmentation.

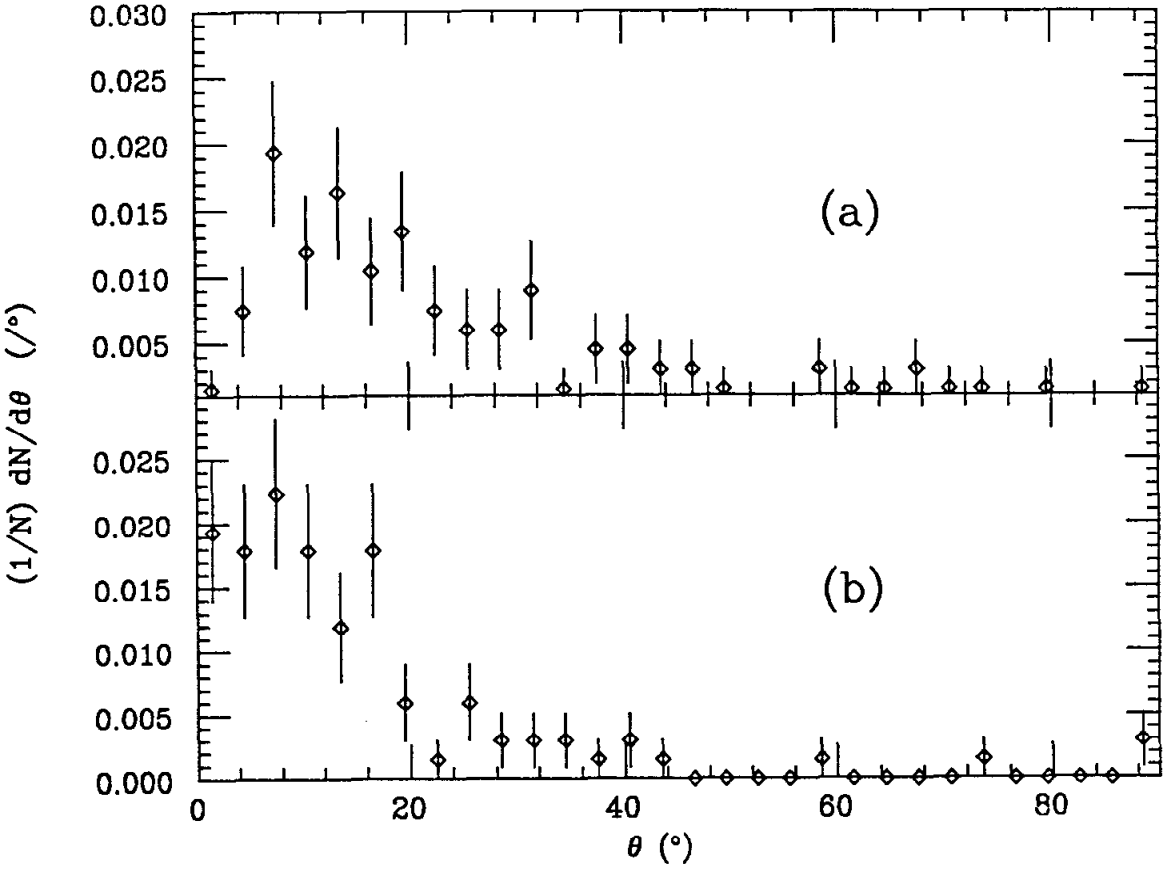

Figure 6.2. Major axis direction misassignment estimated by Monte Carlo: (a) Angle between the parton and final state major axis direction, corrected for detector effects; (b) Angle between the parton and final state major axis direction, uncorrected for detector effects. A significant amount of the error in determining the event plane is due to the fragmentation.

plane needs to be defined. If the ideal "Mercedes" skeleton of Fig. 1.7 is recalled, a sensible choice of 0° direction is along the direction of the harder quark momentum. Not knowing the harder quark direction in a hadronic event, we experimentally define the 0° direction to be along the hemispheric thin jet thrust axis and directed towards the thin jet. Fragmentation on the side of the event having smaller $hE_\perp$ is attributed to products of the isolated quark. For α_s^1 events in a gluon enriched sample, the assignment of 0° to the isolated quark side is correct about 80% of the time.

6.1.3 Reconstruction of the Gluon Side of the Event Plane

The handedness of the event plane is still to be determined, *i.e.* what direction is a positive angular displacement away from 0°? Since gluons have a dk/k bremsstrahlung spectrum, they tend to have less energy than the associated quark. Motivated by this feature of gluon kinematics, the hemisphere containing the fat jet is divided into two $\frac{1}{4}$*spheres* along the plane transverse to the event plane and containing the thrust axis. In general, the $\frac{1}{4}$*sphere* containing the lesser energy of the two subtends the gluon quadrant of the event plane. Angular displacements from 0° in the direction of the lesser energy quadrant are defined to be negative displacements. Pictorially, we have the scheme of Fig. 6.3. Judging from Monte Carlo α_s^1 events, a correct sign determination is made about 70% of the time.

This method of selecting the gluon side of the event plane is the limiting factor in extracting the signal and warrants further discussion. For simplicity, we use in this discussion the $O(\alpha_s^1)$ matrix element for the gluon bremsstrahlung process $g \to q\bar{q}$ given by[69]

$$\frac{d^2\sigma(q\bar{q}g)}{dx_q dx_{\bar{q}}} = \sigma_0 \frac{\alpha_s}{\pi} \frac{2}{3} \frac{x_q^2 + x_{\bar{q}}^2}{(1-x_q)(1-x_{\bar{q}})} \quad ,$$

with σ_0 the QED $e^+e^- \to q\bar{q}$ total cross section, $x_q = E_q/E_{beam}$, $x_{\bar{q}} = E_{\bar{q}}/E_{beam}$, and $x_g = E_g/E_{beam}$ (so that $x_q + x_{\bar{q}} + x_g = 2$). A scatterplot of the x_q and $x_{\bar{q}}$ density is shown in Fig. 6.4. Energy conservation dictates the constraint $x_q + x_{\bar{q}} > 1$ shown in the figure. The three possible energy orderings of the partons in $O(\alpha_s^1)$ are shown in Fig. 6.5. The first skeleton (a) represents the desired configuration for analyzing energy flow asymmetry; the gluon is the least energetic parton. It is for this topology that our criterion for choosing the gluon side of the event plane is correct. The other two skeletons represent undesirable configurations where (b)

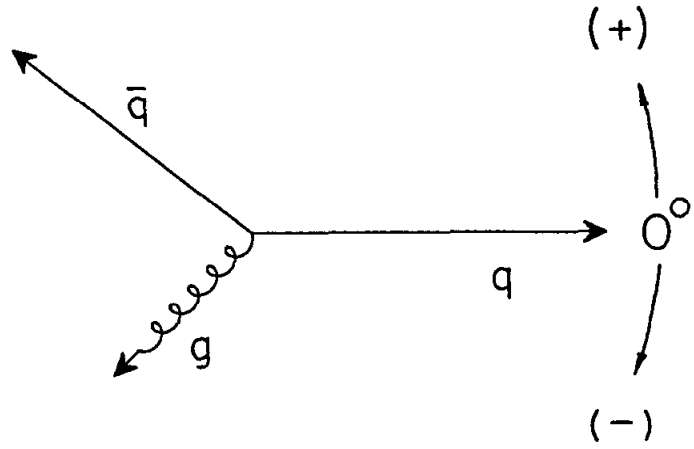

Figure 6.3. Event plane sign convention: angular displacements away from the thin jet towards the gluon of the fat jet are assigned negative displacements. This is the standard orientation of an event.

the gluon is harder than the associated quark, or (c) the gluon is the most energetic parton. Here, our criterion results in the wrong assignment of the gluon side of the event plane. These undesirable configurations don't contribute, however, an asymmetry of the same sign as that expected from string like fragmentation of the skeleton of Fig. 6.5a. The skeleton of Fig. 6.5b introduces an asymmetry with the opposite sign, while the skeleton of Fig. 6.5c introduces no asymmetry. The good region corresponding to parton topologies like those of Fig. 6.5a is given by the constraint $2 - x_q - x_{\bar{q}} < \min(x_q, x_{\bar{q}})$. With reasonable IR cuts on the $O(\alpha_s^1)$ QCD matrix element, this good region accounts for most of the parton topologies generated.

We see that the precise placement of the $hE_\perp^{in}$ cut in the *3-jet* filter must be chosen carefully. If the $hE_\perp^{in}$ cut is very low, the acceptance is high (see Fig. 5.4).

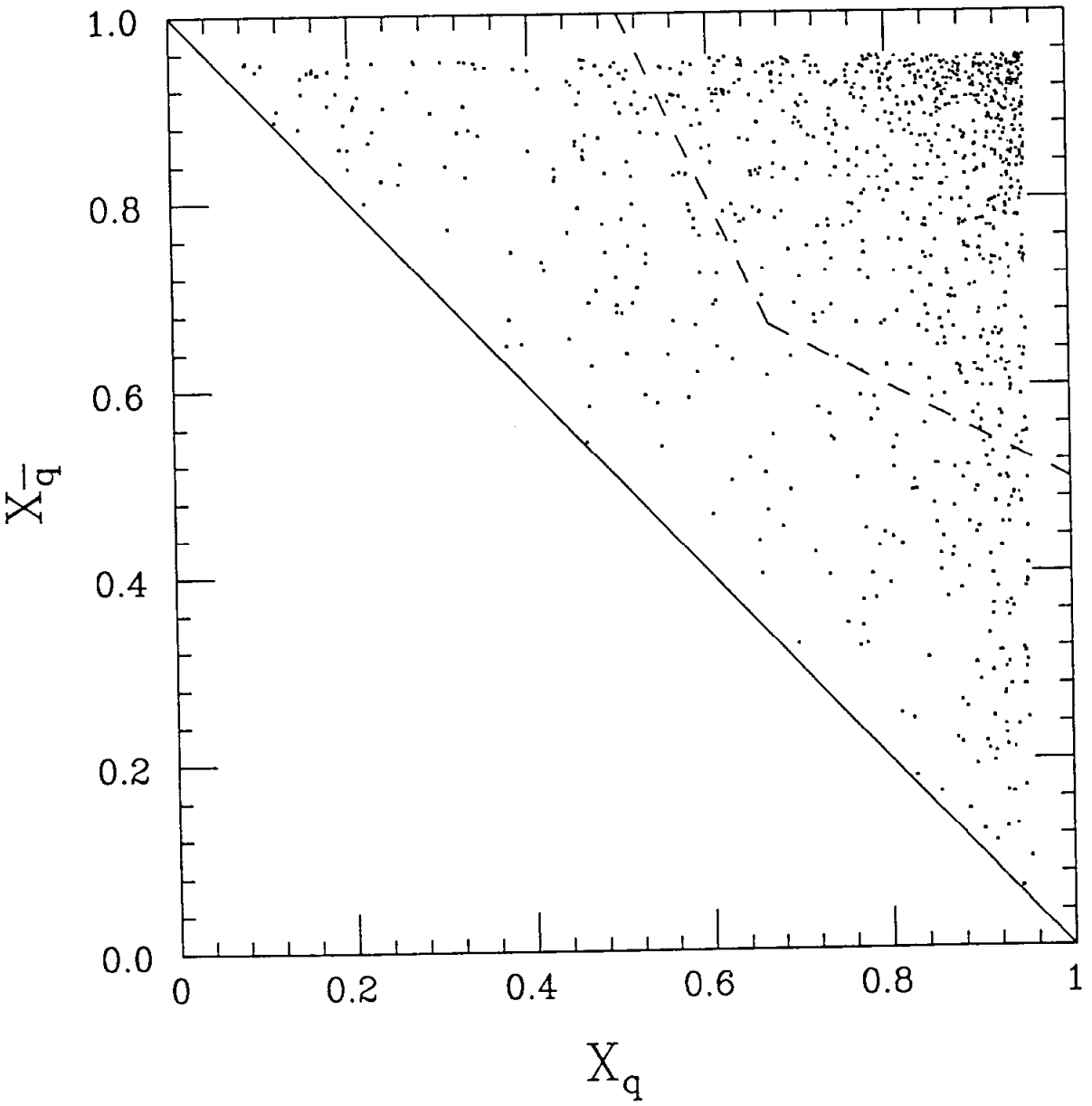

Figure 6.4. Scatterplot of $d^2\sigma/dx_q dx_{\bar{q}}$ to $O(\alpha_s^1)$. The kinematically allowed area of x_q and $x_{\bar{q}}$ in the figure is given by the constraint $x_q + x_{\bar{q}} > 1$ (solid line). The area that contributes good parton skeletons, in the sense of the energy asymmetry, is given by the constraint $2 - x_q - x_{\bar{q}} < \min(x_q, x_{\bar{q}})$ (dashed line). The points shown are for $x_q > .95$ and $x_{\bar{q}} > .95$.

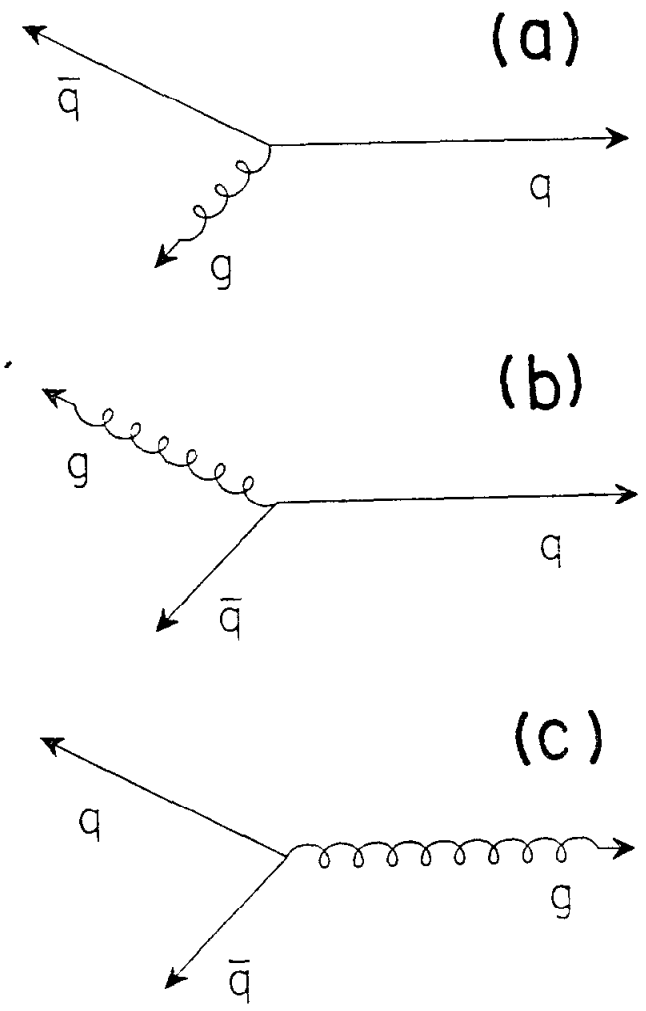

Figure 6.5. Three orderings of the parton energies in $O(\alpha_s^1)$. The first skeleton (a) represents the desired configuration for analyzing energy flow asymmetry: the gluon is the least energetic parton. The other two skeletons represent undesirable configurations where (b) the gluon is harder than the associated quark, or (c) the gluon is the most energetic parton.

Most of these events come from topologies similar to that of Fig. 6.5a, but the emitted gluon tends to be very soft. These events result in very little asymmetry, and dilute the asymmetry from the more *3-jet*-like events. Making the $hE_{\perp}^{in}$ cut at a higher value enriches the event sample with parton topologies similar to those of Fig. 6.5b and c. This again dilutes the desired asymmetry, while the poor acceptance reduces the statistical significance of the result. The final placement of the $hE_{\perp}^{in}$ cut between the above two extremes was placed so as to maximize the asymmetry seen in the data.

6.2 Energy Flow Around the Event Plane

The energy flow around the event plane is studied by projecting each two-ended calorimeter hit vector onto the event plane. By projection onto the event plane, the effect of uncertainties in the event plane orientation are minimized. Figure 6.6 shows the energy flow around the event plane for the data. The narrow peak at 0° is associated with the rather small $hE_{\perp}$ fragmentation of the lone quark. Also apparent is a broad peak around ±180° associated with the larger $hE_{\perp}$ fragmentation of the quark and gluon system. The 3-lobe structure seen in the energy flow should not be interpreted as direct evidence of hard gluon bremsstrahlung. By a suitable choice of fragmentation Monte Carlo parameters, $O(\alpha_s^0)$ events can show a similar structure.[70] The interesting feature here is the asymmetry observed around the region ±90°. The region we associate with the area between the gluon and hard quark jet (near +90°) has more energy then the region we associate with the area between the two quark jets (near −90°). This asymmetry is counter to the asymmetry expected from the phase space imposed by the standard orientation.

We repeat this procedure on Monte Carlo data samples. The energy flow expected from IJM fragmentation (with energy-momentum according to the Ali scheme, and $g \rightarrow q\bar{q}$) is shown in Fig. 6.7a, with the data shown for comparison. The energy flow for STR fragmentation is shown in Fig. 6.7b. The energy flow for Webber's implementation of QCD showers and clustering is shown in Fig. 6.7c. The Webber Monte Carlo is very different from the IJM and STR models. The Webber scheme is to generate partons using leading-log QCD branching, followed by the clustering of partons into color singlets. The cluster decay results in the primary hadrons. This mechanism is detailed in Appendix A.

With regard to gross features of the energy flow, the data and Monte Carlos are

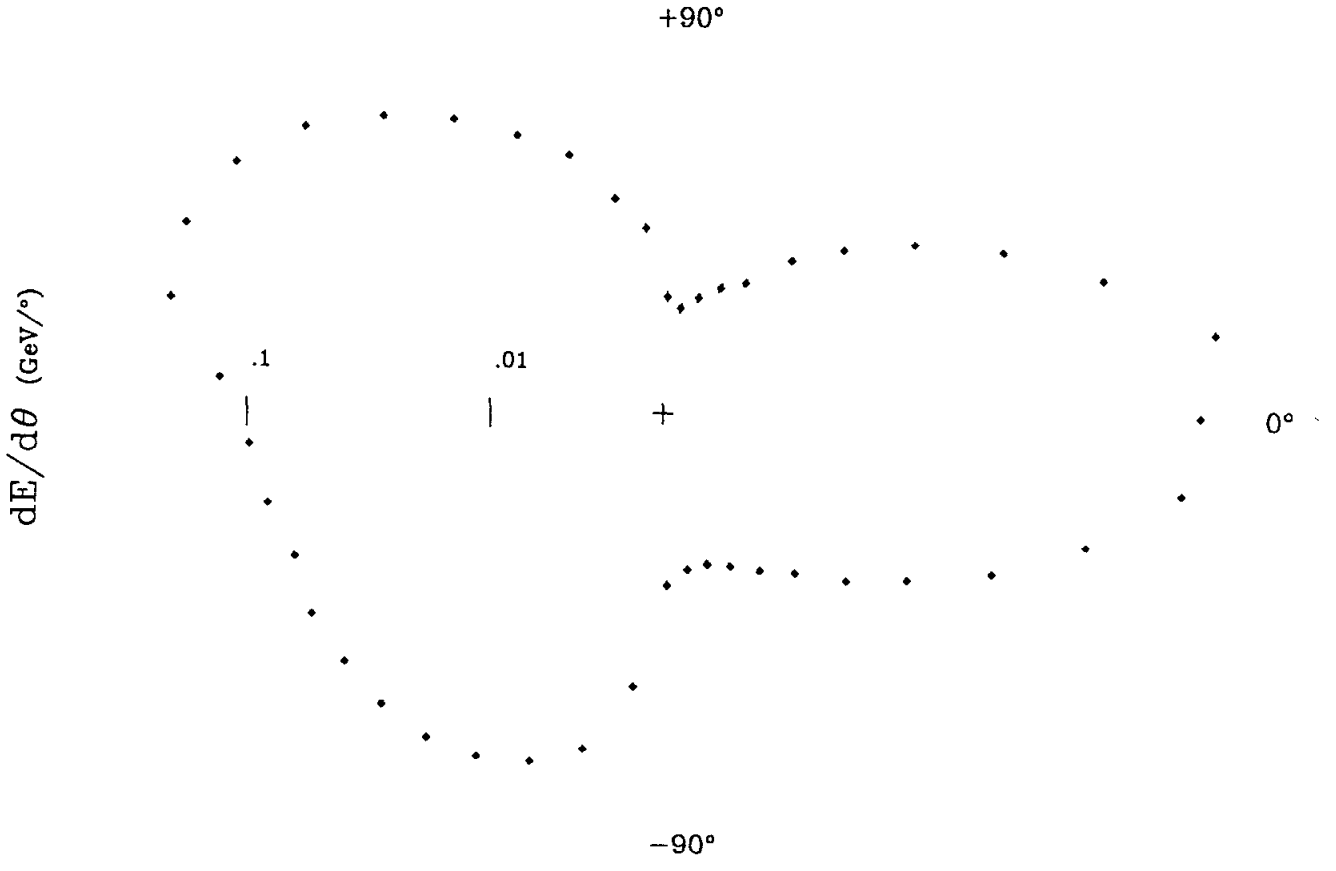

Figure 6.6. Event plane energy flow for the data. Note the log-polar scale.

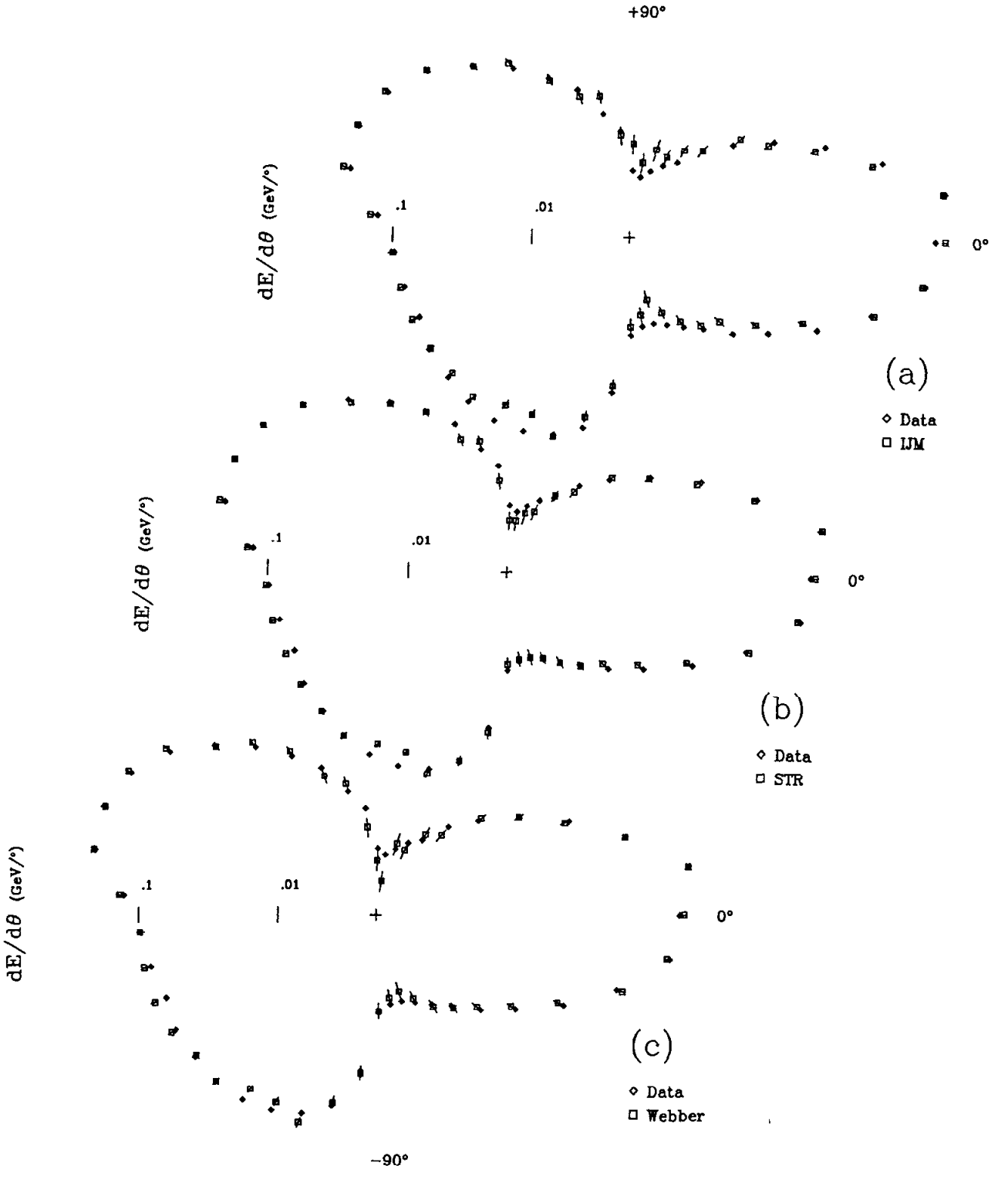

Figure 6.7. Energy flow for the data and fragmentation models: (a) IJM fragmentation with energy-momentum according to the Ali scheme with $g \rightarrow q\bar{q}$, (b) STR fragmentation, (c) Webber cluster model. The asymmetry seen in the data near $\pm 90°$ is modeled by the STR and Webber fragmentation models. The IJM model shows no asymmetry.

similar. However, the asymmetry observed near $\pm 90^\circ$ is somewhat different between the different fragmentation models and the data. The difference in asymmetry between STR fragmentation and the data is very small. There is a very slightly greater asymmetry seen in the STR energy flow as compared to the data, though the overall agreement between the data and STR energy flow appears quite good. The asymmetry seen in IJM energy flow is very small and is opposite in sign to that seen in the data; the area we associate with the area between the gluon and hard quark (around -90°) for IJM fragmentation is depleted in energy relative to the data, and the region we associate with the area between the two quarks for IJM fragmentation shows an energy enhancement relative to the data. The asymmetry seen in the Webber energy flow is slightly larger than that observed in the data, and there is also a slightly greater energy depletion in the $+90^\circ$ and -90° regions then as compared to the data.

6.3 Fits to the Model Hypotheses

It is desirable to determine the goodness of fit of the energy flow of the data to the energy flow predicted by the fragmentation models. There are two sources of systematic errors that must be addressed in the fit procedure.

The first systematic error arises from the MAC energy resolution for small particle energy. The energy deposited in the $\pm 90^\circ$ regions comes mostly from low energy particles. Recall that Fig. 2.4 shows the energy of soft particles ($< 1\,\mathrm{GeV}$) is poorly resolved in the MAC detector. Also, the Monte Carlo estimates for the shower energy in the $\pm 90^\circ$ regions strongly depend on subtle details of the modeling of the these soft showers.

The second systematic error stems from a detail of the parton generation in the Webber Monte Carlo. Cluster Monte Carlos, by generating parton cascades according to leading-log QCD, tend to underestimate the number of hard wide angle gluons radiated. This can result in underestimating the energy flow in both of the $\pm 90^\circ$ regions between the jets.

Both of these systematic errors are addressed in the following argument. While its clear that modeling errors and energy resolution make absolute predictions of the energy flow unreliable, these systematics tend to effect the $\pm 90^\circ$ regions to the same extent. These systematics can be controlled by self-normalizing the energy flow. The region $0^\circ < \theta < 180^\circ$ of Fig. 6.6 is divided by the region $-180^\circ < \theta < 0^\circ$. This approximately corresponds to splitting the $q\bar{q}g$ event plane into two halves

along the thrust axis, then dividing the half containing the softer quark by the half containing the gluon. This procedure results in distributions insensitive to the symmetric systematics and isolates the hadronization asymmetry differences between models from the details of hard parton generation. We define the divided energy flow through the relation

$$D(\theta) = \frac{dE(\theta)/d\theta}{dE(-\theta)/d\theta} \quad .$$

Carrying out this scheme of dividing one side of the event plane of Fig. 6.7 by the other side results in the following figures: Figure 6.8a is the divided energy flow of the data and STR fragmentation. Figure 6.9b is the divided energy flow of the data and IJM fragmentation. Figure 6.10c is the divided energy flow of the data and the Webber implementation of QCD showers with soft gluon interference.

6.4 Discussion and Conclusions

For the case of IJM fragmentation, we expect the thin jet to fragment in a completely symmetric way around the thin jet axis. This effect is seen in Fig. 6.9 as a flat region where $D(\theta) \approx 1$ between 0° and 90°. The flat $D(\theta)$ behavior seen for IJM fragmentation should be compared with the data. The falling value of $D(\theta)$ as θ goes from 0° to 90° indicates that the effects of gluon fragmentation in the fat jet hemisphere extends even out to the thin jet hemisphere. We see this effect as an energy enhancement on the gluon side of the thin jet. The asymmetry around the thin jet ($0° \rightarrow 90°$) is now also apparent in the STR (Fig. 6.9) and the and Webber (Fig. 6.10) models. It's apparent from looking at Figs. 6.8-6.10 that the thin jet asymmetry is described well by STR and Webber models, while IJM fragmentation provides a poor description. This assertion is quantified in the next section.

6.4.1 Goodness of Fit

We now proceed with reporting the goodness of fit of the data to IJM, STR and Webber fragmentation hypotheses. The θ region 0° to 90° corresponding to the thin jet will be used in the fit. The resulting χ^2 are given in Table 6.1. The fit of the data to the IJM hypothesis is very poor. The fits to the STR and Webber fragmentation hypotheses are rather good.

These fits of the thin jet energy flow asymmetry are consistent with the χ^2 fits of α_s and σ_q to the full $hE_{\perp}^{in}(\text{fat})$ distribution. The fit using the STR hypothesis

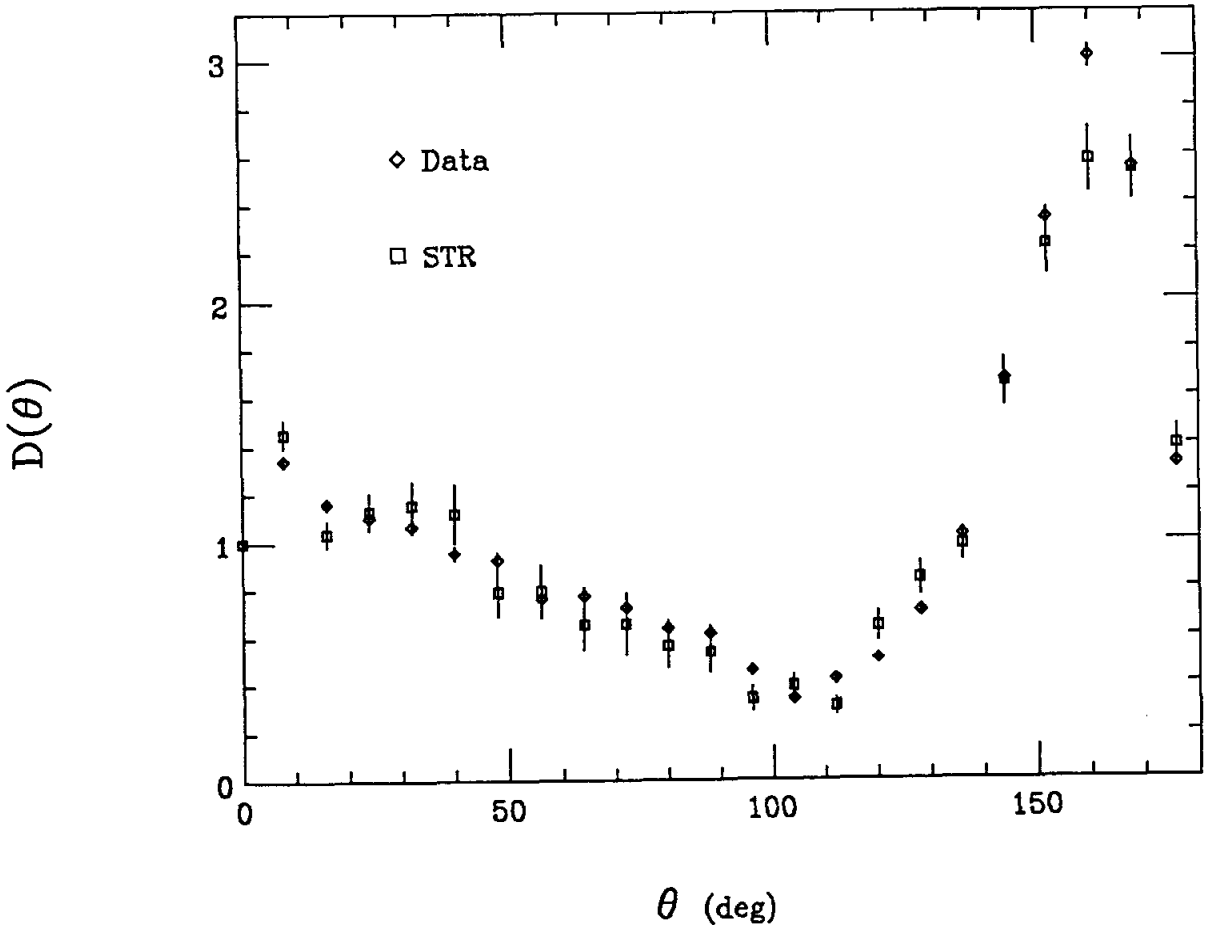

Figure 6.8. $D(\theta)$ for the data and STR fragmentation. The region $0° < \theta < 180°$ of Fig. 6.6 is divided by the region $-180° < \theta < 0°$. This approximately corresponds to splitting the $q\bar{q}g$ event plane into two halves along the thrust axis, then dividing the half containing the quark by the half containing the gluon. A falling slope on the portion of the curve ($0° \rightarrow 90°$) corresponding to the thin jet is seen in the data and the prediction of the STR model.

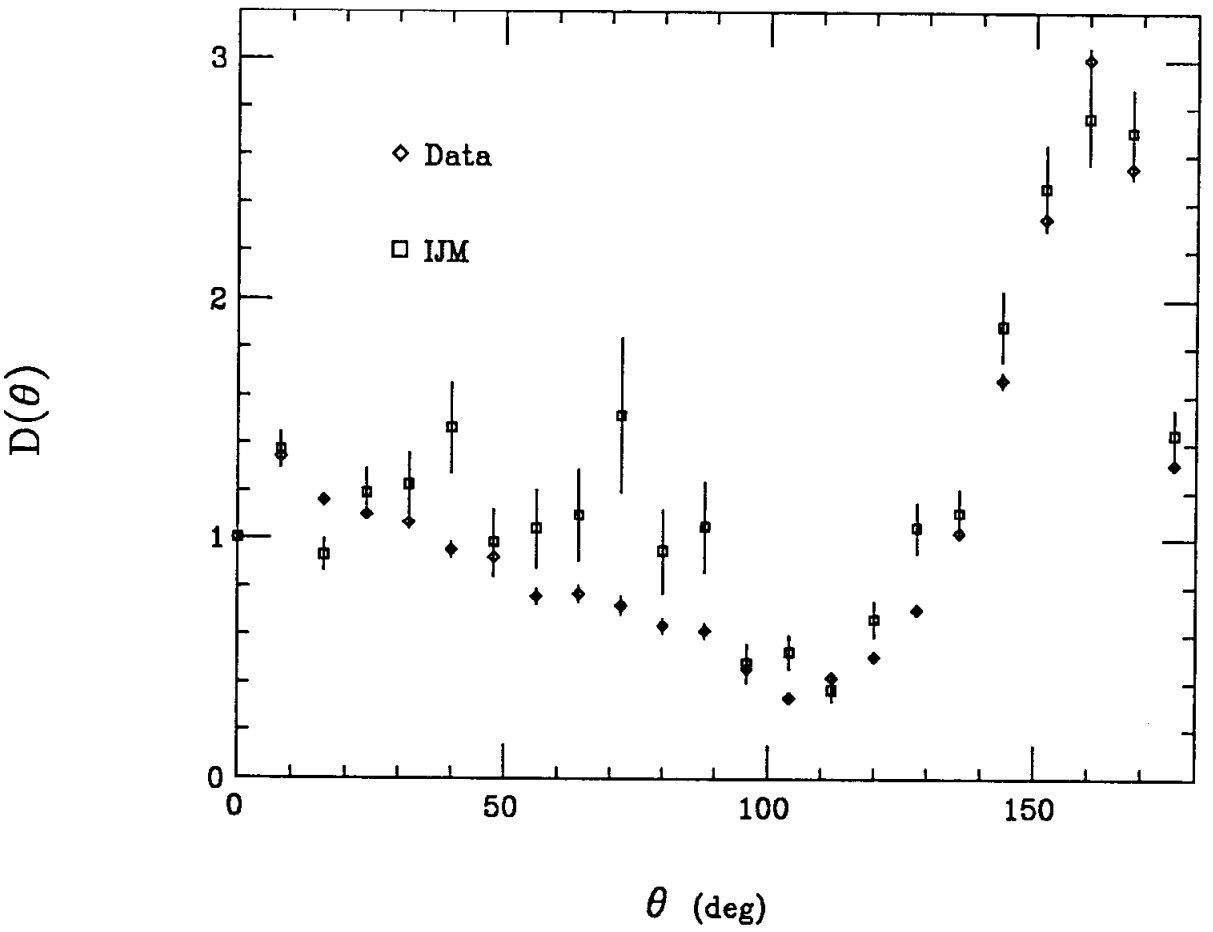

Figure 6.9. $D(\theta)$ for the data and IJM fragmentation. The region $0° < \theta < 180°$ of Fig. 6.6 is divided by the region $-180° < \theta < 0°$. This approximately corresponds to splitting the $q\bar{q}g$ event plane into two halves along the thrust axis, then dividing the half containing the quark by the half containing the gluon. A falling slope on the portion of the curve ($0° \rightarrow 90°$) corresponding to the thin jet is seen in the data but not seen in the prediction of the IJM model.

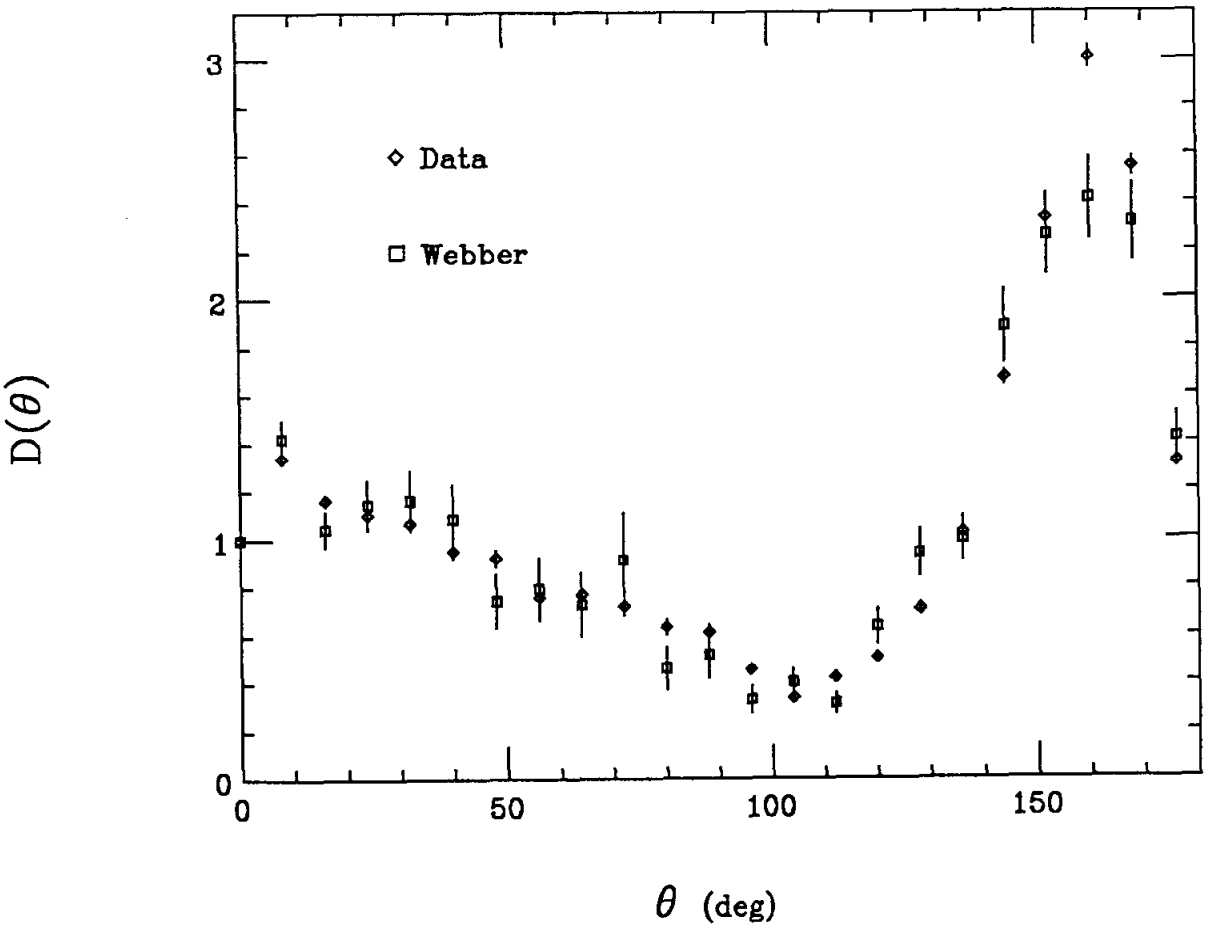

Figure 6.10. $D(\theta)$ for the data and Webber model. The region $0° < \theta < 180°$ of Fig. 6.6 is divided by the region $-180° < \theta < 0°$. This approximately corresponds to splitting the $q\bar{q}g$ event plane into two halves along the thrust axis, then dividing the half containing the quark by the half containing the gluon. A falling slope on the portion of the curve ($0° \rightarrow 90°$), corresponding to the thin jet, is seen in the data and from the prediction of the Webber model.

Table 6.1. χ^2 from fitting the data to IJM, STR and Webber fragmentation hypotheses for the θ interval 0° to 90° corresponding to the thin jet. The IJM fragmentation incorporates energy-momentum conservation with the Ali scheme, and Altarelli-Parisi splitting $g \rightarrow q\bar{q}$. The IJM model provides a poor description of the energy flow asymmetry around the thin jet.

model hypothesis	χ^2	DOF
STR	15.86	12
IJM	42.58	12
Webber	12.86	12

gave $\chi^2 = 25.2$, while fits using the various IJM hypotheses resulted in $\chi^2 > 36$ for 26 DOF. It should be noted that the previous MAC energy-energy correlation study[37] resulted in fits of the data to STR and several implementations of IJM fragmentation. The fits to the STR and a representative IJM scheme used in the previous study are shown in Table 6.2. The fit to the STR hypothesis is quite good. The IJM hypothesis provides a very poor fit.

Table 6.2. MAC energy-energy correlation fits of the data to the STR and IJM fragmentation with energy-momentum conservation with the Ali scheme, and Altarelli-Parisi splitting $g \rightarrow q\bar{q}$. These fits agree with the results of the present analysis, shown in Table 6.1.

model hypothesis	χ^2	DOF
STR	35	47
IJM	136	47

6.4.2 Interpretation

We feel that the proper interpretation of this phenomenon is that the mechanism of hadronization is a coherent phenomenon that involves all the color charges in the event. For the case of the string, the coherent hadronization occurs through strings ending at color charges. The QCD shower models incorporate this coherence by including effects of soft gluon interference in the QCD branching.

This is best seen through the following semi-classical argument. Gluons with large energy have short wavelength and can resolve individual color charges within a jet. A very soft gluon, on the other hand, sees a color charge as some coherent sum of individual color charges in the jets. This coherence results in interference that has strong effects on the soft gluon component in jets. A more complete discussion of this phenomenon is given in Appendix A. We do not see evidence that any one coherence mechanism, strings or soft gluon interference, is favored over the other by the data. We prefer instead to make the point that the present result serves to constrain any model that attempts to describe hadronization; such models must incorporate coherent fragmentation in order to agree with the data.

6.4.3 Comparison with Other Experiments

Since energy flow was proposed as a technique for the testing of QCD predictions,[71] numerous studies using e^+e^-,[72,73] PP[74] and deep inelastic[75] interactions have reported on the a 3-lobe energy flow structure as evidence for gluon bremsstrahlung. As we mentioned earlier, a 3-lobe structure may be generated by *2-jet* phase space and by certain exotic mechanisms unrelated to hard gluon bremsstrahlung.[76] Although other analysis tools eclipsed energy flow as a means of examining *3-jet* events, the JADE Collaboration[77–79] first applied the energy flow technique to the task of detecting subtle differences between the various hadronization models. The JADE results were later confirmed by the TPC Collaboration,[80] who examined particle flow around the event plane. As discussed in Chapt. 1, we regard particle flow as a less robust indicator of the event color flow, although in practice, both energy and particle flow give similar qualitative results. The results of our study agree with the results of the JADE and TPC Collaborations. All three studies observe asymmetry in the particle or energy flow. There is agreement on the finding that IJM fragmentation schemes deposit too much energy or particles in the region associated with the area between the q and $\bar{q}$ jet. Also in agreement, are observations that the STR model provides a good fit to the energy flow or particle flow around the whole of the event plane, including the regions between the primary partons. The TPC study finds that the Webber Monte Carlo over-predicts the particle density in the region between jets. They report that the particle density between jets is especially sensitive to the value of M^{max}, the maximum cluster mass parameter. However, JADE reports that the observed particle flow between jets is described well by the Webber Monte Carlo. This

MAC study and the JADE study find that the Webber Monte Carlo yields accurate predictions for the energy flow between jets. We note that absolute predictions of energy or particle flow from the Webber Monte Carlo are necessarily approximate owing to the leading-log scheme of parton generation. However, all three studies find the Webber model (QCD showers incorporating angle ordering) predicts the observed ratios of the energy flow (MAC, JADE) or particle flow (JADE, TPC).

7. Overall Conclusions

This study resulted in fits of α_s to STR and several varieties of IJM fragmentation yielding

$$\alpha_s \approx \begin{cases} 0.12 & (IJM) \\ 0.17 & (STR) \end{cases} .$$

The fits used $O(\alpha_s^2)$ QCD matrix elements calculated using the $\overline{MS}$ renormalization scheme. These α_s values as well as the model dependence are consistent with earlier MAC energy-energy correlation studies, and are consistent with almost all the other related studies at PEP and PETRA using shape, cluster and energy-energy correlation methods. The α_s value fitted with the STR hypothesis is consistent with α_s derived from the MAC R measurement, while the α_s value fitted with the IJM hypothesis is slightly inconsistent with R. The difference between $\alpha_s(IJM)$ and $\alpha_s(R)$ corresponds to ΔR of $\approx 1/10$. The α_s value fitted with the IJM hypothesis is consistent with results from onia, 2γ and deep inelastic scattering experiments; α_s fitted with the STR hypothesis is inconsistent with these experiments, however.

The α_s situation is admittedly chaotic. α_s derived from R is big. α_s from onia, 2γ and deep inelastic experiments is small. α_s from the PEP and PETRA shape, cluster and energy-energy correlations can be big (STR) or small (IJM), depending on the fragmentation model hypothesis. Its interesting to note that although α_s values measured via R, and α_s values derived via onia, 2γ and deep inelastic scattering measurements are only minimally dependent on the fragmentation model used, the difference between the resultant values of α_s are very large. So, the fragmentation models aren't entirely to blame for the situation.

As yet, the cluster models haven't been used in fits of α_s. This is due to the absence of exact $O(\alpha_s^2)$ matrix elements for the primary parton generation. Incorporating these matrix elements and preserving the soft gluon interference is non-trivial. Since gluon bremsstrahlung has a collinear singularity, the typical gluon is emitted at a very small angle. If angle ordering is applied to such a skeleton, subsequent leading-log evolution generates partons at even smaller angles. The

IR cutoff on the exact matrix elements thus has a critical effect on subsequent branchings. This problem is not insurmountable, however, and is a logical next step in cluster Monte Carlo development.

The size of the current PEP and PETRA databases have made the statistical uncertainty in α_s measurements small relative to the systematic uncertainty in the QCD predictions. Future advances in determining α_s therefore depend on improving the quality of the theoretical predictions. The recent work of Gottschalk and Shatz on the effects of different jet dressing schemes and subleading corrections to the $O(\alpha_s^2)$ cross sections is an important new theoretical development.

This analysis has also examined details of the energy flow projected onto the event plane. An energy depletion is observed in the region associated with the energy valley between the two quarks. A resulting energy asymmetry around the thin jet is seen in the data, as well as in the predictions of STR and Webber fragmentation models. An asymmetry around the thin jet is missing from predictions of the IJM models. These conclusions are consistent with results from the JADE and TPC collaborations.

We attribute this asymmetry to coherence effects in the hadronization. The STR model achieves this coherence via strings stretched between color charges. The Webber model generates coherence by including the effects of soft gluon interference.

One should avoid, however, the temptation to label the STR or Webber model as "right", and the IJM models as "wrong". The fragmentation models are based on phenomenological prescriptions that take the place of QCD in the low Q^2 domain. The fact that the STR model predicts the energy flow asymmetry seen in the data doesn't necessarily mean that the STR value of α_s is more valid then an IJM value of α_s. In fact, though the STR model predicts the observed energy flow asymmetry, the value of α_s extracted using the STR hypothesis is inconsistent with results from onia, 2γ and deep inelastic scattering experiments. That these rather different experiments are in agreement, and yield α_s values with only minimal dependence on fragmentation Monte Carlos, gives an α_s value around .12 considerable credibility. The IJM models predict none of the required energy flow asymmetry, yet fits of α_s with the IJM hypothesis are consistent with the onia, 2γ and deep inelastic scattering experiments. The large value of the second order α_s using the STR hypothesis should therefore be considered an outstanding problem for a model that otherwise describes the data quite well.

The future of QCD studies in e^+e^- annihilation is heading in the direction of

studying refinements of the fragmentation models. There is an advantage in going to higher energy, in that the fraction of time spent in the non-perturbative stage of the event evolution is reduced. Problems arise in that higher energies require higher order QCD calculations for generation of the primary partons. Calculations of $O(\alpha_s^3)$ are unlikely to be forthcoming in the near future. It seems that leading-log QCD parton generation, with some sub-leading corrections, will be at the heart of future hadronization Monte Carlos. At hadron colliders, the ambiguities from the extra complication of initial state QCD radiation has yet to be fully resolved in the showering formalism.

Barring a theoretical breakthrough, the long term outlook for QCD studies still calls for extensive use of phenomenological models. We, as experimentalists, look forward to the day when non-perturbative predictions can be extracted from QCD, rendering obsolete our dependence on phenomenological prescriptions of hadronization.

Appendix A. The Basis Of Monte Carlo Predicting

The complete Monte Carlo simulation of $e^+e^- \rightarrow hadrons$ proceeds in a four step process:

- Generation of two primary quarks and perhaps a radiative photon according to QED, including virtual Z^0 exchange.
- Production of gluons (and perhaps additional quarks) from the primary quarks either (a) exactly to finite order in α_s, or (b) approximately with leading-log QCD branching;
- Generation of primary hadrons;
- Decay of unstable hadrons.

A.1 QED Parton Generation

The Berends-Kleiss-Jadach Monte Carlo[81] is modified to generate $q\bar{q}(\gamma)$ events including QED effects to $O(\alpha^3)$, along with virtual Z^0 exchange. The $q\bar{q}(\gamma)$ generator includes the diagrams given in Fig. A.1. The modifications include removing final state radiation and incorporating the constituent quark mass, charge and weak isospin. The IR cutoff is set at $E_\gamma > 0.01E_{beam}$, and the maximum photon energy is set at the kinematic limit of $E_\gamma/E_{beam} < 1 - (M_q/E_{beam})^2$.

A.2 QCD Parton Generation

There are presently two schemes available for adding quarks and gluons to the primary quark pair. One scheme calls for using the exact matrix elements of $e^+e^- \rightarrow quarks + gluons$ to finite order in α_s. There are exact calculations available to $O(\alpha_s^2)$. Extending these calculations to higher order in the near future seems unlikely.

The second scheme is to use the leading-log formalism to perform iterative parton branching starting with the primary quark pair. This has the advantage

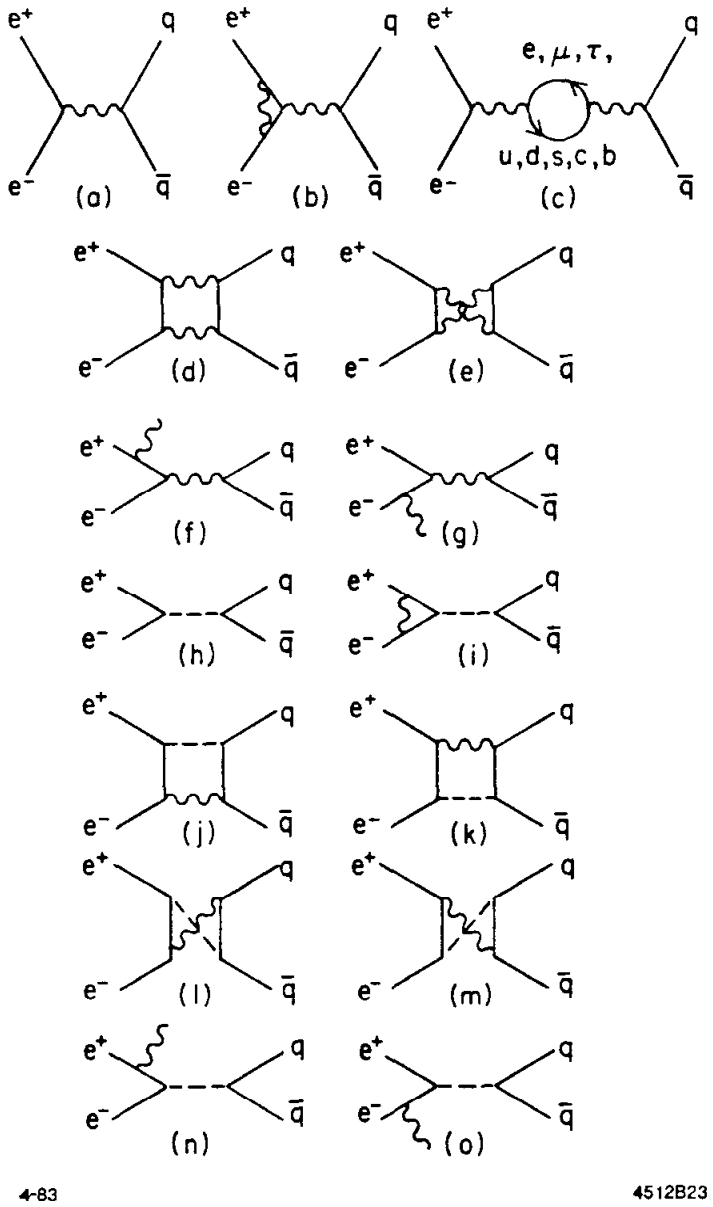

Figure A.1. QED and weak diagrams included in the modified Berends-Kleiss-Jadach $e^+e^- \to q\bar{q}(\gamma)$ event generator.

of incorporating, in an approximate sense, the effects of higher order QCD. The disadvantage is that any large Q^2 branchings are underestimated.

The IJM and STR models use as input the partons generated from the exact $O(\alpha_s^2)$ QCD matrix elements. The Cluster models employ leading-log iterative branching as an integral part of the fragmentation algorithm. Both models could, in principle, be coupled to a leading-log parton generating scheme. However, the approximate nature of the leading-log branching probably makes even the exact $O(\alpha_s^1)$ matrix element more attractive for generating partons at $\sqrt{s}$ of 29 GeV that reproduce global event shapes. With reasonable input parameters, the leading-log and exact schemes both predict approximately the same number of partons at $\sqrt{s}$ of 29 GeV. It is anticipated that at higher energies of $O(100\,\text{GeV})$, the leading-log formalism will be absolutely essential as the number of resolvable jets is expected to be greater than the current ceiling of four available with $O(\alpha_s^2)$ calculations.

A.2.1 Exact Calculation to Finite Order in α_s

If a radiative photon was generated, the previously produced quark and anti-quark are boosted to their center-of-mass frame. Next, these quarks will have gluons and additional quarks added perturbatively to the $q\bar{q}$ system according to the appropriate *2*, *3* or *4-jet* matrix elements.[82] The QCD graphs incorporated into the calculation are shown in Fig. A.2. As the *3* and *4-jet* matrix elements display IR and collinear singularities, a cutoff is employed on the minimum scaled invariant mass, $Y_{min} = M_{ij}^2/s$, between any two colored partons i and j. For each event, Y_{min} is set to the minimum value consistent with:

- The $3+4$*-jet* probability is ≤ 1;
- $d^2\sigma/d\vec{k}_q d\vec{k}_{\bar{q}} \geq 0$ over kinematically allowed values of $\vec{k}_q$ and $\vec{k}_{\bar{q}}$.

A random variable then determines whether 0, 1 or 2 gluons (or perhaps additional quarks) are radiated according to the appropriate $O(\alpha_s^2)$ matrix elements,[82]including $O(\alpha_s^2)$ QCD virtual corrections.[a] This implementation of

[a] There is some controversy as to the $O(\alpha_s^2)$ $e^+e^- \rightarrow quarks + gluons$ matrix element calculation. Gottschalk and Schatz have calculated the $O(\alpha_s^2)$ *3-jet* cross section, including terms subleading in the resolution parameter,[48,49]and found that their result differed from earlier results lacking these terms.[83,84] Gottschalk and Shatz demonstrate that their *3-jet* calculation can result in a smaller fit to α_s, though they caution us against direct comparison with experiment as being far too naive.[50]

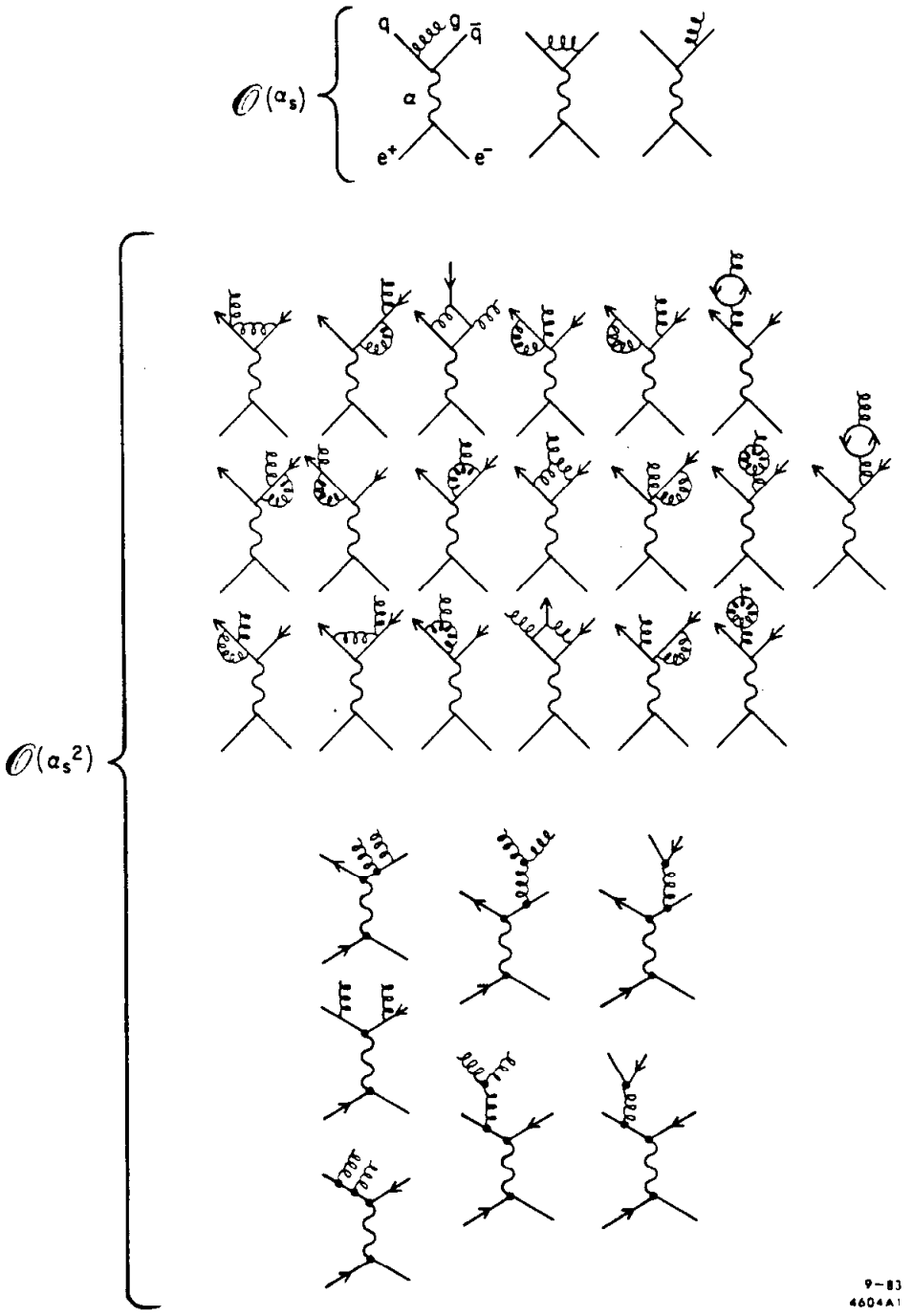

Figure A.2. QCD graphs included in the $e^+e^- \rightarrow quarks + gluons$ matrix elements.

the QCD matrix elements is essentially that provided by the Lund Monte Carlo program.[85] Note that the value of Y_{min} will depend on the particular value of α_s used in the matrix elements. Typical values of Y_{min} and the corresponding parton multiplicity distributions are shown in Table A.1 for various values of α_s.

Table A.1. Parton multiplicity and IR cutoff for various values of α_s, generated by the $O(\alpha_s^2)$ $e^+e^- \rightarrow quarks + gluons$ Monte Carlo.

α_s	% of events			Y_{min}
	2-jet	*3-jet*	*4-jet*	
.10	26	62	12	.005
.15	5	78	16	.010
.20	5	85	10	.020

A.2.2 Leading-Log QCD Branching

The Monte Carlos that generate partons with an exact QCD matrix element to some finite order in α_s rely on phenomenological prescriptions for the fragmentation of the partons down to the QCD scale Q_0. This means that the least understood part of the theory is responsible for almost all of the hadronization. The method of QCD branching allows partons to be generated perturbatively down to the scale Q_0, consistent with $\alpha_s(Q_0^2)/\pi < 1$. The disadvantage is that the approximations inherent in the QCD branching may not be reasonable at the PEP energy scale.

A.2.2.1 Conventional QCD Branching

If we start with the arbitrary (n)-parton state with cross section σ_n, shown in Fig. A.3a, the cross section to evolve into the $(n+1)$-parton state, shown in Fig. A.3b is given as[20,86]

$$d^2\sigma_{n+1} = \sigma_n \frac{\alpha_s[z(1-z)Q^2]}{2\pi Q^2} P(z) \frac{\Delta_s(Q^2_{max})}{\Delta_s(Q^2)} dQ^2 dz$$

where z is the $E+|P_z|$ fraction carried off by the gluon relative to the initial off-shell quark, $z(1-z)Q^2$ is the argument of α_s, $P(z)$ is an Altarelli-Parisi splitting function corresponding to the particular type of branching, and $\Delta_s(Q^2)$ is a Sudakov form factor that may be interpreted as the probability for a quark with mass Q^2 to emit only very soft gluons in the quark branching down to the cutoff mass Q_0.[87] The Sudakov formalism incorporates sub-leading corrections to the QCD branching. The resultant Q^2 is bounded from above by the Q^2 of the parent parton, denoted Q^2_{max},[b] and below by Q^2_0, the QCD cutoff scale. In practice, the cutoff mass must be greater than $2m_u$ to allow for subsequent decay of partons into clusters massive enough to decay into hadrons. Up to uniform angular distributions, Q^2 and z completely define the branching kinematics of the decay vertex.

A.2.2.2 QCD Branching with Soft Gluon Interference

The outgoing particles at each vertex define an opening angle variable $\xi \equiv \vec{q}_i \cdot \vec{q}_j / E_i E_j$, with i and j labeling the two outgoing partons. In the limit that the emitted gluons are very soft, interference effects occur that severely reduce the allowed phase space available for branching.[88] The remaining phase space is that for which the branching angles ξ continuously decrease. For example, in the state shown in Fig. A.3c, the angle ordering is required to be $\xi_2, \xi_3 < \xi_1 < \xi_0$. The main effect of the angle ordering is to suppress the production of gluons in the soft branchings. B. Webber pictures this as a coherence effect:[89] short wavelength gluons resolve the individual color charges in a jet. However, long wavelength gluons only see an overall reduced jet color charge. In terms of the angle variable ξ, the evolution cross section becomes

$$d^2\sigma_{n+1} = \sigma_n \frac{\alpha_s[2z^2(1-z^2)E^2\xi]}{2\pi\xi} P(z) \frac{\Delta_s(\xi_{max})}{\Delta_s(\xi)} \theta(\xi_{max}-\xi)\theta(\xi-\xi_{min}) d\xi dz \quad ,$$

with z now the energy fraction.

The application of this formalism to a Monte Carlo first requires boosting the two primary partons into the frame where $\xi_0 = \pi/2$. Each subsequent branching is generated from the above distribution, which involves assigning an energy fraction and decay angle at each vertex. When branching terminates at the IR cutoff Q_0, the four-momenta of the resultant final state partons can be computed. The subsequent decay of these partons into hadrons is described in a later section.

---

[b] For the primary partons, $Q^2_{max} = s$.

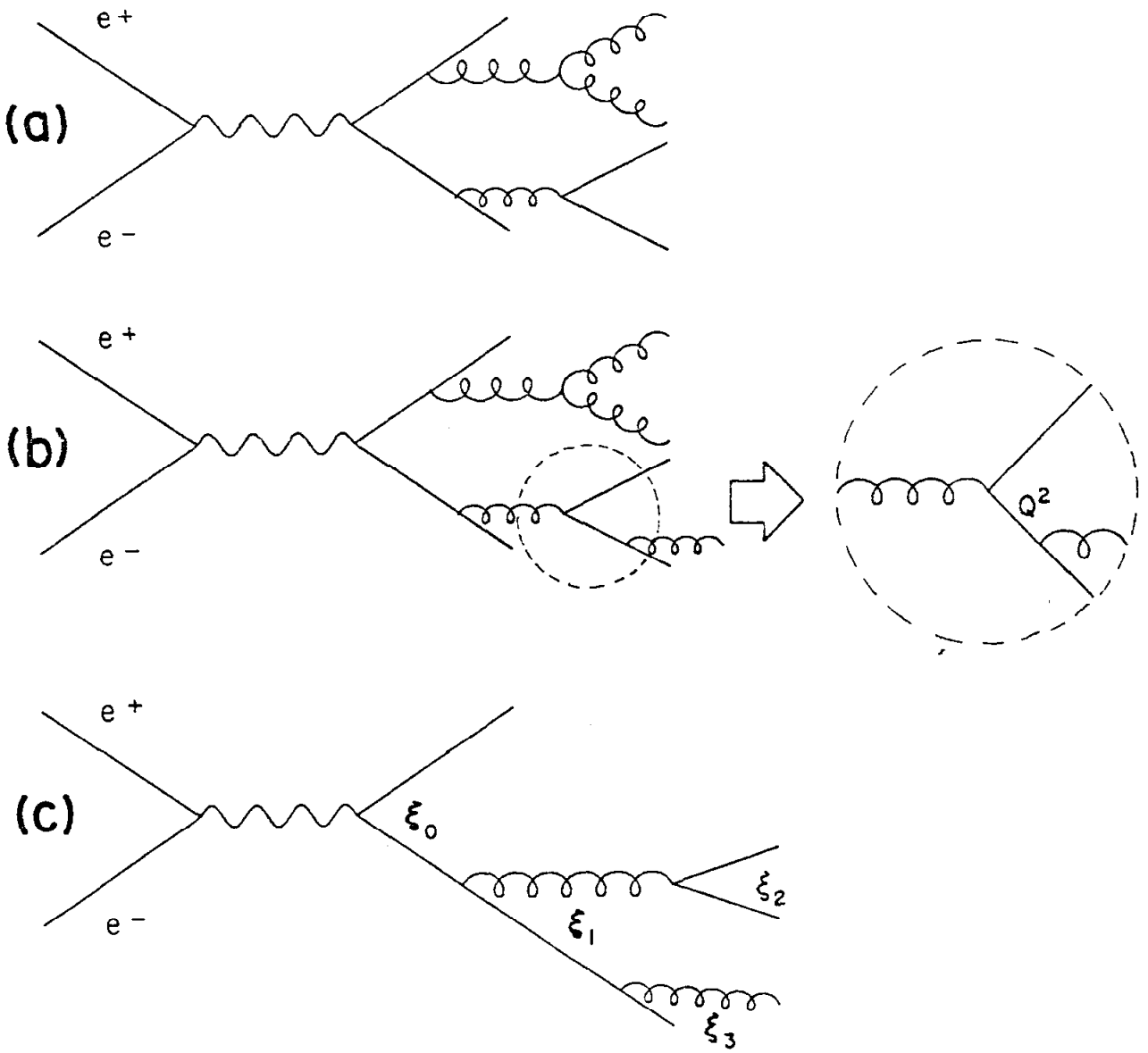

Figure A.3. Snapshots of QCD branching showing (a) an arbitrary (n)-parton state, (b) the ($n+1$)-parton state evolving from (a), (c) the labeling of the vertices with the angle variable. When soft gluon interference is incorporated into branching, the allowed phase space is that for which the branching angles continuously decrease.

A.3 Non-Perturbative Dressing of Primary Quarks and Gluons

The partons from the perturbative parton generating phase are used as input to the non-perturbative fragmentation models. The IJM and STR models produce a cascade of hadrons, with approximate time ordering by rapidity (high to low in the IJM, and low to high in the STR). The IJM and STR models both generate transverse momentum for the jets in a similar way. When the quarks are generated during fragmentation, each quark carries $P_\perp$ according to the distribution:

$$P_q(P_\perp) = \frac{1}{2\sigma_q^2\pi} e^{-P_\perp^2/2\sigma_q^2}$$

The parameter σ_q represents the average $P_\perp$ carried by each fragmenting quark. The value of σ_q is determined by a fit to the data and depends somewhat on the fragmentation model and value of α_s used in the fit. In fact, there is a difference in definition between the σ_q for IJM and STR fragmentation. For IJM fragmentation, the $P_\perp$ is relative to the primary parton direction. For STR fragmentation, the primary partons have been replaced by color strings; the relevant axis for $P_\perp$ is the string axis. The Cluster models group partons into color singlet clusters according to the flavor ordering in the event. These primary clusters then decay into primary hadrons.

A.3.1 Incoherent Jet Models

The IJM parametrization of the properties of quark jets, as developed by Field and Feynman,[90] features quarks that fragment completely independently from each other. There are several schemes developed later for the fragmentation of gluon jets. The simplest is to turn the gluon into a quark of random flavor with equivalent momentum. A more reasonable approach is to split the gluon into a $q\bar{q}$ pair, where the fraction z of the gluon momentum carried by the quark is given by an Altarelli and Parisi splitting function[91] $P_{g\to q\bar{q}}(z)$

$$P_{g\to q\bar{q}}(z) = \{z^2 + (1-z)^2\}/2 \quad .$$

Gluons jets resulting from the Altarelli and Parisi splitting formalism have a softer spectrum then gluon jets resulting from the naive $g \to q$ scheme. The quarks resulting from either of the gluon decay methods then decay as normal quarks.

During quark fragmentation, the parent quark pulls a quark pair out of the sea: $q_i \rightarrow q_i' q_j \bar{q}_k$, with q_i' and q_j combining into a primary hadron according to a fragmentation function $D(z)dz$. This represents the probability that the resultant hadron takes a fraction z to $z + dz$ of the parent quark's momentum

The light quark ($u\,d\,s$) fragmentation functions used are those suggested by Field and Feynman.[90] They reasoned as follows: Let $F(z)dz$ be the probability of finding a primary meson in a jet with fractional momentum between z and dz. Then the quark fragmentation functions $D(z)$ must satisfy

$$F(z) = D(z) + \int_z^1 D(z') F(\frac{z}{z'}) \frac{dz'}{z'} \quad .$$

There are simple solutions of $F(z)$ if $D(z) = (d+1)(1-z)^d$. In order to satisfy the requirement that $F(z)$ approach a constant as $z \rightarrow 1$, an extra constant is incorporated into $D(z)$ yielding

$$D(z) \propto 1 - a + 3a(1-z)^2 \quad ,$$

where $d = 2$ comes from fits to charged particle distributions. The *2-jet* data seems well described by this Field and Feynman ansatz.[92]

For heavy quarks, Peterson *et al.*,[93] wrote down their form for the fragmentation function by noting that gross features of the amplitude for the process $Q \rightarrow H(Q\bar{q}) + q$, a heavy quark Q decaying into a hadron with quark content $Q\bar{q}$ and a quark q, are described by an amplitude proportional to $1/\Delta E$, with the energy transfer ΔE given by

$$\Delta E = E_H + E_q - E_Q \quad .$$

If the hadron mass is dominated by the mass of the heavy quark, and z is a momentum fraction defined by $P_H = zP_Q$, then

$$\Delta E \approx \frac{m_Q^2}{2P_Q} \left\{ 1 - \frac{1}{z} - \frac{m_q^2/m_Q^2}{1-z} \right\} \quad .$$

An extra factor of $1/z$ accounts for the longitudinal phase space, resulting in fragmentation functions with form

$$D^Q(z) \propto \frac{1}{z\left(1 - \frac{1}{z} - \frac{\epsilon_Q}{1-z}\right)^2} \quad ,$$

with $\epsilon_Q = m_q^2/m_Q^2$.

Whether the secondary quarks are the result of light or heavy quark fragmentation functions, the quarks combine into a primary meson with quark content $q_i'\bar{q}_k$. Fragmentation proceeds until the energy of each remaining unbound quark is below a threshold of $O(1\,\mathrm{GeV})$. The final quarks from the cascades of the primary partons then join into soft primary mesons. Figure A.4 is a schematic illustration of hadron production in the IJM model.

An immediate problem is that since the partons fragment completely incoherently, energy and momentum are not conserved. Also, particles with higher energy are produced first (in the CM frame of the primary partons). This "Outside-In" cascade seems to conflict with the requirements of Lorentz invariance, which calls for the most energetic particles to be produced last, on the average.[94]

A.3.2 String Models

STR models[95] create hadrons via the break-up of a massless, color singlet string stretched between the primary quarks. Gluons are treated as kinks on the string that carry a finite amount of energy. A $q\bar{q}g$ topology is pictured as one string stretched between the q and g, and another string between the g and $\bar{q}$. The total energy between partons is assumed to be linear function of separation distance, with energy density $\kappa \simeq 1\,\mathrm{GeV/fm}$.

Mesons are produced by break-ups in the string as an "Outside-In" cascade. Figure A.5a represents a string break-up in position space, while Fig. A.5b shows a break-up in momentum space. Each newly produced quark combines with an adjacent parton, taking a fraction z of the available momentum. The steps between break-ups of the string are random and depend on the fragmentation functions used as well as the mass of the newly produced hadron.

In general, the last pair of partons produced in the breakup of the string will not correspond to a hadron mass. An early scheme to side-step this problem was to choose the z value for the last breakup that forced the final hadron to be on-shell. This resulted in particle distributions that depended on which end of the string the fragmentation started at. Even worse, an asymmetry existed in the central rapidity plateau. This is seen by the following argument. Consider the production of a heavy meson with small z. The proper time of the production point will be far from the average proper time $\bar{\tau} = \overline{m}/\kappa$. In general, it will then take many string breakings before the proper times of the hadron production points return to $\bar{\tau}$. The

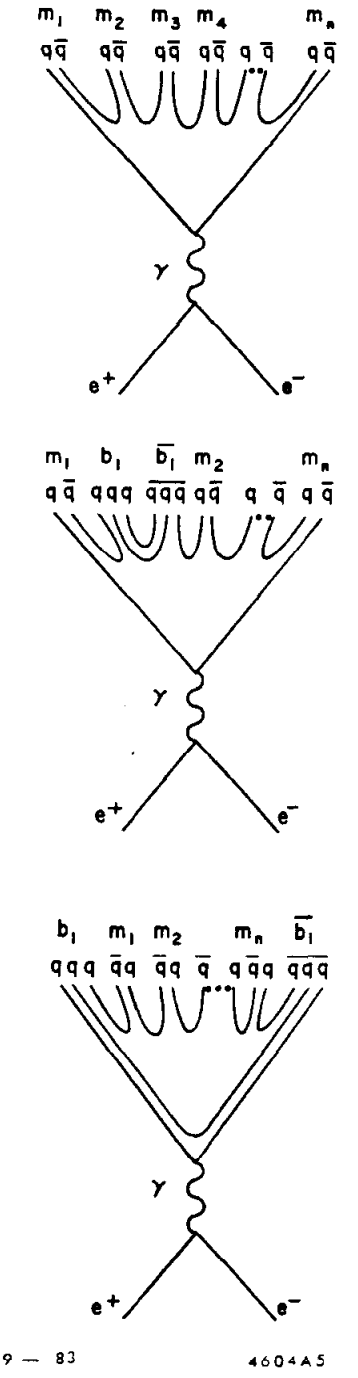

Figure A.4. Schematic representation of fragmentation in the IJM model. The upper figure shows how the quarks pair into mesons. The middle and lower figures show how baryons might result from pulling a diquark pair out of the sea.

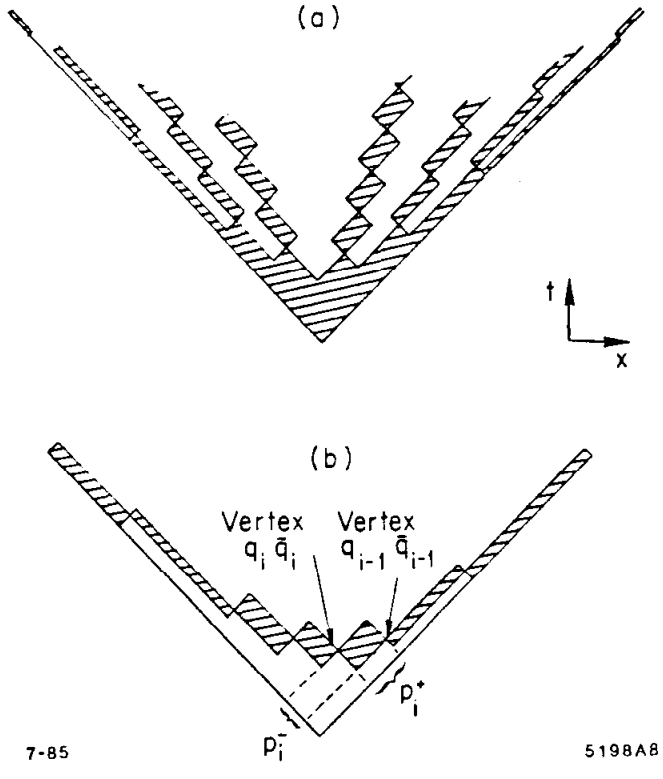

Figure A.5. Schematic representation of fragmentation in the STR model in the (a) position space and (b) momentum space representation. A quark from one end of a string breakup pairs with the antiquark from an adjacent breakup forming a meson.

fragmentation is asymmetric unless heavier mesons fragment with a harder z.[95]

It has been shown by the Lund group that if the fragmentation functions have form

$$f(z) = \frac{1}{z} z^{a_\alpha} \left(\frac{1-z}{z}\right)^{a_\beta} \mathrm{e}^{-bm_\perp^2/z} \quad ,$$

where b is a constant and the indices α and β label quark flavors, then the fragmentation will always be symmetric, *e.g.*, all pairs of breakups on the string are guaranteed to produce on-shell partons, and meson production in the central rapidity plateau will be symmetric. In principle, the a_α could all be different: the Lund group assumes $a_\alpha = a$. String fragmentation coupled with the above fragmentation functions forms the Symmetric Lund model.[95] This model has several advantages. Gluons are incorporated naturally by the string dynamics. Also, energy and momentum are explicitly conserved at each break-up of the string. The physical picture of fragmentation is simple, and the color singlets formed become the primary hadrons.

A.3.3 Cluster Models

In cluster models, the early primary partons are produced far off the mass shell. Each step in the subsequent leading-log QCD evolution places the parton nearer the mass shell.[96,97] At the end of the perturbative parton evolution, the gluons decay into quark pairs. This is always possible since we assumed $Q_0 > 2m_u$. Suppression of heavy quarks appears through phase space terms in the Sudakov factors. Adjacent partons then pair into color singlet clusters. If the mass of a cluster is greater than a scale M_c (this is a rather rare occurrence), then the cluster C fissions into two clusters X and Y according to the prescription

$$P_X^\mu = (1 - \frac{Q_0}{M_c}) P_q^\mu + \frac{Q_0}{M_c} P_{\bar{q}}^\mu$$
$$P_Y^\mu = (1 - \frac{Q_0}{M_c}) P_{\bar{q}}^\mu + \frac{Q_0}{M_c} P_q^\mu$$

where $P_{\bar{q}}^\mu$ and P_q^μ are the 4-momenta of the anti-quark and quark in the cluster C. This results in smaller cluster masses $M_X^2 \sim M_Y^2 \sim Q_0 M_c$.[98]

The clusters from fission, as well as primary clusters with mass less than M_c, undergo isotropic two body decay. This proceeds as follows: For each cluster, another light quark pair ($u\bar{u}$ $d\bar{d}$ $s\bar{s}$) is chosen at random. A quark from the cluster pairs up with the anti-quark just chosen. This pair is then assigned to a meson

resonance of the correct flavor with probability weighting according to phase space and spin. Another resonance assignment is made in a similar way to the remaining quark and anti-quark.

A parton skeleton formed as a product of leading-log evolution of the primary partons is represented in Fig. A.6a, with subsequent cluster formation illustrated in Fig. A.6b. Note that cluster models incorporate the phenomenological part of hadronization at the end of the event evolution. This is in contrast to the IJM and STR models that rely on phenomenology very early on.

A.3.4 Energy-Momentum Conservation in the Hadronization Models

After a boost that places the hadrons back in the lab frame (assuming a primary photon was produced by the Berends-Kleiss-Jadach $q\bar{q}(\gamma)$ generator), depending on the fragmentation model, energy and momentum may not be conserved.

The STR model features explicit energy-momentum conservation at each break-point on the string. The Cluster models feature energy-momentum conservation at each branching in the QCD evolution, as well as in cluster decay.

The IJM models have no explicit overall energy-momentum conservation. The source of this momentum imbalance is as follows:[99] During fragmentation, some of the longitudinal momentum of the parton is converted into transverse mass, and this reduction in longitudinal momentum is approximately independent of $\sqrt{s}$. For *2-jet* events, both jets have approximately equal longitudinal momentum, so on the average, momentum is conserved. But, for *3-jet* events, the parton with the least $P_{\|}$ is left with a greater fraction of its $P_{\|}$ going into transverse momentum than the partons having larger $P_{\|}$. On the average, this results in a momentum imbalance $\vec{P}_{frag}$ pointing opposite in direction to the lowest energy parton, usually the gluon. For *3-jet* events the size of the effect is:

$$\langle \vec{P}_{frag} \cdot \hat{P}_g \rangle \approx -0.8\,\mathrm{GeV/c} \qquad (\text{for } g \to q)$$
$$\langle \vec{P}_{frag} \cdot \hat{P}_g \rangle \approx -1.4\,\mathrm{GeV/c} \qquad (\text{for } g \to q\bar{q})$$

There are two popular approaches to force energy-momentum conservation. The Hoyer method[100] is designed to insure that the original parton directions correspond to the jet directions. The Hoyer recipe is:

- Rescale particle momenta so as to conserve the transverse momentum locally within each jet;

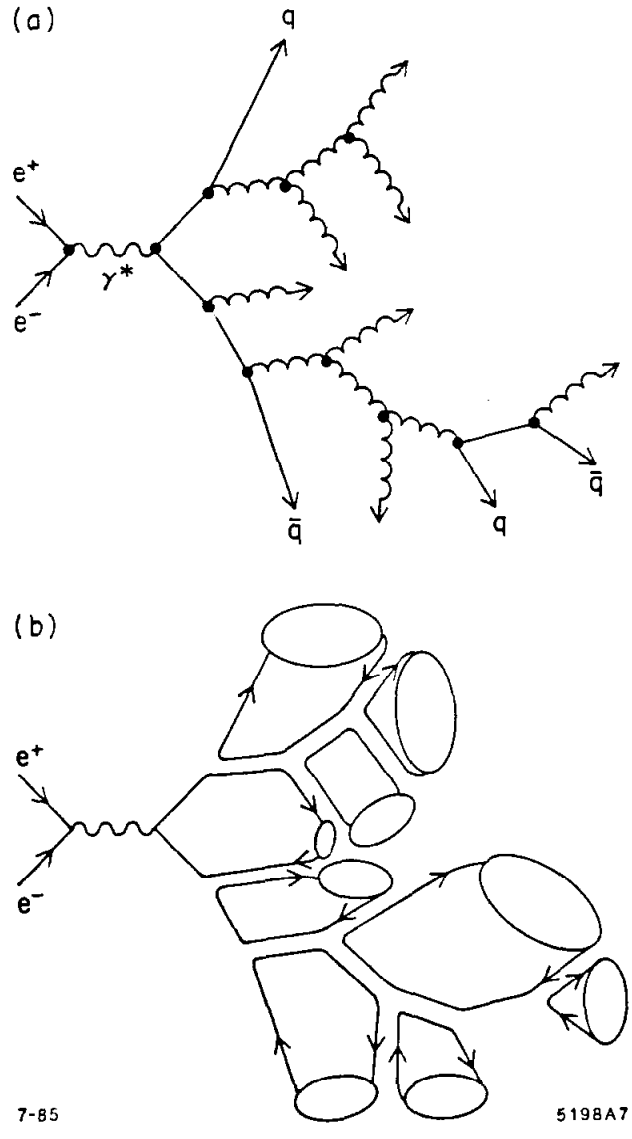

Figure A.6. Schematic representation of fragmentation in the Cluster models showing (a) leading-log QCD branching and (b) formation of color singlet clusters. The branching terminates when the mass is below the scale Q_0^2. Parton pairs form color singlet clusters that undergo decay into hadrons.

- For each jet, rescale the jet $P_{\|}$ so as to preserve the correct $P_{\|}$ ratios of the primary partons;
- On the entire event, rescale E_{frag} to be $\sqrt{s}$, with E_{frag} the sum of the final state particle energies.

The result is that the gluon jet generally ends up with a larger relative $P_{\|}$. This generates events that tend to be more *3-jet* like, but the jets have the same angle relationship as the corresponding primary partons.

The Ali method[101] is designed to preserve the jet energies. The procedure is:

- On the entire event, perform the boost $\vec{\beta} = -\vec{P}_{frag}/E_{frag}$;
- For the entire event, rescale E_{frag} to be $\sqrt{s}$.

The result are events that are generally boosted along the gluon direction. This generates events that are more *2-jet* like, but the ratios of jets energies correspond to the ratios of primary parton energies.

Other energy-momentum conservation schemes abound. These tend, however, to lie somewhere between the extremes of the Ali and Hoyer prescriptions, and consequently produce final states intermediate to the two extremes.

A.3.5 Decays of Primary Hadrons

The last stage of the hadronization is the decay of unstable primary hadrons into long-lived hadrons, leptons and photons. The branching modes, branching fractions and lifetimes are gleaned from experimental measurements[55] or via theory if experimental numbers are lacking.

A.3.6 Monte Carlo Versions Used for This Investigation

The IJM Monte Carlo event simulation utilized a modified version of the Lund Monte Carlo program[102] using the IJM fragmentation option. The light quark fragmentation functions used were those of Field and Feynman. The heavy quark fragmentation functions used were those of Peterson.[93] The String model used was a modified version of the Lund Monte Carlo code using the String fragmentation option, and using the Lund fragmentation functions for all quark flavors. A clustering Monte Carlo incorporating leading-log parton evolution along with angle ordering from soft gluon interference has been implemented by B. Webber.[103] We used a modified version of this code. The QCD branching was started by a primary $q\bar{q}$ pair. Large Q^2 gluon emission is therefore expected to be under-accounted as compared to an exact $O(\alpha_s^1)$ or $O(\alpha_s^2)$ parton generator.

The modifications to all the models involved incorporating initial state QED and weak radiative corrections, and modifying the decays of unstable particles to include secondary decay vertices. The IJM and STR models were modified to incorporate the full $O(\alpha_s^2)$ $e^+e^- \rightarrow quarks + gluons$ matrix element.[82]

A.4 Detector Simulation

The purpose of the detector simulation Monte Carlo is to accept as input the particle types and momenta from the hadronization Monte Carlo, and produce an ersatz event record event similar in format to that from a real event which can be used to model detector biases, efficiencies and backgrounds. The detector simulation makes extensive use of EGS[104] and HETC[105] computer codes for the electromagnetic and hadronic shower simulation. The computing time necessary for full shower transport through the MAC geometry is quite long, about 5 sec/event. Much of the preliminary studies made use of a fast calorimeter simulation that smeared particle energies by the expected calorimeter energy resolution. The fast simulation agreed fairly well with results of the full EGS and HETC simulations for the angular range used in the present study. This fast simulation was used to converge on reasonable values of fragmentation parameters, followed by fine tuning of the parameters using the full calorimeter simulation.

Appendix B. The Thrust Algorithm

One striking characteristic of hadronic events at PEP energies is the tendency for final state particles to emerge with a non-uniform spatial distribution of momentum. There tends to be a preferred axis that minimizes the transverse energy flow.

One quantitative characterization of this tendency is the thrust, given by[31]

$$T = \max_{|\hat{n}|=1} \sum_{i}^{N} \left| \vec{P}_i \cdot \hat{n} \right| / \sum_{i} \left| \vec{P}_i \right| \quad ,$$

with P_i the momentum of track i, and N the number of tracks to evaluate. The value of $\hat{n}$ that maximizes T is called the thrust axis $\hat{T}$. The expression above may be rewritten as

$$T = \max_{|\hat{n}|=1} \hat{n} \cdot \sum_{i} \epsilon_i \vec{P}_i / \sum_{i} \left| \vec{P}_i \right| \quad ,$$

where ϵ_i accounts for the absolute value. This demonstrates that $\hat{n} \propto \sum \epsilon_i \vec{P}_i$, and the problem reduces to finding permutations of $\epsilon_i = \pm 1$ giving maximal T:

$$T = \max_{\epsilon_i=\pm 1} \left| \sum_{i} \epsilon_i \vec{P}_i \right| / \sum_{i} \left| \vec{P}_i \right| \quad .$$

The brute-force approach of evaluating the last expression by testing all possible permutations of ϵ_i requires evaluating 2^N possible configurations, a task that grows increasing cumbersome with increasing N. However, not all of the 2^N configurations correspond to physical configurations. In fact, the number of physical configurations is exhausted by considering all possible planes formed by any two tracks; the tracks on one side of the plane are assigned $\epsilon_i = 1$, while tracks on the other side of the plane are assigned $\epsilon_i = -1$. All four permutations of the two tracks defining the plane must also be examined. The number of configurations tested in this scheme is

given by $4 \cdot \frac{1}{2} N(N-1)$, where the $N(N-1)$ factor comes from taking all unique pairs of tracks to define the planes, and the factor of 4 comes from testing all possible values of ϵ_i and ϵ_j for the two tracks i and j that define each plane.

This thrust algorithm is exact, and is used throughout this analysis.[106]

REFERENCES

1. M. Gell-Mann, Phys. Lett. **8**, 214 (1964).
2. G. Morpurgo, *Proceedings of the* 14^{th} *Intl. Conf. on High-Energy Physics*, edited by J. Prentki and J. Steinberger (Vienna, Austria, 1968), pp. 225-252.
3. W.K.H. Panofsky, *Proceedings of the* 14^{th} *Intl. Conf. on High-Energy Physics*, edited by J. Prentki and J. Steinberger (Vienna, Austria, 1968), pp. 23-42.
4. O. Greenberg, Phys. Rev. Lett. **13**, 598 (1964).
5. H. Lipkin, Phys. Lett. **45B**, 267 (1973).
6. E. Fernandez *et al.*, Phys. Rev. **D31**, 1537 (1985).
7. R.P. Feynman, *Photon-Hadron Interactions* (W.A. Benjamin, 1972), pp. 163-166.
8. J. Bjorken, Phys. Rev. **179**, 1547 (1969).
9. This discussion of the Higgs term in the Lagrangian follows:
   C. Quigg, in *Proceedings of the NATO Advanced Study Institute*, edited by T. Ferbel (Faile Marine Conference Center, St. Croix, Virgin Islands, 1980), pp. 143-278.
10. D. Gross and F. Wilczek, Phys. Rev. **D8**, 3633 (1973).
11. T. Cheng, E. Eichten and L. Li, Phys. Rev. **D9**, 2259 (1974).
12. R. Rückl, CERN preprint 83-1063, p. 19 (1983).
13. H. Georgi and S. Glashow, Phys. Rev. Lett. **32**, 438 (1974).
14. P. Langacker, Stanford Linear Accelerator Center report SLAC-PUB-2544, p. 3.14 (1980).
15. W. Marciano, *Proc. Fourth Workshop on Grand Unification,* ed. by H. Weldon, P. Langacker and P. Steinhardt (University of Pennsylvania, Philadelphia, 1983), p.13.
16. W. Marciano, in *Field Theory in Elementary Particles,* ed. by A. Perlmutter (Plenum Press, 1983) p.79.
17. G. Hanson *et al.*, Phys. Rev. Lett. **35**, 196 (1975).
18. R. Brandelik *et al.*, Phys. Lett. **86B**, 243 (1979).
19. M. Altoff *et al.*, Z. Phys. **C22**, 219 (1984).
20. G. Fox, *Proceedings of the SLAC Summer Institute on Particle Physics,* edited by Anne Mosher (Stanford Linear Accelerator Center, Stanford, California, 1981), pp.141-194.
21. *PEP Design Handbook*, edited by H. Wiedemann, Stanford Linear Accelerator report (1977).

22. A very dated discussion of the hardware, but a very interesting discussion of the MAC construction philosophy and physics goals:
R. Anderson *et al.*, *A Proposal for a Lepton-Total Energy Detector at PEP*, Proposal PEP-6 (1976).
23. W. Ford, in *Proceedings of the International Conference on Instrumentation for Colliding Beams,* edited by W. Ash, (Stanford Linear Accelerator Center, Stanford, California 1982); SLAC Report-250, 174 (1982).
24. G. Gidal, B. Armstrong, and A. Rittenberg, LBL Report LBL-191, 1983.
25. S. Clearwater, Ph.D. thesis, Stanford Linear Accelerator Center Report SLAC-264, 1983.
26. B. Heltsley, Ph.D thesis, University of Wisconsin-Madison Report WISC-EX-83/233, 1983.
27. S. Kaye, Ph.D. thesis, Stanford Linear Accelerator Center Report SLAC-262, 1983.
28. E. Cisneros *et al.*, IEEE Trans. Nucl. Sci. **NS-24**, 413 (1977).
29. M. Breidenback *et al.*, IEEE Trans. Nucl. Sci. **NS-25**, 706 (1978).
30. R. Anderson *et al.*, IEEE Trans. Nucl. Sci. **NS-25**, 340 (1978).
31. E. Farhi, Phys. Rev. Lett. **39**, 1587 (1977).
32. J. Izen, Deutsches Elektronen-Synchrotron report DESY 84-104, 1984.
33. R. Schwitters in *Proceedings of the International Symposium on Lepton and Photon Interactions at High Energies*, edited by W.T. Kirk (Stanford Linear Accelerator Center, Stanford, California 1976).
34. G. Hanson, in *Proc. of the Renc. de Moriond XIII* (1978) vol.2.
35. Ch. Berger *et al.*, Phys. Lett. **B78**, 176 (1980).
36. The "BBEL" calculation:
C. Basham, L. Brown, S. Ellis and S. Love, Phys. Rev. Lett. **41**, 1585 (1978).
37. E. Fernandez *et al.*, Phys. Rev. **D31**, 2724 (1985).
38. E. Fernandez *et al.*, Phys. Rev. **D31**, 1537 (1985).
39. M. Dine and J. Sapirstein, Phys. Rev. Lett. **43**, 668 (1979).
40. H. Aihara *et al.*, Lawrence Berkeley Laboratory report LBL-18408, 1984.
41. This study.
42. B. Adeva *et al.*, Phys. Rev. Lett. **54**, 1750 (1985).
43. W. Bartel *et al.*, Deutsches Elektronen-Synchrotron report DESY 84-050, 1984.
44. W. Bartel *et al.*, Phys. Lett. **129B**, 145 (1983).

45. M. Althoff *et al.*, Deutsches Elektronen-Synchrotron report DESY 84-057, 1984.
46. H. Behrend *et al.*, Deutsches Elektronen-Synchrotron report DESY 83-127, 1983.
47. B. Adeva *et al.*, Phys. Rev. Lett. **50**, 2051 (1983).
48. T. Gottschalk and M. Shatz, California Institute of Technology preprint CALT-68-1172 (1984).
49. T. Gottschalk and M. Shatz, California Institute of Technology preprint CALT-68-1173 (1984).
50. T. Gottschalk and M. Shatz, California Institute of Technology preprint CALT-68-1199 (1984).
51. E. Witten, Nucl. Phys. **B120**, 189 (1977).
52. H. Kolanoski, in *Proc. XXII Intl. Conf. on High Energy Phys.* Leipzig, July 19-25 (1984) p. 330.
53. P. Oddone, presented at the TPC HEPAP Review, (SLAC, Stanford, California, May 23, 1985) *preliminary.*
54. P. B. Mackenzie and G. P. Lepage, Phys. Rev. Lett. **47**, 1244 (1981).
55. Particle Data Group, C. Wohl *et al.*, Rev. Mod. Phys. **56** (num. 2, part II, 1984).
56. E. Bloom, at the *Aspen Winter Phys. Conf.* (Aspen, Colorado, January 13-19, 1985).
57. W. Atwood, in *Proceedings of the SLAC Summer Institute on Particle Physics*, edited by Anne Mosher (Stanford Linear Accelerator Center, Stanford, California, 1979).
58. G. Altarelli and G. Parisi, Nucl. Phys. **B126**, 298 (1977).
59. L. Abbott and R.Barnett, Ann. Phys. **125**, 276 (1980).
60. A. Bialas and A. Buras, Phys. Rev. **D21**, 1826 (1980).
61. BCDMS Collab. (D. Bollini *et al.*), Phys. Lett. **104B**, 403 (1981).
62. BFP Collab. (A. Clark *et al.*), Phys. Rev. Lett. **51**, 1826 (1983).
63. EMC Collab. (J. Aubert *et al.*), Phys. Lett. **105B**, 315 (1981).
64. EMC Collab. (J. Aubert *et al.*), Phys. Lett. **114B**, 291 (1982).
65. CCFRR Collab. (D. MacFarlane *et al.*), Z. Phys. **C26**, 1 (1984).
66. CHARM Collab. (F. Bergsma *et al.*), Phys. Lett. **123B**, 269 (1983).
67. CHARM Collab. (F. Bergsma *et al.*), Phys. Lett. **153B**, 111 (1985).
68. CDHS Collab. (H. Abramowicz *et al.*), Z. Phys. **C17**, 283 (1983).

69. J. Ellis, M. Gaillard and G. Ross, Nucl. Phys. **B111**, 253 (1976).
70. D. Barber *et al.*, Phys. Rev. Lett. **43**, 830 (1979); Phys. Lett. **108B**, 63 (1982).
71. A. Rújula *et al.*, Nucl. Phys. **B138**, 387 (1978).
72. D. Barber *et al.*, Phys. Rev. Lett. **43**, 830 (1979).
73. H. Behrent *et al.*, Phys. Lett. **B113**, 427 (1982).
74. W. Geist in *Proceedings of the SLAC Summer Institute on Particle Physics*, (Stanford Linear Accelerator Center, Stanford, California, 1982); Stanford Linear Accelerator report no. 259, pp. 389-404 (1983).
75. J. Aubert *et al.*, Phys. Lett. **110B**, 433 (1981).
76. G. Wolf, Deutsches Elektronen-Synchrotron report DESY-077, p. 14, 1982.
77. W. Bartel *et al.*, Deutsches Elektronen-Synchrotron report DESY 83-079, 1983; Deutsches Elektronen-Synchrotron report DESY 83-080, 1983.
78. A. Petersen *et al.*, in Proc. Symp. Multiparticle Dynamics (Lund, Sweden, 1984); Deutsches Elektronen-Synchrotron report DESY 84-082, 1983.
79. W. Bartel *et al.*, Deutsches Elektronen-Synchrotron report DESY 85-036, 1983.
80. H. Aihara *et al.*, Phys. Rev. Lett. **54**, 270 (1985); **54**, 1209(E) (1985); Lawrence Berkeley Laboratory report LBL-18408, 1985.
81. F. Berends, R. Kleiss and S. Jadach, Nucl. Phys. **B202**, 63 (1982).
82. The $O(\alpha_s^2)$ matrix elements used are those of
R. Ellis, D. Ross and A. Terrano, Nucl. Phys. **B178**, 421 (1981).
83. F. Gutbrod, G. Kramer and G. Schierholz, Z. Phys. **C21**, 235 (1978).
84. Z. Kunszt, Phys. Lett. **107B**, 123 (1981).
85. B. Andersson, G. Gustafson and B. Soderberg, Z. Phys. **C20**, 317 (1983).
86. G. Marchesini and B. R. Webber, Nucl. Phys. **B238**, 1 (1984).
87. D. Amanti *et al.*, Nucl. Phys. **B173**, 429 (1980).
88. A. Bassetto, M. Gafoloni and G. Marchesini, Phys. Rev. **100**, 201 (1983).
89. B. R. Webber, Nucl. Phys. **B238**, 429 (1984).
90. R. Field and R. Feynman, Nucl. Phys. **B136**, 1 (1978).
91. G. Altarelli and G. Parisi, Nucl. Phys. **B126**, 298 (1977).
92. R. Brandelik *et al.*, Phys. Lett. **94B**, 437 (1980).
93. C. Peterson, D. Schlatter, I. Schmitt and P.M. Zerwas, Phys. Rev. **D27**, 105 (1983).
94. J.D. Bjorken, in Proceedings of the SLAC Summer Institute on Particle

Physics (Stanford Linear Accelerator Center, Stanford, California, 1973).

95. B. Andersson *et al.*, Phys. Rep. **97**, 31 (1983).
96. R. Odorico, Nucl. Phys. **B172**, 157 (1980).
97. G. Fox and S. Wolfram, Nucl. Phys. **B168**, 285 (1980).
98. This cluster decay is that of Webber:
    B. Webber, Nucl. Phys. **B238**, 492 (1984).
99. This discussion is along the line of:
    T. Sjöstrand, Deutsches Elektronen-Synchrotron preprint DESY 84-023, 1984.
100. P. Hoyer, P. Osland, T. Walsh and P.M. Zerwas, Nucl. Phys. **B161**, 349 (1979).
101. A. Ali, E. Pietarinen and J. Willrodt, Deutsches Elektronen-Synchrotron preprint DESY T-80/01, 1980.
102. We use a modified form of the Lund JETSET version 5.2 code for IJM and STR fragmentation.
103. B.R. Webber, Nucl. Phys. **B238**, 492 (1984).
104. R. Ford and W. Nelson, Stanford Linear Accelerator Center report SLAC-210, 1978.
105. T. Gabriel and B. Bishop, Nucl. Inst. Meth. **155**, 81 (1978).
106. This thrust algorithm came to my attention through H. Lynch (private communication).